Buoyancy Controlled Float Swarms for Distributed Sensing in Coastal Waterways

Trevor Harrison

A dissertation
submitted in partial fulfillment of the
requirements for the degree of

Doctor of Philosophy

University of Washington

2021

Reading Committee:

Brian L. Polagye, Chair

Timothy Mundon

Steven L. Brunton

Program Authorized to Offer Degree:
Mechanical Engineering

University of Washington

Abstract

Buoyancy Controlled Float Swarms for Distributed Sensing in Coastal Waterways

Trevor Harrison

Chair of the Supervisory Committee:
Associate Professor Brian L. Polagye
Mechanical Engineering

Buoyancy-controlled underwater floats have produced a wealth of *in situ* observational data from the open ocean. When deployed in large numbers, or 'swarms,' floats offer a unique capacity to simultaneously map, in three-dimensions, environmental variables, such as currents, temperatures, and dissolved oxygen. This sensing paradigm is equally relevant in coastal waterways, yet remains underutilized due to economic and technical limitations of existing platforms. This dissertation describes the development, performance, and utilization of a prototype coastal float swarm.

Chapter 2 describes a virtual experiment evaluating performance of float swarms in providing high-resolution, four-dimensional mapping of currents in tidally-dominated, coastal settings. They are assessed against standard methods for measuring currents: an X-band radar, a stationary (bottom-mounted) acoustic Doppler current profiler (ADCP), and a mobile (vessel-based) ADCP. Using the output from a hydrodynamic simulation, a virtual field campaign was performed at twenty-four locations in Admiralty Inlet, Puget Sound, Washington during spring and neap tidal exchanges. A reconstruction of the volumetric currents was generated for each platform every 15 minutes and evaluated against the true currents to assess accuracy over a horizontal extent of 400 x 500 m at 5 m resolution and vertically through the entire water column (20-80 m) at 2 m resolution. Simulation results suggest

that, for this survey extent and resolution, a vessel-based ADCP survey is most accurate, followed closely by the float swarm. The overall performance hierarchy persists over most locations and stages of the tide. Thus, if mapping currents at high resolution (<10 m) and short time scales (<1 day) is the primary scientific objective, vessel-based ADCP surveys are likely the best option. For longer duration surveys, a combined deployment with a stationary ADCP and X-band radar system is the best choice. Lastly, if *in situ* measurements of scalar properties (e.g., salinity, temperature, dissolved oxygen) are desired, float swarms offer the unique capability of simultaneously sampling these properties while also surveying currents with accuracy comparable to mobile ADCPs.

Encouraged by the simulated effectiveness of floats swarms, a prototype swarm of twenty-five inexpensive, buoyancy controlled floats, dubbed μFloats (“microfloats”) was developed, filling a technological gap in coastal observational platforms. μFloats move vertically in the water column by controlling their buoyancy, but are otherwise Lagrangian. Underwater positioning is achieved by acoustic localization using low-bandwidth communication with GPS-equipped surface buoys. The μFloat features a high-volume buoyancy-engine that provides a 9% density change, enabling automatic ballasting and vertical control from fresh to salt water ($\sim$ 3% density change) and reserve capacity for external sensors. Chapter 3 describes the μFloat system in detail, and provides background on float dynamics and controls.

In Chapter 4, we outline three field tests undertaken to benchmark buoyancy control and acoustic localization accuracy: a quiescent-flow test in Lake Washington, WA; a controlled disturbance test in a 4 m deep salt water test tank; and an energetic tidal channel deployment in Agate Pass, WA. Results demonstrate depth-holding accuracy within ±0.2 m of target depth in quiescent flow and ±0.5 m in energetic flows, which is superior to that reported for other floats in the literature, and matched only by a float with hybrid buoyancy-engine and propeller-driven combined control technique. In the salt water test tank, divers added calibrated weights to the float, emulating disturbances from vertical currents and water density changes and demonstrated the floats' ability to correct for both with minimal deviation from the target depth. Unburdened by auxiliary sensors, μFloats can achieve a terminal velocity of ∼0.5 m/s, though overshoot and time to settle at target depth are improved by constraining the vertical speed to ∼0.3 m/s. This performance proved satisfactory for tidal channel deployments in Agate Pass: even in high currents (>2 m/s) and a short region of interest (∼1 km), float were able to reach and maintain depth on operationally relevant timescales (∼30 seconds). Additionally, range, robustness, and accuracy of the underwater acoustic localization array was evaluated based on results from both Lake Washington and Agate Pass. A strong thermocline in Lake Washington resulted in downward refraction of acoustic localization messages, reducing connectivity and requiring supplementary post-processing to extract accurate float trajectories. Nonetheless, localization accuracy was demonstrated to within ±5 m during periods with sufficient connectivity. Localizations in Agate Pass were similarly successful. While the acoustic environment was more favorable, the drift paths of GPS-track surface buoys produced inferior array configurations that resulted in larger localization errors.

Tidal currents, particularly in narrow channels, can be challenging to characterize, due to high current speeds (> 1 m/s), strong spatial gradients, and relatively short synoptic windows. Chapter 5 presents, in detail, the μFloat deployments in Agate Pass, WA, which represent the first use of float swarms toward small-scale (< 1 km), high resolution (< 5 m) measurements characterizing mean currents in energetic tidal channels. Float data was evaluated against data products from station-keeping and drifting ADCPs. Bearing out the simulation results from Chapter 2, we show that a modest float swarm can provide water velocity data with similar quality to ADCPs, while simultaneously capturing *in situ* properties that cannot be remotely observed, such as temperature.

In summary, this work contextualizes float swarm data products against standard *in*

situ and remote observational methods, providing both a measure of anticipated accuracy and operational practicality. Second, it describes the design and benchmarking of the μFloat system, which fills a technological gap in coastal observation platforms. Finally, the scientific relevance of the μFloat system is demonstrated in a novel tidal channel survey, with data products shown to agree with standard instruments, while expanding operational possibilities for coastal sensing. Future developments will build on these proven capabilities to explore the dynamics, physical properties, and soundscapes of our coastal waters.

TABLE OF CONTENTS

Page

LIST OF FIGURES

LIST OF TABLES

Table Number Page

NOMENCLATURE

μFloat	'micro-float'
SLB	surface localization buoy
ADCP	acoustic Doppler current profiler
CTD	conductivity-temperature-depth sensor
SWIFT	Surface Wave Instrument Float with Tracking
GPS	global positioning system
IMU	inertial measurement unit
GSM	Global System for Mobile Communications
ASV	autonomous surface vehicle
AUV	autonomus underwater vehicle
USBL	ultra-short-baseline (acoustic localization)
ROMS	Regional Ocean Modeling System
RF	Radio frequency
PPS	pulse-per-second
m_f	float mass
m_a	float added mass
U_f	float velocity

A	cross sectional area of the float
C_d	coefficient of drag
g	gravity
ρ_w	water density
U_w	water velocity
V_f	total float volume
V_o	nominal float volume with piston fully retracted
V_{pist}	volume of the piston
$V_{pist,NB}$	volume of the piston at neutral buoyancy
$V'_{pist}(t)$	time varying volume of the piston
$\mathrm{V}_{\mathrm{limit}}$	velocity limit in float controller
PD	proportional-derivative (controller)
GUI	graphical-user-interface
MAD	median absolute difference

ACKNOWLEDGMENTS

This dissertation is the culmination of seven years thinking about, tinkering with, and bringing to fruition, float swarms. The endeavour was undertaken naively: ‘Let’s build a swarm of ocean sensors. How hard could that be?’ Needless to say, this would not have been possible without support and contributions from a massive amount of people.

First and foremost, I must thank my advisor, Brian Polagye, for believing in this project from the beginning and supporting me over the long path that brought it to reality. His mentorship, dedication to quality research, and passion for teaching has been invaluable to my success. Thank you!

I would also like to acknowledge my committee members: Steve Brunton, for making complex math less scary and super cool; Tim Mundon, for the seed of an idea that grew into this dissertation and many excellent conversations and advice given regarding μFloat analysis; Matt Dunbabin, for hosting me at Queensland University of Technology for eight months and joining me in the canoe for the first ever μFloat field deployment; and John Delaney for pushing me to expand my vision of what might be possible in oceanographic sensing. Additional thanks to former committee member Andy Stewart for arguments about added mass, for securing the first grant to build the swarm, and a good memory from a Lake Union sail.

The creation of a single prototype is no small feat and construction of nearly thirty floats and five surface buoys was far more than I could accomplish on my own. Particular thanks are owed to Corey Crisp, without whom the floats would not exist: he holds nearly singular responsibility for the electronics and software systems that underlie float functionality. Thank you for being patient with my endless ideas and requests, for contributing a number of your own excellent ideas, and for simply being a great colleague. Additional thanks to Jessica Noe for completely overhauling my (crude) CAD design between prototype and swarm versions and for investigating possible improvements to the μFloat controls in her Masters work. Thanks to Cassie Riel for brilliantly managing all the pieces-parts of the swarm pre-production, joining us on field tests, diving with the float for the disturbance test, and generally supporting the project. Thanks to Ben Maurer for many fruitful conversations, a few great mountain bikes, and for diving with float during the disturbance test. Thanks to James Joslin for contributions of project management and mechanical design, but even more so for being a solid friend, colleague, collaborator, and rafting guide. Thanks to Justin Burnett and Paul Gibbs for design work. Additional thanks to Paul for captaining the vessel on an early Puget Sound tests and a more recent Lake Washington evening outing to rescue two missing μFloats. Thanks to Paul Murphy for developing the original hydrophone processing code utilized in Chapter 4, helping with the Sequim Bay mini-swarm deployment, and for capturing what remains the best photo of μFloat deployments.

Beyond those previously mentioned, a number of people contributed to the construction and occasional repairs of the swarm. Thanks to: Kira Smith, Jack Ryan, Zachary Tully, Andrew Witt, Ben Drajeske, Kevin Zach, Able Baca, and Harlin Wood.

A number of undergraduates contributed expertise and time to early prototypes that were crucial to early design improvements. Thanks to: Alex Reid, Olivia Rogers, Adam Hill, James Lindsay, Joushua Jerzy Jaworski Castillo, Brittany Lydon, Sage Berglund, Tomas Delgado, Chris Fisher, Christy Smith, and Mary Helwig. Thanks as well to Fritz Stahr, Jim Osse, Dana Swift, Eric D'Asaro, and Rick Rupin for advice on underwater floats.

Field tests would not be possible without the skill and expertise of vessel captains. Thanks to Captain Andy Reay-Ellers, Chris Archer, Paul Gibbs, and Curty Rusch for piloting some of the early tests. Thanks to Garrett Staines and John Vavrinec at PNNL-MCRL for early deployments in Sequim Bay that informed the design of the Agate Pass tests.

A special thanks is owed to the Agate Pass field team. Thanks to Jim Thomson for providing the SWIFTs and vessel ADCPs. Your expertise, communication in the field, and eagle eyes are all aspirational. Thanks to Alex de Klerk for excellent piloting in Agate Pass and Lake Washington and for not driving over floats (mostly). Thanks to Zachary Tully for being a gregarious and patient field assistant. And thanks to EJ Rainville and Nate Clemett for handing the SWIFTs and station-keeping. Additional thanks to Jim and Nate for pre-processing SWIFT and vessel-keeping data (respectively).

Thanks to Jeff Neasham for sharing the nanomodem technology and providing your expertise when things looked weird. Thanks to Kristen Thyng for the high resolution ROMS data used in Chapter 2 and helping me understand the intricacies of the data structure. Thanks to Chris Bassett for continued advice on acoustics in coastal water properties.

Graduate school would not have been possible – and certainly would have been a lot less fun – without support from family and friends. Thanks to Ariana for making the last three years amazing and for joining the Lake Washington field deployment! The Marine Renewable Energy Lab has been an endless source of excellent co-workers and friends. Thanks to: Paul Murphy, for conversations on acoustics, politics, and being a solid upstairs roommate; Hannah Ross, for excellent conversations, some fun outdoors, and being a solid downstairs roommate (Mike too!); Ben Strom, for great 4th of July's, help with data science classwork, and (even if briefly) being a solid upstairs roommate; to Emma Cotter, for being an excellent cubicle neighbor and friend. Curtis Rusch, for being an endless source of positivity and cheer and an excellent raquetball and running partner. Thanks to Rob Cavagnaro, Paul, Ben, Danny Sale, and Lars Hendrikson for great nights jamming - I wouldn't have played my trumpet while I was here if it weren't for you all. Brad Perfect, you were an invaluable adventure partner for my early years in graduate school, and the sole reason I managed to climb Washington's volcanoes. Thanks to Trent Dillon, Kate van Ness, Isabel Scherl, Brittany Lydon, and Aidan Hunt for starting conversations about race and helping us improve as individuals, a lab, and a department. To Dom Forbush, for early help on the bird and bat camera system, Chris Fisher, for assistance recording birds and bats, and to Chase Haegele, for outdoor adventures. The trouble with being around for eight years means many people have come and gone, most of whom have contributed to the great environment that supported my success - if you're missing, thank you.

And finally, thanks to my family. To my mom and my sister for unaccountable hours of support, love, and compassion throughout my life and especially in the past few years. To my Dad, for teaching me hard work, discipline, excellent grammar, and the power of establishing habits. I will forever miss you. To Larry, for your constant love and support over the years, for making Mom happy, for sharing your love of good cooking and good food, and passing along the sentiment that things will turn out all right. I will forever miss you.

Nearly all colormaps used here came from the **cmocean** library (Thyng et al., 2016). Note that all data processing described in this manuscript was performed in MATLAB (Mathworks®).

Funding: This material is based upon work supported by the National Science Foundation Graduate Research Fellowship under Grant No. DGE-1762114 and U.S. Department of Defense Naval Facilities Engineering Command. Construction of the swarm was supported by ONR DURIP N00014-17-1-2336. Ongoing work is supported by the U.S. Department of Defense Naval Facilities Engineering Command under N0002410D6318 / N0002418F8702.

DEDICATION

In memory of my fathers.

Chapter 1

INTRODUCTION

1.1 Scales of Ocean Sensing: Phenomena and Instrumentation

Oceans have long been the subject of human curiosity. Our coasts are home to nearly 40% of the world's population [105] and supply critical ecosystem services, including fish habitats, coastal protection, nutrient cycling, and recreation [8, 42]. Scientific understanding has revealed the myriad of phenomena existing and acting in our oceans (Fig 1a), with spatial scales ranging from 1 mm to 100 km and time scales extending from seconds to millennia.

To study these processes, scientists and engineers have devised a plethora of sensors, instruments, platforms, and methodologies, each providing sampling coverage suited to the particular phenomena of interest (Fig 1b). Early ship-based point measurements made by sailors for navigation have given way to a variety of technologically advanced *in situ* methods: continuous ship transects, Lagrangian surface drifters and subsurface floats, stationary moored instruments, and more recently autonomous underwater vehicles, including both short-term propeller-driven vehicles and longer-duration buoyancy-driven gliders, as well as heavily instrumented, high-bandwidth sensor arrays cabled to shore [56, 146]. Additionally, remote sensing provided by satellites equipped with myriad specialized sensors provide synoptic views not achievable with *in situ* methods [49].

1.2 Lagrangian Floats

Oceanographic floats are arguably the most significant and revolutionary *in situ* ocean observation paradigm developed in the last century [57, 122]. The very first floats developed by Swallow [142] led to the discovery of deep-water mesoscale ocean circulation [144, 143]. Similar floats evolved, including the SOFAR Rossby and Webb [123] and RAFOS floats [124].

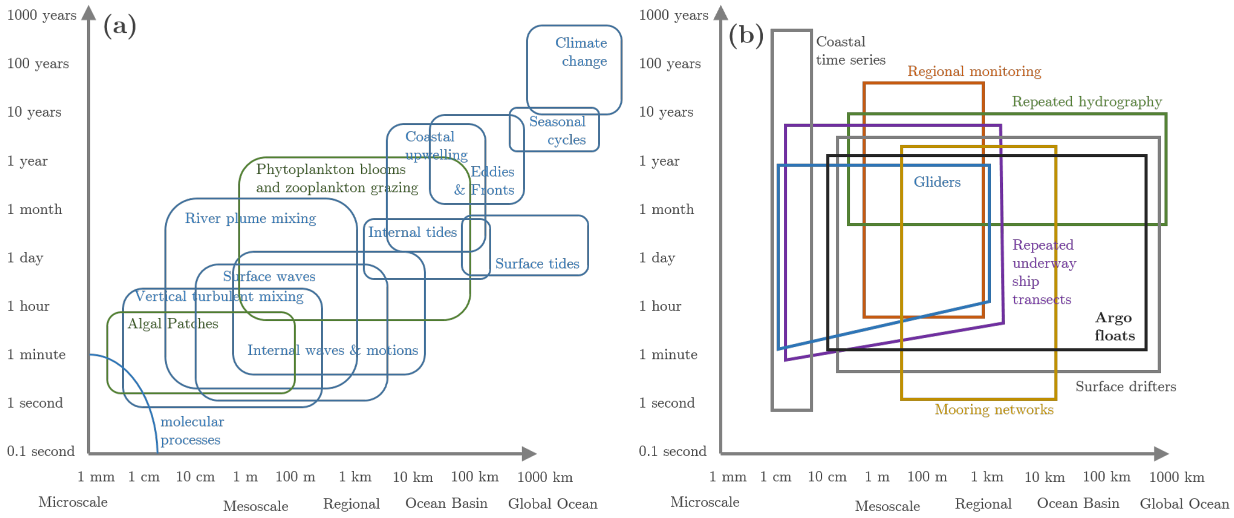

Figure 1.1: (a) Scales of ocean processes and (b) the platforms that sense them. Adapted from [81, 20].

The advent of the ALACE float [32] ushered in the global Argo float program, one of the most ambitious and successful oceanographic sensing campaigns in history. Initiated in 1999, the Argo program has since produced over two million profiles of conductivity-temperature-depth (CTD) data distributed throughout the global ocean, dramatically improving our understanding of ocean circulation and spatial and temporal distributions of salinity and temperature [120, 168]. The effort is ongoing, with 3900 active profiling floats distributed worldwide [1], and float missions have expanded beyond the initial standard 2000 m depth CTD profiles to now include biogeochemical sensors and deeper profiles to 6000 m [73].

1.3 Coastal Processes

Despite this demonstrated success in deep-water basin-scale research, floats remain underutilized in coastal environments. Coastal waters experience many of the same forces as the open oceans - tides, wind, solar heating, mixing, and biological activity - but these forces are magnified by interactions with shallow and variable bathymetry and influxes of fresh water from rivers. Spatial scales are smaller, with horizontal ranges O(1-100) km rather than O(10-1000) km, vertical ranges of O(10-100) m rather than O(100-1000) m, and temporal scales from seconds to weeks, rather than hours to decades. But within these smaller domains, forcing phenomena maintain the same order of magnitude. This concentration produces stronger spatial and temporal gradients. *In situ* and remote sensing must provide correspondingly higher fidelity observations to support effective and responsible monitoring, simulation, and management of coastal waterways [6, 164, 86, 48]. Floats, specifically when deployed in multitude as 'swarms,' are a promising method to supply this increased resolution in coastal environments.

1.4 Coastal Floats

A primary obstacle to the use of float swarms in coastal environments is a lack of appropriate hardware. Commercially available floats are designed for the global ocean: they include pressure housings and hydraulic buoyancy control systems for 2000 m dives and can tolerate relatively low accuracy depth control of O(10) m. Similarly, the high-precision sensors required for global scientific efforts are an appreciable fraction of total system cost. Because floats are deployed for long durations ($\sim$ 5 years) without intention of recovery, data communication is accomplished via satellite. These requirements produce floats with unit costs starting at $20k.

Coastal environments, defined here as extending from estuarine systems out to the continental shelf, have a maximum depth of roughly 200 m [12]. The correspondingly lower hydrostatic pressures permit use of simpler (and less expensive) mechanical systems for buoyancy control, such as the solid piston design implemented by [27] and [71]. Conversely, the shallow waters require higher resolution O(1) cm depth control. Density can vary by 3% where fresh river water enters salty coastal seas or be well-mixed in regions with strong tidal currents: a coastal float must accommodate both conditions. The smaller O(1-100) km horizontal domains permit economic hardware recovery and operations within the range of cellular and radio communication, eliminating the reliance on satellite communication for data offload. Finally, in areas with strong tidal currents (1-2 m/s), residence time in a region of interest may be limited to a few minutes, necessitating relatively high vertical speeds to reach depth on operationally relevant time-scales.

The only commercially available device appropriate for coastal environments is MRV Systems' ALAMO float. A smaller cousin of the Argo float platform, the ALAMO float was designed for rapid deployment in front of hurricanes and recently employed for under-ice research in the Arctic [72], gathering repeated profiles of salinity and temperature. Due to the minimal commercial options, a number of academic groups have designed custom floats suitable for the coastal ocean, as described in Table 1.1. D'Asaro et al. developed the Lagrangian float [30, 27] for studying convection, vertical velocities, vorticity, and turbulent mixing in the upper-ocean ($<$ 300 m) mixed layer and large scale tidal channels [3, 140, 39, 40, 83, 31, 29, 134]. The Lagrangian float has also measured internal waves, surface waves, and upwelling [82, 26, 28]. Roman et al. developed a coastal float equipped with bottom-tracking [127, 99, 121] and a downward-looking camera for visual benthic explorations, and later combined thruster and buoyancy-control for improved vertical actuation accuracy and efficiency [139]. While the previously mentioned profiling, Lagrangian, and bottom-tracking floats are roughly 1 m scale, Jaffe et al. designed the miniature Autonomous Underwater Explorer (M-AUE) with a form factor of roughly 0.2 m to better emulate passive and vertically-migrating larvae, as well as improve measurements of submesoscale ocean dynamics [71]. With a small swarm (16 floats), they demonstrated plankton patch formation in internal waves on the California Continental Shelf. More recently, higher capacity coastal floats have been developed for observing shelf biogeochemical processes [126] (Massion, pers. comm.), though these are quite large ($O(100)$ kg), requiring an A-frame for deployment, and costly (>$100k).

These examples clearly substantiate the applicability of floats towards the study of coastal processes. However, the available platforms do not fully address coastal ocean sensing needs. Specifically, while the coastal floats described here all provide unique control advantages over Argo floats, the high-precision sensors on D'Asaro and Roman floats render them prohibitively expensive for low-cost swarm deployments ($>$ $15k). Conversely, the M-AUE, designed for swarm sensing, is significantly less expensive at roughly $6k per unit, but its buoyancy engine is insufficient for operations in areas with large density gradients, such as river plumes. Additionally, the M-AUE form factor complicates auxiliary sensor integration.

Table 1.1: Summary of specifications for state-of-the-art floats, including the μFloat that is the focus of this dissertation.

Float	**MRV ALAMO**	**D’Asaro *et. al* ML-FII**	**Roman *et. al***	**Jaffe *et. al* M-AUE**	**μFloat**
Time in Use	5 years	20 years	4 years	8 years	4 years
Weight	10 kg	50 kg	16 kg	1.9 kg	4.7 kg
Diameter	12.2 cm	25 cm (1 m drag screen)	15.2 cm (30 cm w/ sensors)	12.4 cm	13 cm
Length (hull/antenna)	75 cm / 15 cm	89 cm / 52 cm	90 cm / 20 cm	14 cm / 13 cm	64 cm / 76 cm
Environment	Ocean	Ocean, Large Tidal	Coastal	Coastal	Coastal
Depth Rating	1200 m	300 m	100 m	100 m	100 m
Range (scale)	10-1000 km	1-100 km	1-5 km	1-10 km	1-10 km
Endurance	5-9 years	6 months	2 days	36 hours	30 hours
Buoyancy Control	Hydraulic Bladder	Solid Piston	Solid Piston	Solid Piston	Solid Piston
%ΔVol.	4.2%	1.5%	2%	0.8%	9%
Control Modes	Profiling Isopycnal Isobaric	Lagrangian Isopycnal Profiling	Profiling Depth Altitude	Depth/Isobaric	Depth/Isobaric
Depth Accuracy	±1 m	±1 m	±5 cm	<1 cm	±1 m
Localization	Custom (opt) [46]	w/ RAFOS (opt.)	USBL; visual odometry	Hydrophone mobile LBL	Nanomodem mobile LBL
Range	400 km	1200 km	2 km	5-6 km	1 km
Resolution	±100 m	±1 km	±5 m	±1 m	±5 m
Recovery Comms	Satellite	Satellite	Satellite, RF	Satellite, RF	Cellular, RF
Data Transfer	Satellite	Satellite	Satellite, RF	Manual	WiFi
Sensors	Temperature Pressure Salinity Biogeochem. (opt.)	Temperature Pressure Salinity Biogeochem. (opt.)	Temperature Pressure Altimeter Salinity (opt) Biogeochem (opt) Stereo Camera (opt)	Temperature Pressure 3-axis acceleration Compass Hydrophone	Temperature Pressure 3-axis acceleration 3-axis orientation 3-axis gyroscope
Applications (demonstrated)	Ocean circulation; Temperature and salinity in upper ocean; Hurricane processes; Arctic heat content	Vertical turbulent velocity and vorticity; Surface gravity waves; Internal waves; Convective mixed-layer temperature and salinity	Benthic surveying; Seafloor mosaic imaging; Visual odometry; Bi-modal depth control w/ thruster	Internal waves; Plankton mimics; Acoustic monitoring	Mean velocity mapping; Temperature mapping
Unit Cost	~ $24k	~ $80k	~ $15k	~ $6k	~$2.4k

1.5 Research Overview

The objective of this work was to investigate the feasibility and demonstrate the effectiveness of distributed sensing with swarms of buoyancy-controlled floats in coastal environments, as shown schematically in Figure 1.2.

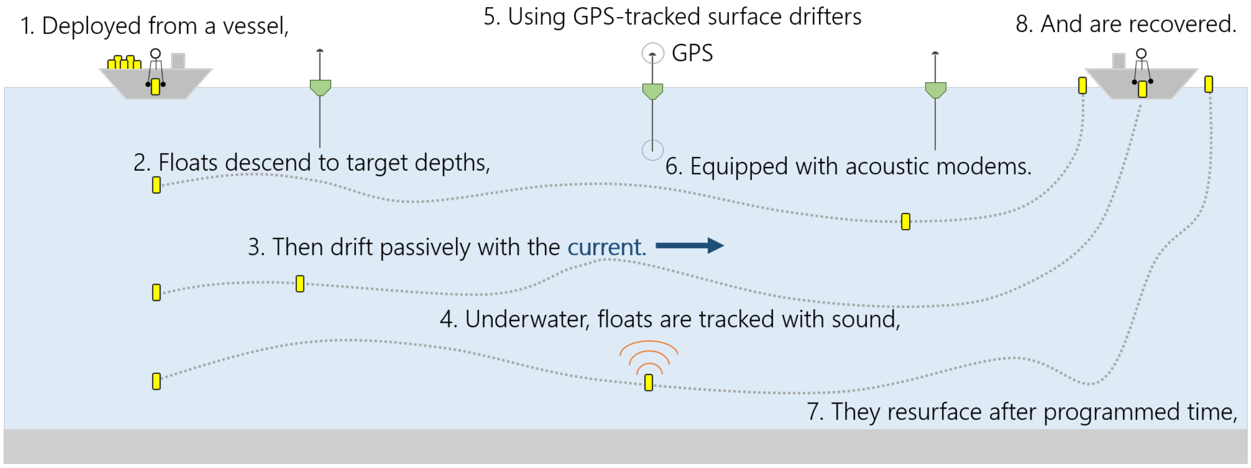

Figure 1.2: μFloat operational concept

In Chapter 2, we perform a virtual experiment within a high-fidelity model of Admiralty Inlet, Puget Sound, WA, evaluating the ability of float swarms to volumetrically resolve horizontal velocities of tidal currents, and compare the results against standard instruments – acoustic Doppler current profilers (ADCPs) and X-band radar. In Chapter 3, we present the μFloat ("microFloat") system, a buoyancy-controlled coastal float designed for economic swarm sensing. The μFloat system specifically addresses the gap between the capabilities and form factor of floats developed by D'Asaro and Roman and the limitations imposed by the form factor of the float developed by Jaffe, while taking advantage of recent developments in oceanographic and electronic systems to significantly reduce cost. In Chapter 4, we describe the tests undertaken to benchmark system performance, specifically buoyancy control and underwater localization, in both quiescent-flow and high-current environments. Chapter 5 presents comprehensive results from a deployment of twenty μFloats in Agate Pass, WA, an energetic tidal channel with currents exceeding 2 m/s, comparing swarm measurements to drifting and station-keeping ADCP measurements, and demonstrating their effectiveness as a scientific platform. Finally, Chapter 6 concludes the dissertation, discussing implications of the system performance on potential research applications and avenues for future improvements.

Chapter 2

VIRTUAL EVALUATION OF FLOAT SWARMS

The objective of this chapter is to investigate feasibility and effectiveness of float swarms for mapping tidal currents and evaluate their data products against those from standard instruments, acoustic Doppler current profilers and X-band radar systems.

This chapter contains content from [63] as published in *Journal of Atmospheric and Oceanic Technology* (©American Meteorological Society. Used with permission). Portions of that manuscript have been edited to avoid redundancy.

2.1 Introduction

Comprehensive mapping of water currents in energetic, coastal environments is challenging due to the combined forcing of tides, winds, waves, as well as the mixing of fresh and salt water, all of which vary in space and time. Yet a four-dimensional understanding is essential for multiple applications: currents affect navigation of surface and underwater vehicles [78]; they control transport of pollutants and nutrients [113, 115]; they drive sediment transport [4]; and they determine the feasibility of renewable power generation [116].

Here, we perform a virtual experiment to evaluate the performance of four measurement platforms for volumetric current mapping: a stationary acoustic Doppler current profiler (ADCP), a vessel-based mobile ADCP survey, an X-band surface radar, and an underwater float swarm. While these measurement platforms are used throughout the coastal ocean, their relative performance has not been benchmarked in energetic tidal environments. The platforms are evaluated using the output of a numerical simulation of Admiralty Inlet, Puget Sound, Washington (USA) [156, 158]. Specifically, volumetric flow-field reconstructions with a small spatial range $O(1\text{ km})$ and high-resolution $O(10\text{ m})$ are generated by all platforms every 15 minutes over an ebb-flood tidal cycle $O(12 \text{ hours})$ during neap and spring conditions. While observational requirements will vary with use-case, this type of short-term, high-resolution measurement is relevant to model validation efforts such as renewable energy resource characterization [2] and rip current identification [19]. We first examine the accuracy of all platforms at one location in Admiralty Inlet over a single ebb-flood cycle to identify sources of reconstruction error. We then compare results across locations and neap-spring cycles to assess general performance. In the discussion, we provide commentary on how the virtual results may extend to real surveys and larger surveys. We also include a qualitative comparison of platform operational constraints, as well as an examination of the particular strengths of hybrid stationary ADCP/radar surveys and of float swarms. We begin by briefly reviewing each of the measurement techniques.

2.1.1 Acoustic Doppler Current Profilers (ADCPs)

Acoustic Doppler current profilers (ADCPs) are widely employed to measure currents, using sound to remotely profile three-dimensional water velocity. ADCPs are available from multiple manufacturers and can operate in water depths shallower than 10 m to ocean-scale (2000 m), with trade-offs between range, resolution, and measurement uncertainty [55, 149]. When deployed on stationary platforms such as bottom-landers or moored buoys, they provide good temporal resolution (up to 16 Hz), but limited spatial coverage. Mobile surveys expand spatial coverage when deployed from surface vessels [51, 165], autonomous surface vehicles (ASVs) [13, 23], autonomous underwater vehicles (AUVs) [5, 13, 103, 159], or drifting platforms [59, 134]. Correcting for vessel motion can be accomplished through ground-tracking, integration with the ships navigation system, and motion-tracking on-board the instrument [161, 66, 104, 44]. For a mobile survey, increased spatial coverage comes at the cost of “blurring” in the volumetric current reconstruction due to the temporal evolution of hydrodynamics during a survey [96]. Thus, survey times are limited by the local period of temporal stationarity – the period of time over which a current field can be considered statistically stable – which can be as short as five minutes in tidal channels [98, 153]. In vessel-mounted, ASV, and AUV applications, survey strategies generally involve variations on repeated transects [14, 41, 51, 132], though station keeping methods which emulate repeated short-term stationary deployments have also been used to improve signal-to-noise ratios [13, 114]. ADCP current measurements rely on an assumption of flow homogeneity across diverging sensing beams (e.g, at 80 m distance from instrument, beams with 20° angle from normal measure points 50 m apart). In flows with strong, sharp gradients, this assumption can be violated, thus increasing measurement uncertainty [150], though modern instruments flag measurements with poor correlation between beams. Early Narrowband ADCPs also suffered from appreciable $O(10\%$ full scale range$)$ Doppler noise, requiring averaging over multiple pings for acceptable accuracy [51]. However, technological improvements in broadband processing have decreased Doppler noise to near-negligible magnitudes relative to mean current speeds in energetic tidal channels [60]. Finally, ADCPs cannot accurately survey near boundaries (surface or seabed) due to acoustic reflections [149].

2.1.2 X-Band Radar

X-band radar images backscatter off capillary waves on the sea surface. [169] developed the algorithm to estimate water currents from a time-series of similar radar measurements. The algorithm has been subsequently improved [50, 129, 130] and remains an area of active research [10, 15, 68, 90, 91, 135]. Horizontal surface currents are estimated from the difference between the distribution of measured wavenumbers and the distribution predicted by an ideal wave-dispersion relation [10, 91, 145, 169]. The resulting data product is a map of horizontal surface currents over the imaged region. While a wide range of radar frequency bands (HF [112], VHF [131], etc.) have been utilized in wave field and current monitoring, we restrict our attention to X-band technologies, as the range and resolution are most comparable to the other survey methods. X-band radars are typically deployed on shore, though recent vessel-based deployments with motion compensation have proved successful [90, 91]. The primary advantage of shore-based radar is the capacity for large spatial coverage $O(10\text{ km}^2)$ over extended time-periods. However, because the method relies on wave-current interactions, there is inherent depth-averaging in the estimated current field and limited sub-surface resolution. Recently, vertical gradients in horizontal currents have been estimated from the wavenumber dependency of current-induced Doppler-shift [15, 90]. However, fetch-limited coastal environments may not produce the spectrum of wavelengths necessary for these methods. In all cases, the accuracy of the current estimates depends on meteorological and wave conditions: wave height greater than 0.5 m, wind speed greater than 1 m s^{-1} [101, 125], and alignment of wind and waves within 45° [47], any of which may be intermittent in coastal waters. Additionally, all processing algorithms involve horizontal spatial averaging and must balance spatial resolution against measurement noise, with resulting output resolutions of 70 m to 250 m. Lastly, typical X-band radar data products do not include any direct estimate of vertical velocity.

2.1.3 Float Swarms

Oceanographic floats are *in situ* mobile sensing platforms that drift with the water currents. The most notable example is the worldwide Argo float array, with over 3800 floats currently deployed [120]. These floats adjust their buoyancy to move up and down in the water column and send data back to shore via satellite when at the surface. Recent efforts have extended float sensing to coastal environments to measure internal waves [71], larval transport [71], circulation [127], turbulence [30], and biological abundance [121]. The transition from ocean to coastal environments has spurred advancements in buoyancy control for larger density gradients and underwater tracking for sustained, high-resolution position measurements [71]. While promising, floats have a number of weaknesses. First, due to their limited actuation, they may quickly leave the area of interest and the intervention (recovery and redeployment) necessary to sustain persistent sensing is labor-intensive. Second, strong density gradients at fresh-salt water interfaces complicate control of buoyancy engines used for vertical actuation and self-ballasting [99, 27, 127]. Third, when submerged, float position must be estimated. Most localization techniques rely on short acoustic messages from beacons with known locations (e.g., drifting GPS-localized buoys [71] or USBL [118]) and therefore accuracy is impacted by the quality of the acoustic environment. Non-acoustic methods include visual odometry [18] and terrain-based localization [118] and are impacted by water clarity and knowledge of bathymetry, respectively. Whatever the method chosen, there will be associated limitations on accuracy, sample rate, and range of float position estimates.

2.2 Methods

2.2.1 Simulation Domain

The virtual measurement campaign to compare platform performance was conducted within a numerical simulation of Admiralty Inlet, Puget Sound, Washington (USA). Puget Sound is a fjord estuary in which nearly the entire tidal prism is exchanged through Admiralty Inlet [102], leading to tidal currents in excess of 3.5 m s^{-1} [116]. Tides are mixed-semidiurnal and have unbalanced ebb-flood cycles. Irregular coastline features, such as Admiralty Head, produce local flow acceleration and eddies. In additional to strong horizontal currents, two sills, at the northern and southern ends of Admiralty Inlet, cause strong upwelling and downwelling. The combination of vertical and horizontal gradients in water currents, as well as their temporal evolution, provides a complicated and energetic setting to evaluate platform performance.

We used the output from a high-resolution model of Admiralty Inlet [156, 158], which is a subdomain of the Model of the Salish Sea (MoSSea, [141]). MoSSea is implemented in the Regional Ocean Modeling System (ROMS), a three-dimensional, free surface, hydrostatic model with structured horizontal coordinates and terrain-following vertical coordinates [62, 133]. For the subdomain, open boundary forcing information comes from the MoSSea model. The Flather boundary condition is used for barotropic velocities and Chapman boundary condition for the free surface. Radiation and nudging were used for both the baroclinic velocity field and scalar quantities (i.e., salinity, density, and temperature). All walls were treated as no-slip and quadratic bottom stress was applied with $C_D = 3 \times 10^{-3}$, matching

[141]. The subdomain has a uniform horizontal grid with 65 m resolution and 20 vertical terrain-following layers that stretch proportionally to the local water depth at each horizontal location. The model output consists of velocity components U_x, U_y, U_z aligned with East, North, Up coordinates, respectively, as well as salinity, density, and temperature. Output temporal resolution is 15 minutes. Further specifics of the simulation are given in [156] and output data are available from [157]. While the magnitude of the modeled tidal currents within the Admiralty Inlet subdomain are known to be underestimated relative to field observations, the model adequately reproduces general circulation patterns [156, 158].

Within the subdomain, 24 locations were chosen for analysis (black points, Fig. 2.1), representing areas with strong spatial gradients (e.g., nearshore at Bush Point, Admiralty Inlet, and Point Wilson, Fig. 2.1, B, A, P respectively), as well as mid-channel locations with more homogenous flow. We evaluated platform performance during two tidal exchanges during September 2016 (arbitrary selection), for one strong, spring and one weak, neap tidal exchange (Fig. 2.2).

The virtual field experiment required interpolating the model output at arbitrary positions and times. Using MATLAB (Mathworks®), terrain-following vertical layers were mapped to Cartesian coordinates based on local depth. Spatial linear interpolation functions, $G_i = f(x, y, z)$, were then constructed for all model data outputs at each time step (i) to estimate quantities at any position. For the remainder of the paper, all reference to "sampling" the site model refers to querying these interpolation functions, rather than the discrete model output. Evaluation periods were constrained to a 15 minute time interval to align with the model output time step and approximate period of statistical stationarity at this location [98]. For temporal interpolation to intermediate times within an evaluation period, we first compute spatial information at the two bounding model output time-steps (i.e, G_i, G_{i+1}) and linearly interpolate between them.

Table 2.1 presents an overview of the raw data, sampling method, and processing for each platform. Figure 2.3 depicts the platform deployment stencil. The location of the stationary ADCP serves as the reference for deployment layout and determines nominal site

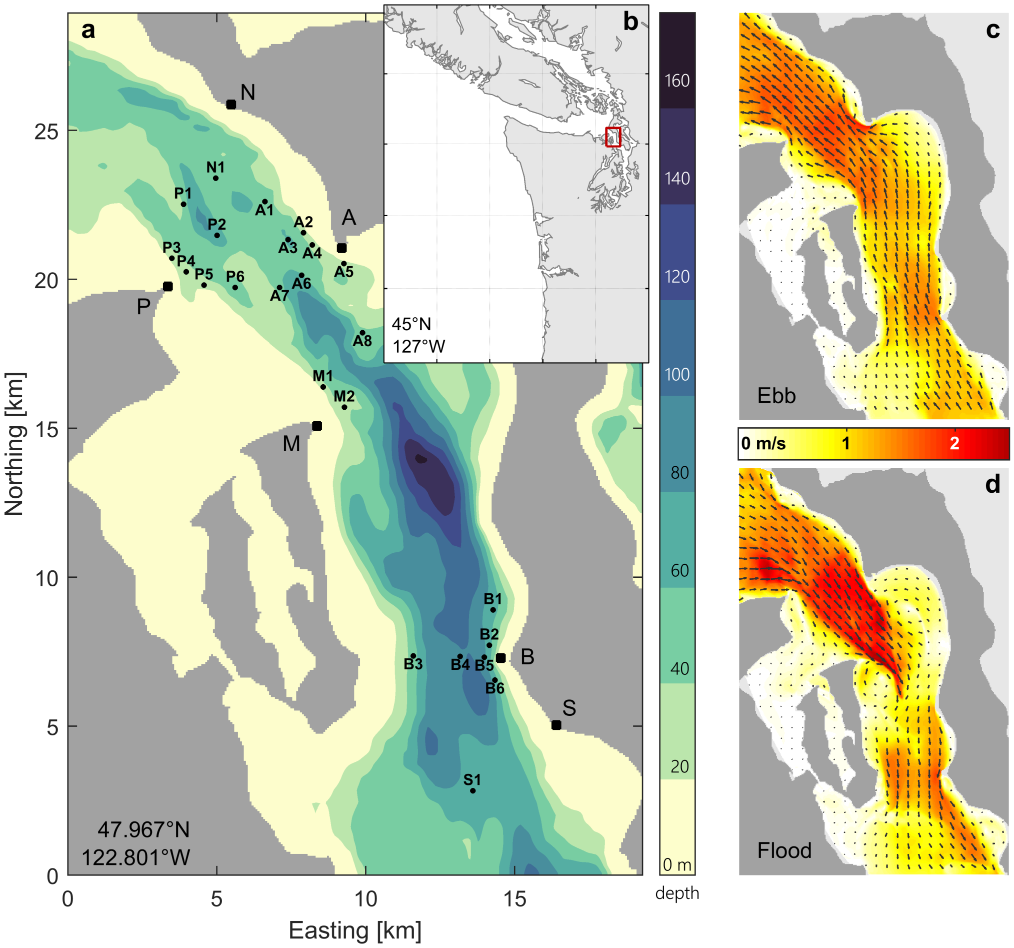

Figure 2.1: Virtual study site: (a) Admiralty Inlet. Color indicates local depth in meters, relative to mean sea level. Black circles indicate analysis locations. The black squares on land indicate X-band radar locations (N) North; (P) Point Wilson; (A) Admiralty Head; (M) Marrowstone Island; (B) Bush Point; (S) South. Location ID letter-prefix indicates the corresponding radar location used for comparison with other platforms. (b) MoSSea model domain [141], with the Admiralty Inlet sub-domain outlined in red. (c) and (d) horizontal currents at 15 m depth during peak spring ebb and flood tides, respectively.

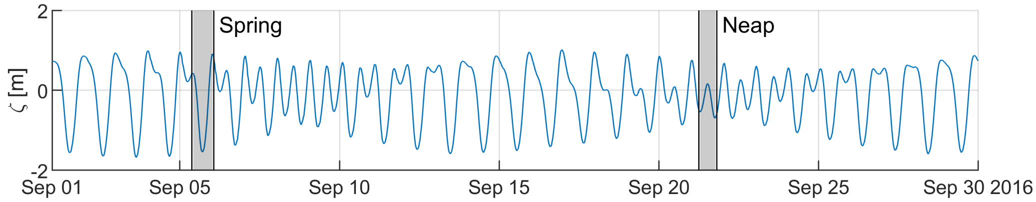

Figure 2.2: Time series of water surface level (ζ) at location A6. The two tidal cycles used in the analysis, a strong, spring exchange and weak, neap exchange, are indicated in grey.

Table 2.1: Summary of samples and processing for each platform

Platform	**Stationary ADCP**	**Mobile ADCP**	**X-Band Radar**	**Float Swarm**
Data Output (point)	u, v, w	u, v, w	u, v	u, v, w, T, S, P,…
Sample Locations	Vertical profile Range: <100 m Resolution: 1 m	"Lawnmower" pattern centered on stationary ADCP. Vertical profile with 1 m resolution every 1 m along transects perpendicular to currents.	Horizontal plane Range: 4 km radius circle Resolution: 150 m	30 floats deployed upstream of mobile ADCP survey boundary. Passively drift after reaching target depth. Sample frequency 0.2 Hz.
Data Processing	Horizontal extrapolation: Constant profile over region. Magnitude scaled by water depth	Linear interpolation function from all samples taken during 15 minute survey.	Vertical extrapolation: 1/7 power law current magnitude. Direction independent of depth.	Linear interpolation function from all samples taken during 15 minute deployment.

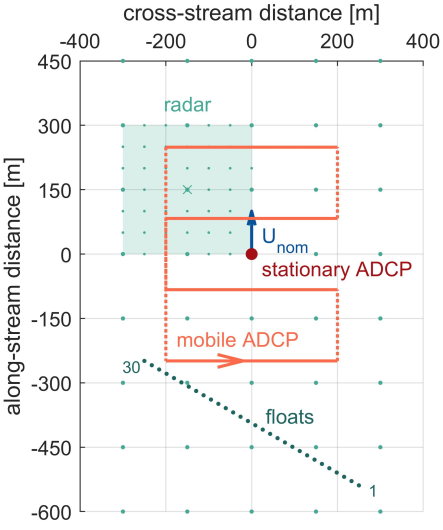

Figure 2.3: Deployment stencil. At each location indicated in Figure 2.1, the platforms were deployed accordingly. Horizontal spatial position is referenced relative to the stationary ADCP. Mobile ADCP survey and floats were aligned according to the nominal surface velocity U_{nom} defined for each peak ebb and flood cycle. For the mobile ADCP, solid lines indicate transects (sampling) and dashed lines indicate transits (not sampling). For floats, the first float (1) is deployed furthest upstream and final float (30) aligned with the boundary of the mobile ADCP survey. For the radar, the light green box indicates the area of spatial averaging for the output point ×, with smaller light green dots indicating the raw samples. The larger light green dots indicate radar output points.

parameters of depth D_{nom} (relative to the mean sea level) and velocity U_{nom} (horizontal velocity at 2 m depth). For a given tidal exchange (ebb or flood), the deployment layout was aligned relative to the flow direction during peak currents, and remained constant through the exchange. Details of sampling and deployment are provided for each platform in Sections 2.2.3-2.2.5 and the underlying code is available from [64].

2.2.2 Performance Evaluation

Platform performance was evaluated in terms of “sample accuracy” (i.e., how accurately each platform estimated the currents at a position in space and time) and “volumetric reconstruction accuracy" (i.e., how accurately the volumetric currents could be reconstructed from the platform measurements).

Sample Accuracy

The sampling accuracy of each platform was evaluated by comparing measured values to the true values at sample locations. As a reminder, "true" values are those interpolated directly from the original Admiralty Inlet model data. For radar and static ADCP surveys, sample error was taken as the difference between the measured and the true time-mean value at the sample location over the survey interval (15 minutes). For mobile ADCP and floats, sample error was computed as the difference between the instantaneous measured and true values at the sample location. Additionally for these two platforms, "time blurring" error [165] was calculated as the difference between the instantaneous measured value and the time-mean over the survey interval at the sample location.

Volumetric Reconstruction Accuracy

The accuracy of each reconstruction was assessed by comparing the measured field to the true field over the survey volume shown in Figure 2.4, defined by the rectangle bounding the mobile ADCP survey in the horizontal plane ($\sim$ 400 m x 500 m) and by the water depth in the vertical. A regular grid of query points with 5 m x 5 m x 2 m resolution was generated throughout the survey volume. The true field, U, was defined as the ROMS model output spatially interpolated over this evaluation grid and time-averaged over the survey interval. This oversampling of the ROMS model output improves the visual interpretation of reconstruction errors. The measured field, $\tilde{U}$, was generated for each platform as detailed in Sections 2.2.3-2.2.4. To facilitate interpretation, we present these fields as horizontal current magnitude $|U_H|$ and direction θ_H. Local reconstruction error, E_k, is calculated as the difference between the measured and true field at evaluation point k,

$$E_k = \tilde{U}_k - U_k. \tag{2.1}$$

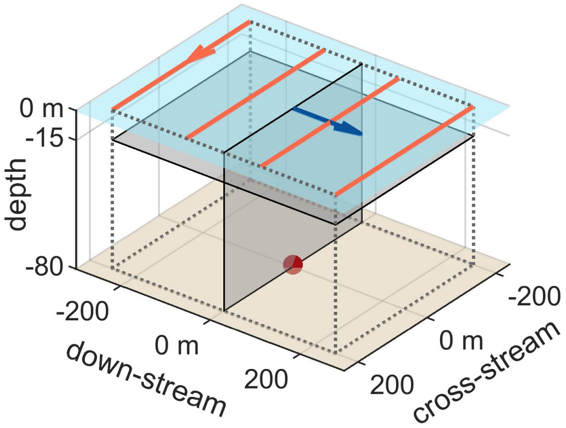

Figure 2.4: Evaluation geometry. The survey volume (indicated by dashed lines) is defined horizontally by the extent of the mobile ADCP survey (orange, transits omitted for clarity) and vertically by the water depth. The gray horizontal plane at 15 m depth is used to compare reconstruction accuracy in Section 2.3.1. The gray vertical cross-stream plane aligned with the stationary ADCP location (red) is used to evaluate salinity field reconstruction accuracy in Section 2.4.6. As in Fig. 2.3, water flow direction is indicated by the blue arrow.

Examining spatial distributions of reconstruction errors over a horizontal plane provides a qualitative understanding of how site dynamics and sampling techniques interact. However, a more compact representation is necessary for quantitative comparisons between multiple locations and tidal exchanges. For this purpose, we use the median absolute deviation (MAD) to characterize reconstruction accuracy. This is evaluated over the grid for each survey interval as

$$\mathrm{MAD} = median(|E_k|). \tag{2.2}$$

2.2.3 ADCP Measurements

ADCPs estimate three-dimensional current speed by measuring the beam-wise velocity of acoustic scatterers (e.g., zooplankton, sediment, bubbles) via the Doppler-shift of a transmitted pulse, or “ping” [149]. Time-gating differentiates the distances of returned signals from the instrument. With multiple, divergent beams, an assumption of spatial homogeneity of the measured field, and knowledge of the instrument position relative to the global reference frame, beam velocities are transformed to absolute water velocity. These samples are assigned a nominal position along a vertical profile extending away from the instrument.

ADCP: Model Implementation

To capture the sampling error associated with ADCP beam spread in an heterogeneous current field, we followed the method of [119]. A stencil of instrument-relative sample points was constructed based on the specified instrument range (100 m), bin size (1 m), blanking distance (1 m), and beam angle (20°), and transformed to absolute coordinates according to the instrument position, heading, and orientation (upward-looking or downward-looking). The ROMS site model (Section 2.2.1) was sampled at each along-beam bin location, projected into the beam direction, and these along-beam velocities were then used to estimate the absolute Cartesian velocity. We neglect Doppler noise here, but discuss its implications in Section 2.4.2. For bottom-mounted, upward-looking ADCPs, samples near the sea-surface (within 6% of local water depth) were discarded. For vessel-mounted, downward-looking ADCPs, equivalent samples near the bottom were discarded.

ADCP: Model Implementation - Stationary Platform

A bottom-mounted, upward-looking ADCP was implemented as the representative stationary deployment configuration (red circle, Fig. 2.3). The ADCP was elevated 1 m from the sea floor, consistent with a typical bottom package. A single, time-average profile was generated for each 15-minute survey interval. To extrapolate the profile over the survey volume, we assumed a constant velocity profile shape, but scale magnitude as

$$U_{local} = U_{ADCP} \frac{D_{nom}}{D_{local}} \tag{2.3}$$

where D_{local} is the local water depth. Velocity direction was assumed horizontally invariant over the survey volume. This "continuity" extrapolation is naïve, but a reasonable starting point for a previously unsurveyed location, and, as discussed in Section 2.3.1, yields relatively low MAD values.

ADCP: Model Implementation - Mobile Platform

The mobile ADCP survey was modeled as a downward-looking ADCP submerged to a depth of 1 m below a small vessel. The survey path followed a "lawnmower" pattern (orange track, Fig. 2.3) and was constrained to a synoptic, round-trip time of 15 minutes. The path consisted of four 400 m survey transects oriented perpendicular to the horizontal current and centered on the stationary ADCP. Vessel speed was 2 m s^{-1} along transects, sufficient to maintain vessel controllability in high currents while minimizing over-ground and relative flow velocities, both of which are potential sources of measurement error [41, 53]. Along each transect, a profile was sampled every 1 m of horizontal distance, corresponding to a 2 Hz sample rate. Maximum sample rates of ADCPs appropriate for our site depths are 8 Hz, thus the rate used here corresponds to a four-sample averaging to further justify omission of Doppler-noise effects. Vessel speed increased to 10 m s^{-1} between transects, resulting in a transect separation distance of approximately 125 m. We optimistically assumed the vessel had sufficient propulsion to overcome surface currents and that bottom-tracking and ship-motion compensation algorithms [149, 44, 104, 66, 161] were able to mitigate impacts of vessel heave, pitch, or roll on data quality. The data output from the mobile ADCP survey was a profile of three-dimensional velocity at each sample (i.e., ping) location along the transects. All samples within a survey interval were used to construct a linear interpolation function for comparison with the true field.

2.2.4 X-Band Radar

The raw data output from an X-band radar consists of a series of digitized images of radar backscatter from capillary waves. Every antenna revolution (2-4 s period), a 360° image is produced, with range and resolution determined by power, settings, and deployment geometry. Data processing requires a time series of $O(100)$ images, so in practice, a current field estimate can be produced every 4-7 minutes. All modern data-reduction techniques utilize a three-dimensional fast Fourier transform over a spatial window through a number of time frames to estimate the wave field and currents. The process generates a single, spatially averaged current estimate for each window. Larger spatial windows improve the signal-to-noise ratio, while smaller windows reduce heterogeneity within the analyzed wave field and better resolve gradients. While the analysis window can be shifted by an arbitrarily small amount, movements smaller than the window size act to smooth the output grid, rather than increase underlying resolution, at the cost of increased computation time [47]. Balancing these factors, window sizes range from 70 m (pers. comm. Joel Culina) to 750 m [15], with 0% to 50% overlap. Further, real wave fields contain a spectrum of wavelengths, where longer wavelengths penetrate deeper and interact differently with the underlying currents [90].

X-Band Radar: Model Implementation

Fully resolving a realistic water-wave climate, simulating the radar-signal interaction, and implementing a typical data-reduction technique was well beyond the scope of this paper. Instead, we restricted our effort to generating a velocity field representative of those produced by X-band radar data, while specifically accounting for the depth-averaging inherent in wave-current interactions and horizontal spatial averaging inherent in radar post-processing. We assumed the radar to have a range of 4 km radar with no degradation of accuracy within that range. Consequently, six on-shore locations (black squares, 2.1) provided coverage for all survey locations. The data output was a 150 m resolution grid of current estimates within the sensed region of a given radar (larger light green dots, Fig. 2.3). To account for spatial averaging inherent in data processing, each output point was generated by oversampling the true field on a 50 m grid within a 300 m square spatial window (light green rectangle and points, Fig. 2.3) centered on the output point and averaging the result. Wave-current interactions were approximated by depth-averaging currents from the top 5 m of the water column (corresponding to a surface wave with a 10 m wavelength). For the purposes of evaluating sample accuracy, measurements were assigned to a nominal depth of 2.5 m below the surface (i.e., mid-point of the 5 m depth-average). For volumetric reconstruction of horizontal velocity, we assumed 1/7th power law velocity profile [128], decaying from the estimated near-surface current to 0 m s^{-1} at the seabed. Direction was assumed constant with depth. One current field estimation was generated every survey interval (15 minutes).

2.2.5 Float Swarm

Underwater floats function as trackable water parcels with vertical control achieved via buoyancy manipulation [27, 99]. Floats are small (< 1 m) relative to spatial variations in mean currents, and when adjusted to be neutrally buoyant, float transport can be considered Lagrangian (i.e., float velocity is equal to the local water velocity) [27, 30, 32].

Float Swarm: Model Implementation

The float swarm was comprised of 30 individual floats (dark green dots, Fig. 2.3). This number was chosen semi-arbitrarily as a balance between deployment/recovery logistics and volumetric sampling density. As a relatively nascent approach for sampling in coastal waters, there remain technological challenges associated with buoyancy control and localization [27, 71, 99]. Because underwater localization remains an area undergoing rapid evolution [147, 80, 92] and our focus is inter-platform comparison, we did not define a specific localization method and instead optimistically assumed that underwater tracking could provide absolute position of the floats every 5 seconds. We discuss implications of position uncertainty in Section 2.4.2 and operational challenges in Section 2.4.4.

We simulated a simple float deployment procedure employed by [71]: a vessel-running cross-stream with floats sequentially placed in the water. As shown in Figure 2.3, the vessel path was angled such that all floats entered the survey volume at roughly the same time. The deployment line ran 500 m cross-stream (extending 50 m to either side of the mobile transects). We assumed floats could be dropped over the side at an interval of 5 seconds, requiring 145 s to deploy all 30 floats and vessel speed of 3.8 m s^{-1}. The floats were set to one of five depth settings (5%, 20%, 40%, 60%, 90% of nominal depth), repeated sequentially along the deployment line. On deployment, a float would dive at a rate of 0.4 m s^{-1} (a reasonable balance between buoyancy actuation and drag) until reaching target depth, then adopt Lagrangian behavior under the assumption that control action maintains neutral buoyancy. In the event that a float impacted the seabed (e.g., advection by downwelling), the float track was discontinued for simplicity. Less than 1% of tracks were terminated in this manner. In fast currents, floats leave the survey volume during the 15-minute survey interval, while in relatively slow currents, floats only traverse part of the survey volume. To compare this sampling approach to other platforms, a new float swarm was deployed every 15 minutes. This optimistically assumes a sufficient supply of floats and vessels such that deployment can occur concurrent with recovery.

The raw data output from the swarm are float positions every 5 seconds. Velocity was computed by differentiating position (third order polynomial spline). As with the mobile ADCP survey, all samples collected within each survey interval were considered a single snapshot of the field and used to compute a linear interpolation function for comparison to the true field. Velocities during diving and resurfacing were not included in the reconstruction. No extrapolation was made to evaluation points outside the convex volume bounding float samples and excluded evaluation points were not included in calculation of reconstruction statistics (i.e., MAD assessed only over the volume surveyed, not necessarily the entire survey volume).

2.3 Results

2.3.1 Volumetric Current Reconstruction at a Single Location

Figure 2.5 depicts the time series of reconstruction accuracy – computed as the median absolute difference (MAD) between the true and measured horizontal velocity evaluated over the survey volume – during the spring tidal cycle for each type of measurement platform at a mid-channel location between Admiralty Head and Point Wilson (Fig. 2.1, Site A6), as well as snapshots of the vertical and horizontal spatial variations of currents and reconstruction errors throughout the tidal cycle.

The mobile ADCP survey produces the lowest reconstruction error throughout the tidal cycle (Fig. 2.5a,b). From the snapshots (Fig. 2.5c,d), we observe the effects of non-synoptic measurements (i.e., "time blurring"). When the flow is accelerating (hour 3, strengthening ebb), the reconstruction underestimates the mean field over the upstream half of the survey area (instantaneously sampled velocity is less than the time-mean over the survey interval) and overestimates it for the downstream half. During peak ebb (hour 5), there is minimal field acceleration, and the error is negligible over the domain.

The float swarm has a MAD comparable to the mobile ADCP survey (Fig. 2.5a,b), though artifacts of linear interpolation from sparse sampling can be observed in all float snapshots (Fig. 2.5e). The floats have three primary limitations. First, during weak currents (less than 0.6 m s^{-1}), they do not traverse the entire survey volume (e.g., during slack tide, Fig. 2.5e, hour 2 and hour 8). Second, as for the mobile ADCP, there is non-synoptic measurement error (e.g., underestimate at hour 3, overestimate at hour 7). This is because the floats pass through the domain in much less than the 15-minute survey interval during periods of high currents, and thus measure a slower speed than the interval time-mean when the flow is accelerating and a faster speed when the flow is decelerating. Third, the float measurements are spatially sparse. For example, float sampling cannot resolve the vertical gradient over the upper 20 m of the water column at hour 10, leading to systematic overestimate of current speed (Fig. 2.5e). However, the flow is also accelerating during this period, which means that the non-synoptic error concurrently underestimates current speed. This is an example of how these limitations can combine to produce unexpected patterns in reconstruction errors.

Despite the simplistic horizontal extrapolation scheme, the stationary ADCP performs moderately well through much of the tidal cycle (Fig. 2.5a,b). Reconstruction errors (Fig. 2.5a,b) are correlated with the horizontal current anomaly (Fig. 2.5h). Because the vertical profile is relatively consistent within the survey volume (the vertical profile IQR is frequently

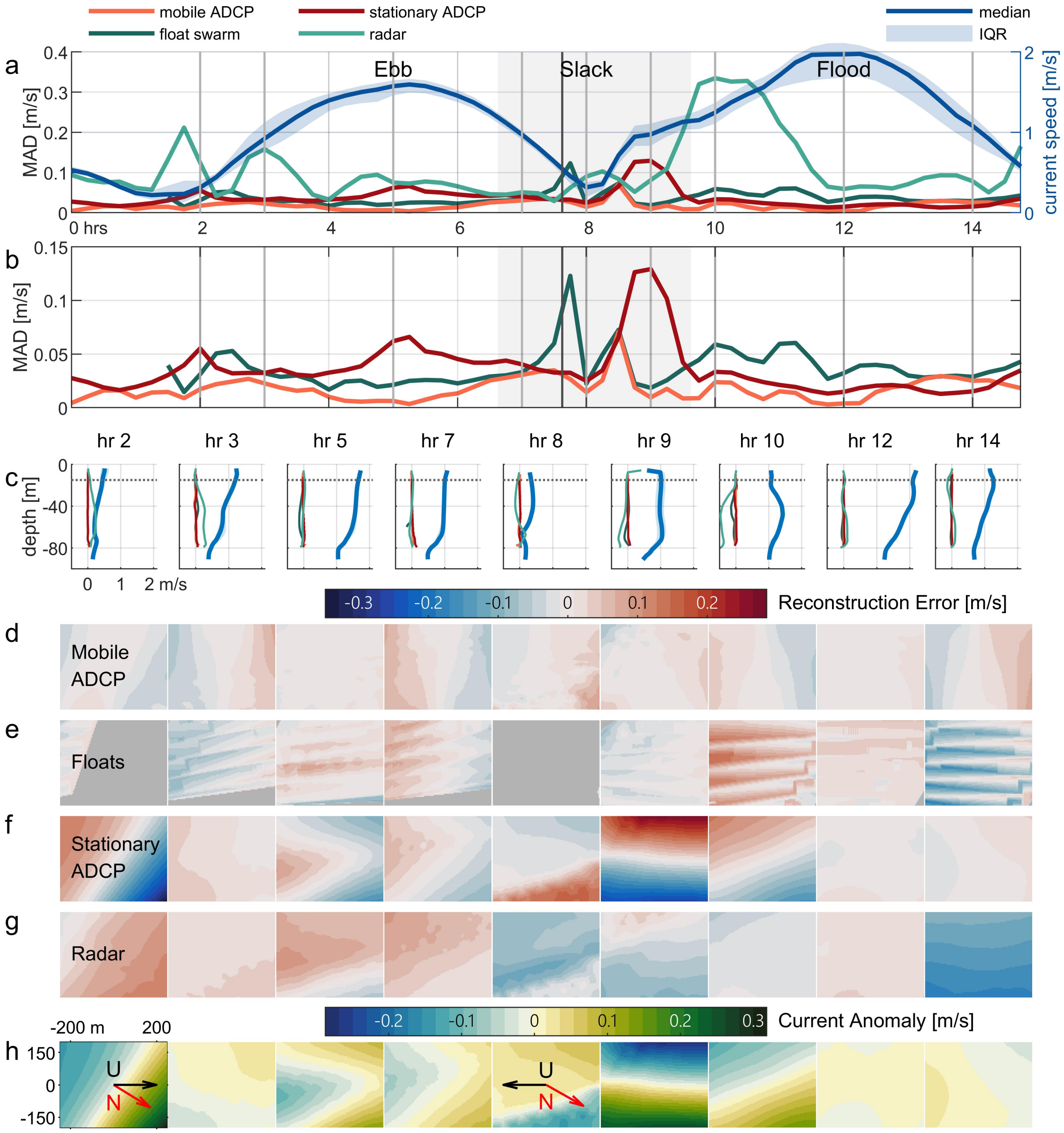

Figure 2.5: Volumetric current reconstruction mid-channel between Admiralty Head and Point Wilson (Fig. 2.1, Site A6) during the spring tidal cycle. (a) shows the time series of the median horizontal current magnitude and interquartile range (IQR) and the corresponding MAD for each platform, as evaluated over the entire survey volume. (b) magnifies the vertical axis in (a), dropping current and radar data series for easier comparison of stationary ADCP, mobile ADCP, and floats. Rows (c-h) are snapshots of the field and reconstructions at the indicated time. (c) depicts the current profile (median and IQR) and platform errors (Eq. 2.1) at the static ADCP location. (d-g) show reconstruction errors over a horizontal plane at 15 m depth. (h) depicts the current anomaly, $U - median(U)$ on the same plane. The dashed line across the vertical profiles (c) indicates the horizontal plane. For floats (e), light gray regions indicate unmeasured portions of the survey volume due to insufficient float coverage.

Table 2.2: RMS sample, time-blurring, and reconstruction error (MAD) computed over time series in Fig. 2.5a for each measurement platform.

Platform	**Sample Error (m/s)**	**Time Blurring Error (m/s)**	**Reconstruction Error (m/s)**
Mobile ADCP	0.001	0.026	0.02
Floats	0.000	0.023	0.04
Stationary ADCP	0.004	–	0.04
Radar	0.008	–	0.13

not discernible from the median, Fig. 2.5c), the single profile is representative.

Conversely, the radar performance correlates directly to time-variation in the vertical profile. When the current profile is well-represented by the assumed power law (Fig. 2.5g, hours 5, 7, 12, and 14), the reconstruction error is similar to the other platforms (Fig. 2.5a). However, reconstruction error increases sharply when the vertical structure deviates from this approximation (e.g., hours 9 and 10).

2.3.2 Sources of Error

Reconstruction error is a combination of the sampling error for individual measurements and errors from interpolation and extrapolation in space and time. Table 2.2 shows that, for all devices, error contributions from sampling are an order of magnitude smaller than those from reconstruction interpolation and extrapolation.

For both the float swarm and the mobile ADCP, instantaneous sample error is negligibly small relative to the interpolation errors. For the floats, the small sample errors are expected, as the only source of error is the differentiation of position to estimate velocity. For both ADCPs, sample error results from nonuniform flow across the beams, however the stationary ADCP exhibits higher sample error than the mobile ADCP. This makes sense, since beam spreading for the bottom-mounted, upward-looking platform is greatest near the surface where currents are strongest, while for the down-ward looking platform at the surface, beam

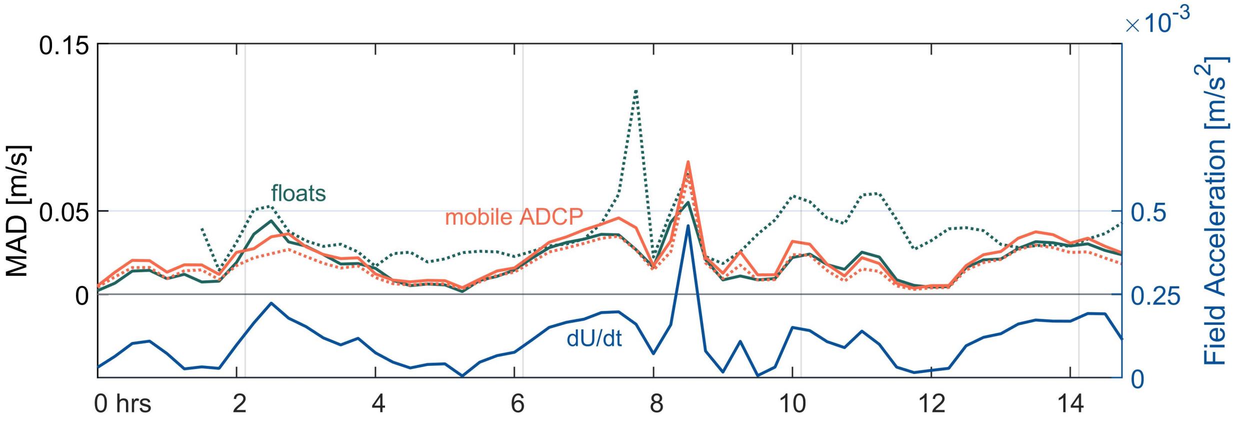

Figure 2.6: Comparison of mobile ADCP (orange) and float (green) errors to field acceleration over time for Site A6. For platforms, solid lines are median time-blurred sample error and dotted lines are the reconstruction error, as defined in 2.2.2. The solid blue line is the field acceleration.

spreading is greatest where currents are smallest. Sample error is highest for the radar, which is appropriate as it averages over a much larger volume of water than the other platforms.

Additionally, reconstruction error for both the mobile ADCP and floats appears predominantly attributable to time-blurring, as shown by the comparison of reconstruction error (MAD) to field acceleration (Fig. 2.6). For the mobile ADCP, the spatial interpolation implemented in the reconstruction mitigates the time-blurring error, as the transect sampling scheme causes up-stream (early) samples to be spatially averaged with downstream (late) samples. In contrast, float measurements are all sequentially "downstream" in both space and time and thus interpolation exacerbates the time-blurring error, increasing the reconstruction error.

2.3.3 Performance Trends Across Locations

Moving away from the single survey location discussed in Sections 2.3.1 and 2.3.2, we now consider platform performance across all 24 representative locations in the Admiralty Inlet subdomain. Figure 2.7 shows the time-distribution of platform performance (MAD) at each location (i.e., each platform time series in Fig. 2.5 is reduced to the statistical distributions shown for site A6). These distributions include data from both the spring and neap tidal cycles, with no noteworthy differences in performance between spring and neap.

Across locations, there is minimal variation in performance of the mobile ADCP or floats. Stationary ADCP and radar exhibit greater variability, which is expected since the appropriateness of the simple extrapolations in the horizontal and vertical directions change with location. Figure 2.8 reduces these data further, categorizing the overall performance of each platform in an energetic coastal setting in terms of the time-median reconstruction error at each location. This is evaluated for horizontal velocity, horizontal direction, and vertical velocity. Overall, relative platform performance is consistent across velocity components and locations in the Admiralty Inlet subdomain.

2.4 Discussion

2.4.1 General Trends in Reconstruction Accuracy

When interpreting results, we remind the reader that the conclusions drawn are specific to the spatial and temporal range and resolution of the simulated survey: in this case, mean currents measured at 15 minute intervals during the span of a tidal cycle (12 hours) over a horizontal range of <1 km with 5 m resolution and vertical ranges <100 m with 2 m resolution. We expect the trends observed here will hold for surveys at similar orders of magnitude and discuss implications for considerably different scale in Section 2.4.3. For this virtual survey, there are consistent trends in volumetric reconstruction accuracy: mobile ADCP performs best, followed closely by the float swarm and the stationary ADCP, and finally X-band radar. Relative performance varies in time (Fig. 2.5), with stationary ADCP and floats sometimes matching performance of the mobile ADCP, and the radar sometimes outperforming the stationary ADCP. While these distributions do vary moderately by location (Fig. 2.7), this variation is small relative to the overall differences between platforms. Further, the performance trend is consistent across all velocity components (Fig. 2.8). These performance

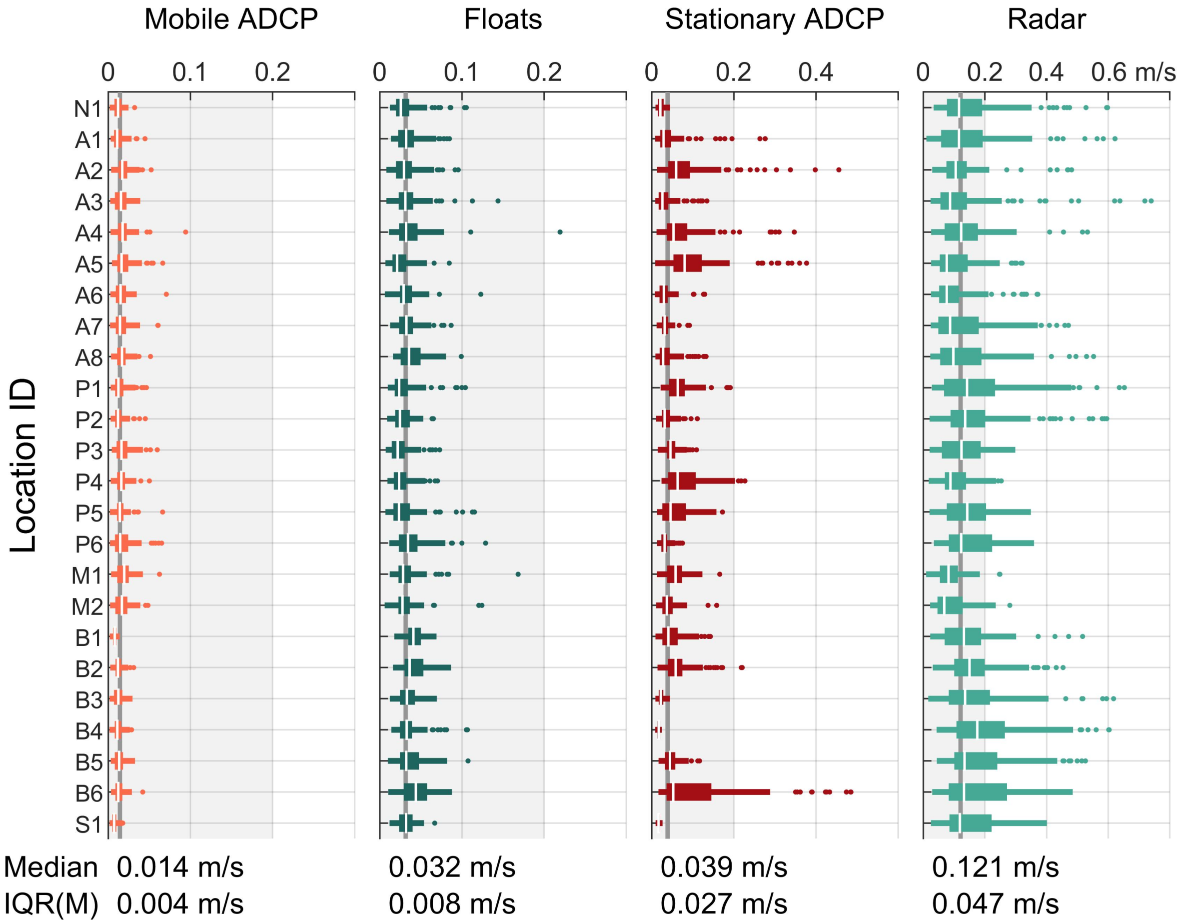

Figure 2.7: Temporal distribution of horizontal velocity reconstruction accuracy (MAD) at all locations. Location IDs correspond to the positions in the site map (Fig. 2.1). Note the axes scale for stationary ADCP and radar are double that for floats and mobile ADCP, as indicated by the shading. For each distribution, the white bar denotes the median, the thick bar denotes the interquartile range (IQR), and whiskers extend from $Q25 - 1.5 * IQR$ to $Q25 + 1.5 * IQR$. All values outside that range are considered outliers and denoted by points. For each platform, the median and IQR computed over the median values (white bars) from all locations are included for reference.

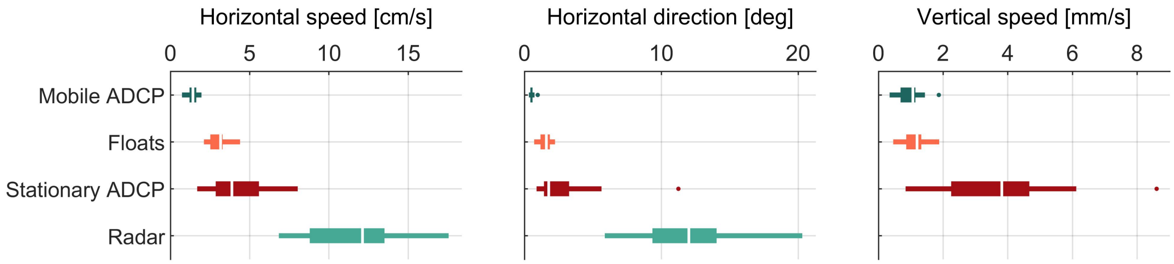

Figure 2.8: Generalized performance trends over the domain. Each distribution is composed of the temporal median from each of the 24 locations (i.e. distribution of the white bars in Fig. 2.7). Note the difference in units for horizontal (cm s^{-1}) and vertical (mm s^{-1}) currents. Distribution statistics are as described in Fig. 2.7

trends are correlated with the number of samples obtained by each platform within the survey volume. This demonstrates that the accuracy of volumetric reconstruction depends primarily on sample distributions and appropriateness of the interpolation/extrapolation scheme, rather than the individual sample accuracy. This is consistent with the magnitude of the sample, time-blurring, and reconstruction errors shown in Table 2.2. The mobile ADCP and floats directly sample throughout the survey volume and, accordingly, perform better than the X-band radar and stationary ADCP which require assumptions about the vertical and horizontal structure, respectively. The stationary ADCP is able to estimate volumetric currents with surprising accuracy when combined with a simple horizontal extrapolation. During periods with strong mean-flow acceleration, the stationary ADCP can even outperform a mobile ADCP survey, as it is unaffected by time-blurring. The relative performance difference between the radar and stationary ADCP is consistent with velocity gradients in the survey volumes, which are more significant in the vertical than horizontal directions.

We emphasize that these results are indicators of relative rather than absolute platform performance for several reasons. First, the MoSSea model is known to underestimate peak velocities in this region by as much as 1 m s^{-1} and has correspondingly weaker spatial gradients [156]. Second, the reconstruction errors are specific to the interpolation and extrapolation methods, and the simple strategies used here are likely a conservative estimate of the absolute accuracy that could be obtained with more sophisticated methods. For example, temporal de-meaning [53, 128, 162] or model-based data assimilation strategies (e.g., EOF [160], 4DVar [7]) would likely reduce reconstruction errors across platforms.

2.4.2 Extension to Real Surveys

We expect the overall performance trends observed here to extend to real surveys. However, the relative differences will be altered by sources of error omitted from our platform models and environmental phenomena not captured in the site model.

Impact of Omitted Platform Sample Errors

Our sample errors are significantly smaller than those reported for experimental measurements using some of these platforms. For mobile ADCPs, [60] report single-ping noise of 0.027 m s^{-1}, which is an order of magnitude larger than errors arising from the inhomogeneity across beams that is resolved by our implementation. For floats, [71] estimate localization accuracy of ±1 m horizontal with an update interval of 12 s, corresponding to velocity uncertainty of ±0.08 m s^{-1}, two orders of magnitude larger than sample errors from differentiation of position to obtain velocity. For both of these platforms, real sample error appears to be of similar magnitude to the reconstruction error estimated here. X-band radar measurements have recently been validated against surface drifters, with measurement differences of approximately 0.04 m s^{-1} [91]. As with the mobile ADCP and floats, these differences are an order of magnitude larger than errors arising from the spatial averaging in our implementation.

To explore how increased sample error for the mobile ADCP and floats would impact reconstruction accuracy, we reconsidered the simulation at site A6, modifying the float localization to include ±1 m standard deviation white noise on horizontal position, and the mobile ADCP to have ±0.03 m s^{-1} standard deviation white noise in horizontal velocity. With the additional noise, the root-mean-square reconstruction error (MAD) for the mobile ADCP increases to 0.024 m s^{-1} and, for the float swarm, increases to 0.053 m s^{-1}. This amounts to increases of 15% and 30% , respectively, relative to the errors reported in Table

2.2 arising from the more optimistic approach. Therefore, we expect the relative performance differences between mobile ADCP, floats, and stationary ADCP will likely decrease for real surveys, but maintain the hierarchy described in Section 2.3.3.

Impact of Additional Environmental Phenomena

Next, we consider the implications of dynamics not resolved in the Admiralty Inlet subdomain. The site model does not resolve flow gradients at horizontal scales less than 65 m, vertical scales less than 3-5 m, and temporal scales less than 15 minutes (i.e., velocity perturbations from turbulence or wave orbital velocities are not explicitly resolved). Because the radar and stationary ADCP obtain a time-averaged measurement, we do not expect their ability to reconstruct mean currents to be affected by waves or turbulence (with the caveat that X-band radar measurements require sufficient waves for operation). The impact of turbulence on the mobile ADCP and floats is more subtle. For both platforms, small-scale isotropic turbulence (1 second to 1 minute) will increase sample error in a similar manner as the elevated sample noise scenarios. In contrast, larger, coherent turbulent features with time scales on the order of 1 to 15 minutes, can substantially bias float measurements. For example, if some floats are caught within a coherent gust (e.g., an eddy) that propagates through the domain, they may observe currents that depart substantially from the time-mean value of that area. Without repeated sampling within the statistically stationary period, it is impossible to separate temporal variability from spatial gradients. Mobile ADCPs face similar challenges, though these are mitigated by the ability to maintain a survey transect through large-scale flow features. Therefore, for locations with relatively large coherent turbulent features, we expect reconstruction error to increase moderately for floats and, to a lesser extent, mobile ADCPs.

Wave effects will vary with site. In some locations, wave conditions may be strong enough to modify the overall mean flow field [65, 167] and sampling from all platforms should be avoided in waves if measurements of purely tidal currents are paramount. In moderate sea states when the velocity field can be treated as a linear superposition of wave orbital velocities and tidal currents, estimates of tidal currents can be obtained using processing specific to each platform and to the relative magnitude of wave and current contributions. For tidal channels like Admiralty Inlet, which are protected from swell, the wave field will be fetch-limited with relatively short wavelengths and waves would be unlikely to significantly bias sampling of energetic mean currents over the water column. However, in locations with greater exposure to high-amplitude swell, such as Pentland Firth, UK, or locations with lower mean currents, wave orbital velocities may be comparable to tidal currents. Time-averaging samples will filter wave contributions for radar and stationary ADCP measurements, but more sophisticated processing would be necessary to parse these contributions in mobile ADCP and float surveys. Finally, while the site model also lacks wind-driven currents and Stokes drift, we do not expect these phenomena to noticeably alter the results, as they also decay exponentially with depth and their velocities (0.01-0.1 m s^{-1}) are an order of magnitude smaller than mean currents over most of the tidal cycle at the study location.

2.4.3 Extension to Larger Survey Areas

With regards to spatial coverage, the results presented are constrained to a mobile ADCP survey to a track that could be repeated in 15 minutes, resulting in a relatively small 400 m x 500 m area. While quantitative analysis of generalized survey strategies is beyond the scope of the present work, some qualitative discussion is possible. For the mobile ADCP survey, expanding coverage will reduce horizontal resolution and increase time-blurring in accelerating flows [165]. For a float swarm of a given number, coverage depends on the deployment distribution and the currents. Adjustments to the deployment distribution based either on *a priori* knowledge or real time observations of trajectories could improve accuracy and/or coverage. For the static ADCP, the success of the horizontal extrapolation implies that locations throughout Admiralty Inlet (as modeled) are largely horizontally homogeneous over spatial scales < 250 m. As the extrapolation scheme is applied over larger survey areas or to locations with stronger horizontal gradients, accuracy is expected to diminish. Conversely, X-band radar provides an order of magnitude greater spatial coverage than the other platforms, with accuracy expected to remain largely constant over a larger survey area.

2.4.4 Operational Constraints

Thus far, our evaluation has solely considered the relative accuracy of the platforms, yet the choice of sensing platform must also weigh operational constraints: costs, spatial coverage, duration, and operational logistics. These are summarized in Table 2.3.

Logistically, a radar system is the simplest platform to deploy, supervise, and recover because it is land based and is only restricted by availability of a vantage point and electrical power. Deployment and recovery of bottom-mounted ADCPs is also relatively straightforward, requiring a vessel with sufficient lifting capacity and favorable surface conditions during a slack tide. Bottom-platforms must have sufficient ballast to remain stationary in high tidal currents, as well as wave orbital velocities in locations exposed to high-amplitude swell, and be trawl-resistant in locations with active fishing. Mobile ADCP surveys require a ship with sufficient propulsion to maintain maneuverability in strong tidal currents and moderate wave conditions, though even then, consistent repetition of survey tracks can be difficult [41]. Floats are logistically much more challenging requiring deployment and recovery once per survey interval. Logistical effort and cost will scale with the number of floats and their spatial distribution at recovery. Because of this, such operations may be better-suited to autonomous, robotic systems than human crews. However, float swarms may be able to use the depth- and time-variance of currents [137] to increase persistence and reduce logistical effort devoted to deployment and recovery. Finally, most float localization schemes use active acoustics, which require additional infrastructure, supervision, and specific environmental conditions (e.g., ambient noise at localization frequencies) to ensure optimal data quality.

Table 2.3: Operational considerations for survey platforms

Platform	**Cost**	**Spatial Coverage**	**Duration**	**Operations**
X-Band Radar	Capital: \$30k-\$130k per instrument Operational: fixed (deployment and recovery time)	Horizontal: - Range: $<$ 4 km radius from tower - Resolution 70-250 m, depending on data processing. Data quality degrades moderately with distance. Vertical: surface (0-10 m), though recent techniques estimate profiles to 10 m in certain wave fields [90].	Days - Months	Deployment on land. Requires power source, tower. Deployment and recovery requires 2-5 people, otherwise unsupervised. Vessel- or mooring-based surveys possible for regions offshore $>$ 4 km. Extraction of currents depends on wind conditions: minimum of 3 m s^{-1} [101, 125].
Static ADCP	Capital: \$30k-\$100k per instrument Operational: fixed (deployment and retrieval vessel time)	Horizontal: point 0(10 m) Vertical: - Range: 0-1000 m, frequency dependent. - Resolution: decreases with increased range, frequency dependent.	Days - Months	Vessel availability and low sea states - slack tide only required for deployment and recovery. In especially high current or wave environments, platform must be suitably ballasted, increasing deployment vessel lift capacity. Trawl-resistant platform in locations with active fishing.
Mobile ADCP	Capital: \$30k-\$100k per instrument Operational: scales with duration (vessel and crew time)	Horizontal: - Range: O(0.1-10 km), dependent on vessel speed and survey duration. Duration increases time-blurring in accelerating velocity field. - Resolution O(1-10 m) Vertical: [same as Static ADCP]	Hours - Days	Surveys primarily restricted to daylight hours, low sea states ($\leqslant$3). Vessel agnostic, but must be able to maintain course between 2-4 m/s (4-8 kn) for highest data quality. Requires 2-3 crew members. Alternative deployment platforms include autonomous vehicles, drifters.
Floats	Capital: \$3k-\$20k per float Operational: scales with duration (vessel and crew time), weakly with number of floats	Horizontal: - Range: O(0.1-10 km), varies with deployment distribution, current speed. - Resolution: O(1 m), scales with survey area for fixed number of floats. Vertical: - Range: 0-300 m, device dependent. - Resolution: scales with total water depth for fixed number of floats.	Hours - Days	Surveys primarily restricted to daylight hours, low sea states ($\leqslant$3). Require constant supervision, repeated recovery and redeployment. Vessel agnostic. Requires 2-3 crew members and single vessel for small deployments ($\leqslant$ 30 floats), more for larger deployments or increased repeat rates. Localization method may require additional infrastructure (e.g., surface or seabed positioning beacons). Accuracy is function of localization method and associated weaknesses (e.g., ambient noise interfering with localization messages).

2.4.5 Combining Stationary ADCP and X-band Radar

Both stationary ADCP and X-band radar provide long-duration data sets, but suffer from required extrapolations in the horizontal and vertical directions, respectively. As they provide complementary vertical and horizontal data, a logical solution is to deploy the platforms simultaneously. While such deployments have been performed to validate X-band radar surface current measurements against those from ADCPs [58, 10, 47], analysis was restricted to point-wise comparisons, rather than volumetric reconstructions. To evaluate the potential benefits for dual-platform deployments, we used the ADCP-measured vertical profile structure over the survey domain, scaled by the magnitude of the radar-measured local surface current relative to the surface current at the ADCP. The combined method was evaluated for all locations.

As shown in Figure 2.9a, combining stationary ADCP with X-band radar results in a median MAD over all locations of 0.029 m s^{-}1, a moderate improvement over the stationary ADCP in isolation (0.039 m s^{-}1) and a dramatic improvement over the X-band radar (0.121 m s^{-}1). While the combined method out-preforms floats (0.032 m s^{-}1), the mobile ADCP (0.014 m s^{-}1) remains the optimal method. Figure 2.9b-d depicts example cases of combined performance for the spring tidal cycle (currents as depicted in Fig. 2.5a) relative to the simpler stationary ADCP and radar methods, with mobile ADCP included for reference. Over all locations and for the vast majority of the time, the combined method is either equal to or better than the lesser of ADCP and radar reconstructions errors, as is demonstrated in Figure 2.9b. However, combining the platforms does not always improve the results, as can be observed in Figure 2.9c from hours 9-14, suggesting a particularly complicated flow, with strong variations in the horizontal and vertical. Finally, Figure 2.9d depicts a case when the site variance is largely vertical: the radar reconstruction suffers from the power-law extrapolation while the stationary ADCP performs nearly as well as the mobile ADCP. This site also demonstrates the most common way in which the combined method performs worse than either isolated platform: at hrs 9-10, the radar error dominates the reconstruction,

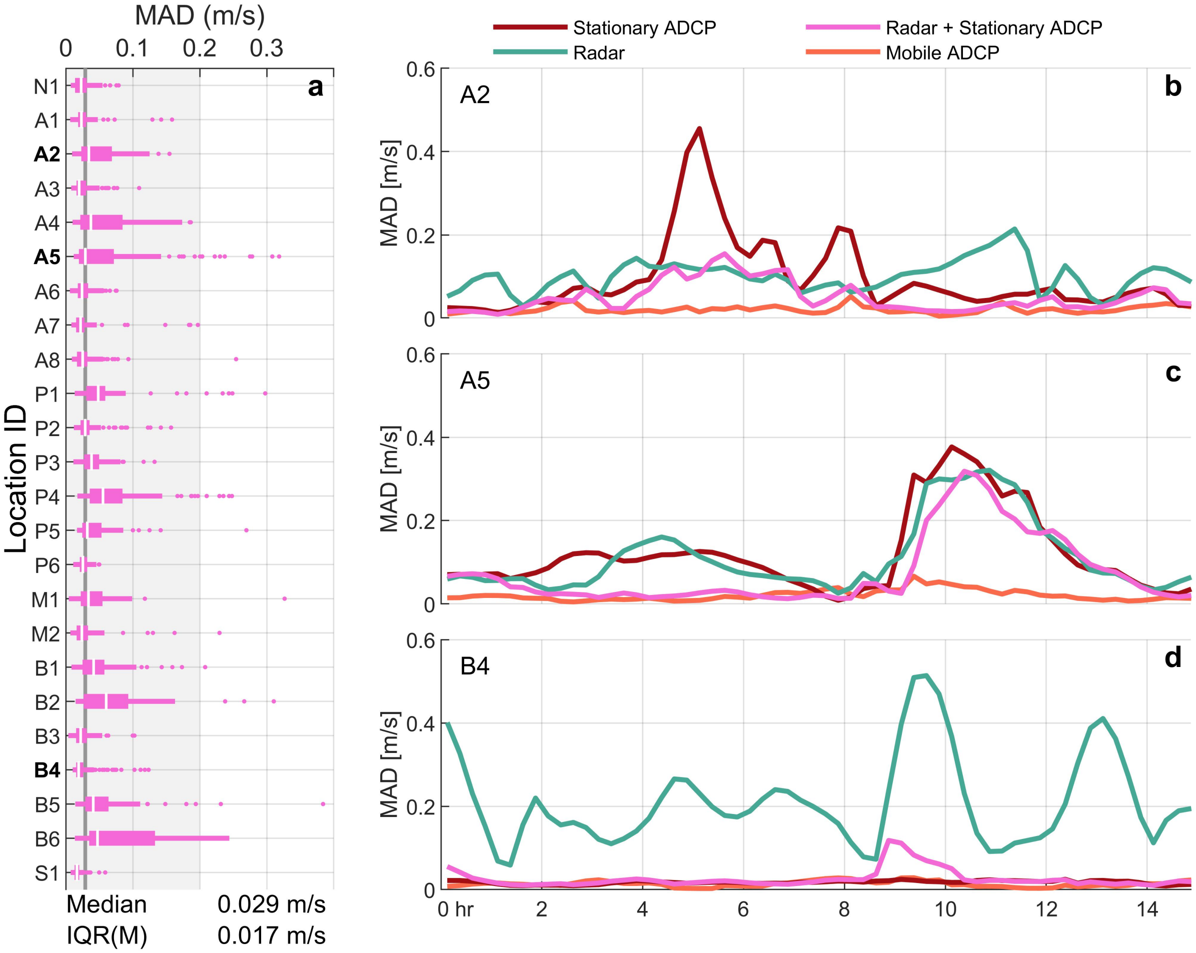

Figure 2.9: Combined stationary ADCP and radar deployment. (a) Distribution of horizontal velocity reconstruction accuracy (MAD) at all locations. Distribution statistics are as described in Fig. 2.7. (b-d) Time series of MAD for combined method as compared to radar, stationary ADCP, and mobile ADCP at locations A2, A5, and B4. Floats excluded for clarity.

suggesting that the horizontal variance at the surface, as captured by the radar, is different than the variance throughout the water column. While the mobile ADCP still consistently performs better than the combined method, the dual-deployment of stationary ADCP and X-band generally increases accuracy and has a clear persistence benefit over either floats and mobile ADCPs.

2.4.6 Float Swarm Physical Sampling

While floats are unable to reconstruct velocity with as high an accuracy as the mobile ADCP and are only suited to short-term deployments, they have one distinct advantage over the other platforms: they can simultaneously sample physical properties that cannot be remotely sensed at depth, such as temperature, salinity, and dissolved oxygen. To demonstrate this capacity, we applied the same methods to sample and reconstruct salinity, another output from the site model, under an assumption of negligible sample error in this quantity. Figure 2.10 shows the salinity reconstruction accuracy of the float swarm through site A6 during the neap tidal cycle (condition with highest stratification). As would be expected, depth-averaged salinity increases during the flood tide, as water from the Pacific Ocean enters the domain from the northwest, and decreases during ebb when brackish water exits Puget Sound. The floats accurately capture this signal, with reconstruction errors an order of magnitude smaller than the range over the time series. The one notable exception is around slack tide, when poor coverage biases the volumetric reconstruction at hours 6 and 7. As for the velocity fields, interpolation artifacts caused by sparse sampling are evident in all reconstructions (Fig. 2.10c), but suggest an ability to volumetrically resolve gradients in scalar water properties to an extent that is not currently feasible.

2.5 Conclusion

This study evaluates the ability of four sensing platforms – stationary ADCP, mobile ADCP, X-band radar, and a float swarm – to volumetrically characterize four-dimensional currents over a survey volume with a horizontal extent of 400 x 500 m. For this virtual survey, mobile

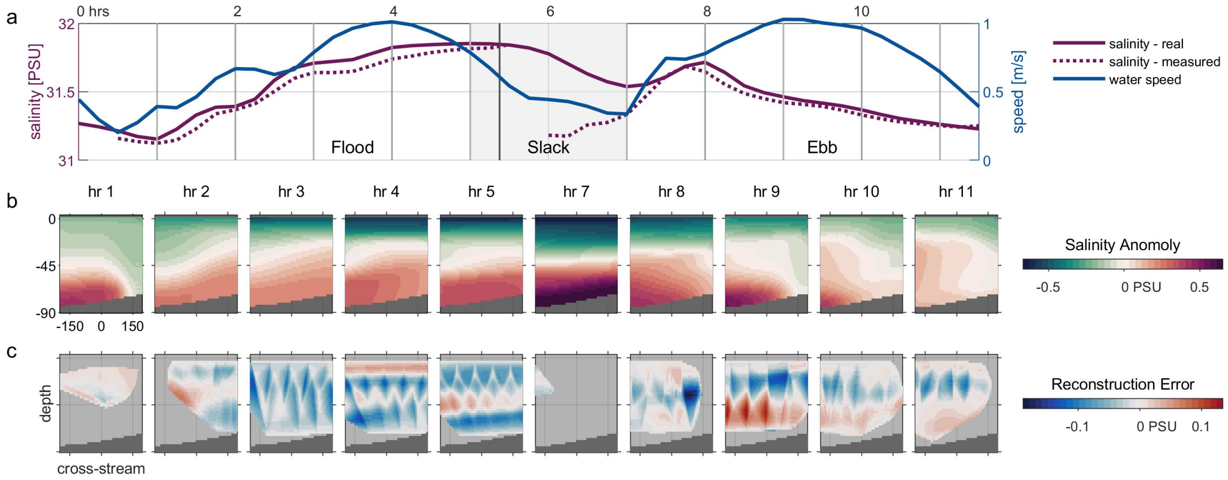

Figure 2.10: Reconstruction error of salinity field. (a) shows the time series of the true salinity (solid purple), the float measured salinity (dashed purple), and magnitude of the horizontal water currents (solid blue) over the weak-neap exchange (all are median values evaluated over the survey volume). Rows (b,c) are snapshots of the cross-stream vertical plane (Fig. 2.4) centered on the stationary ADCP location, with the dark gray region indicating the seafloor. Thus, floats in stream-wise currents move into the page. Salinity anomaly (b) is the spatially demeaned field at the indicated time step. Reconstruction error (c) is the difference between the measured and true salinity field at all evaluation points in the survey volume. For the reconstruction, light gray regions indicate unmeasured portions of the survey volume due to insufficient float coverage.

ADCP surveys perform best, followed closely by float swarms, and then, more distantly, stationary ADCPs and X-band radar. X-band radar does, however, provide significantly greater coverage than any other platform and has a low incremental cost for relatively long survey durations. Radar accuracy can be significantly improved by simultaneously deploying a stationary ADCP to provide information about the vertical velocity structure, overcoming the primary limitations of both platforms. While a mobile ADCP is likely the best choice for surveying currents at these scales (range $O(1\text{ km})$, resolution $O(10\text{ m})$), floats can simultaneously gather co-temporal scalar quantities, such as temperature, salinity, and dissolved oxygen. Even though this study is specific to a tidally-dominated environment, accurate volumetric reconstructions in any environment require measurements that adequately sample horizontal and vertical gradients.

Chapter 3

THE μFLOAT SYSTEM

With the simulated field studies from Chapter 2 indicating that an operationally feasible number of floats could map tidal currents and other water properties with high resolution and accuracy on par with traditional methods, the next step was to identify a float suitable to the task. As discussed in Section 1.4, there were no commercial or academic floats readily available that matched the economical and technological requirements associated with a coastal float swarm. This technology gap motivated the development and construction of the μFloat system.

The objective of this chapter is to review the design requirements for coastal floats and to introduce the μFloat system. Special attention is given to the buoyancy engine and underwater localization, as these subsystems lay the foundation for quality data products. Performance of these key subsystems is subsequently benchmarked in Chapter 4.

3.1 Design Requirements of a Coastal Float Swarm

As outlined in the Section 1.4, the primary requirements of a coastal float suitable for swarm deployments are as follows:

1. *Sensing Scales:* Coastal waterways are typically less than 200 m deep. Here, we targeted a working depth of 100 m. Horizontal domains are typically O(1-10) km. Highest resolutions of interest are O(1-10) cm in the vertical and O(1-10) m in the horizontal. Dynamics of interest have timescales ranging from minutes to years. As floats are not necessarily well-suited to maintaining persistence in a particular region, short duration (O(1) hour - O(1) day) studies of energetic processes (e.g., tidal currents) were emphasized for this design.

2. *Buoyancy Control:* The float must have sufficient buoyancy engine capacity to auto-ballast in response to water density variations (max 3% change from river to ocean water). To enable vertically distributed sampling, the float must be able to hold depth to within 1 m over its entire depth range (100 m) in both stratified and well-mixed environments. The float must be able reach target depths on operationally relevant time scales, particularly for deployments in energetic tidal channels. The float should have spare buoyancy engine capacity to accommodate external sensors.

3. *Underwater Localization:* Mapping subsurface currents with float swarms requires tracking the float while underwater. As GPS does not function subsurface, an alternative underwater localization system is necessary. Higher position accuracy and sample rates will decrease (make smaller) the minimum length scale resolvable by the floats. An accuracy of 10 m was targeted as a scientifically relevant but achievable first step. To match survey extents, the horizontal range of the underwater localization system should be at least 1 km.

4. *Sensors:* The float should be equipped with a basic sensor suite such that volumetric measurements of *in situ* water properties (e.g., temperature) can be demonstrated.

5. *Economic:* The unit cost of the float (and any secondary equipment necessary for localization) must be inexpensive enough such that production in multitude is possible for an individual research group. Here, a full system cost of less than $100k was targeted.

6. *Logistics:* To ensure operational flexibility and low survey costs, floats should be easily manageable by a single person. Deployment should not require any specialized vessels or equipment. As floats may move rapidly through the region of interest, they must be recoverable and redeployable. The float should have sufficient power to gather data for at least one day.

3.2 A Review of Float Dynamics

Design of a coastal buoyancy-driven float is constrained by float dynamics. In the vertical direction, these are governed by the balance of inertia, mass, buoyancy, drag, and external flow-field accelerations, and can be expressed as follows:

$$(m_f + m_a)\frac{\mathrm{d}U_f}{\mathrm{d}t} = -m_f g + \rho_w V_f g + \frac{1}{2}\rho_w A C_d (U_w - U_f)|U_w - U_f| + (\rho_w V_f + m_a)\frac{\mathrm{D}U_w}{\mathrm{D}t}. \quad (3.1)$$

Here, m_f is the mass of the float, m_a is the added mass of the float, V_f is the total volume displaced by the float, g is acceleration due to gravity, and ρ_w is the water density. U_w and U_f are the velocity of the water and float, respectively. A and C_d are the float's cross-sectional area and coefficient of drag. Here, drag is represented in typical quadratic form, but in conditions of strong density stratification and low relative float speeds, a linear treatment may be more appropriate [27, 38]. The $\frac{\mathrm{D}U_w}{\mathrm{D}t}$ term describes the accelerations of the surrounding flow, however only those fluctuations with length scales greater than the characteristic length of the float will contribute to float motion [30]. Dynamics in the horizontal are the same as described for the vertical, save the elimination of gravity and buoyancy terms. For a given size, flow-following is improved by maximizing drag, as it always acts to counter relative velocity between the float and surrounding water. This can be achieved through addition of a sail [27], though such modifications must be approached carefully, as such drag surfaces may increase inertia due to added mass. A derivation of Eq. 3.2 is included in Appendix A.

To move vertically in the water column, nearly all modern floats actively control float volume V_f. In quiescent water, ($\frac{\mathrm{D}U_w}{\mathrm{D}t} = U_w = 0$), we can rewrite Eq. 3.2 in terms of the nominal float volume V_o and time varying buoyancy engine volume $V_{BE}(t)$

$$(m_f + m_a)\frac{\mathrm{d}U_f}{\mathrm{d}t} = -m_f g + \rho_w g(V_o + V_{BE}(t)) - \frac{1}{2}\rho_w A C_d U_f |U_f|. \quad (3.2)$$

If we decompose the buoyancy engine volume into two parts, defining a constant neutrally buoyant volume $V_{BE,NB}$ such that $\rho_w(V_o + V_{BE,NB}) = m_f$ and time varying movements ${V'}_{BE}(t)$ around that volume, we can rewrite Eq. 3.2 as

$$(m_f + m_a)\frac{\mathrm{d}U_f}{\mathrm{d}t} = \rho_w g {V'}_{BE}(t) - \frac{1}{2}\rho_w A C_d U_f |U_f|. \tag{3.3}$$

Thus, terminal velocity ($\frac{\mathrm{d}U_{f,z}}{\mathrm{d}t} = 0$) is determined by the balance of buoyancy engine offset from neutral and hydrodynamic drag and is a dynamically stable state for a given buoyancy engine offset volume. Assuming a symmetric shape and drag coefficient, $V_{BE,NB}$ must be near 50% of the total buoyancy engine volume to ensure a similar maximum dive and rise speed. This can be achieved via pre-deployment ballasting.

Buoyancy engines provide several possible control modes: profiling, isobaric/depth control, and isopycnal/Lagrangian control. Vertical motion provides the basis for profiling, the standard data-gathering mode of the Argo floats [168]. Isobaric (constant pressure) control can be achieved with feedback from a pressure sensor. Isobaric control also serves as an excellent proxy for depth control, accurate to within 3% of the total water depth (maximum likely error between an assumed and actual density). If knowledge of absolute depth is critical, additional conductivity and temperature sensors can provide an estimate of density through the water column during decent, though when deployed in a dynamic environment, the float may advect to a region with new conditions. Such isobaric or depth control provides the ability to drift with horizontal currents, sampling a particular layer of interest, while actively compensating for changes in site density. Similar to depth control, constant altitude control can be achieved with a bottom-tracking altimeter and enables visual benthic surveys and terrain-based odometry [121, 18, 17, 118].

Isopycnal (constant density) control relies on local vertical density gradients to provide a dynamically stable ‘parking depth.’ This was the control mode of the original Swallow floats [142], as it requires no active control in a stably stratified environment: the float descends until settling at the isopycnal surface corresponding to its density. On short time scales, such a float is the closest approximation to Lagrangian, as vertical water currents will induce excursions uninterrupted by active control schemes. On long time scales, the float will return to the dynamically stable isopycnal surface [38]. However, to ensure passive stability, increases in float density due to compressibility (i.e., reduction in float volume V_o due to increased hydrostatic pressure) must not be greater than those in the surrounding water [27, 39]. Additionally, isopycnal control requires a sufficiently strong density gradient and is thus unreliable in well-mixed waters (e.g., tidal channels).

3.3 System Overview

The prototype μFloat swarm sensing system is comprised of twenty-five buoyancy-controlled μFloats (Fig. 3.1a) and five GPS-tracked surface buoys (Fig. 3.1b) that provide underwater localization.

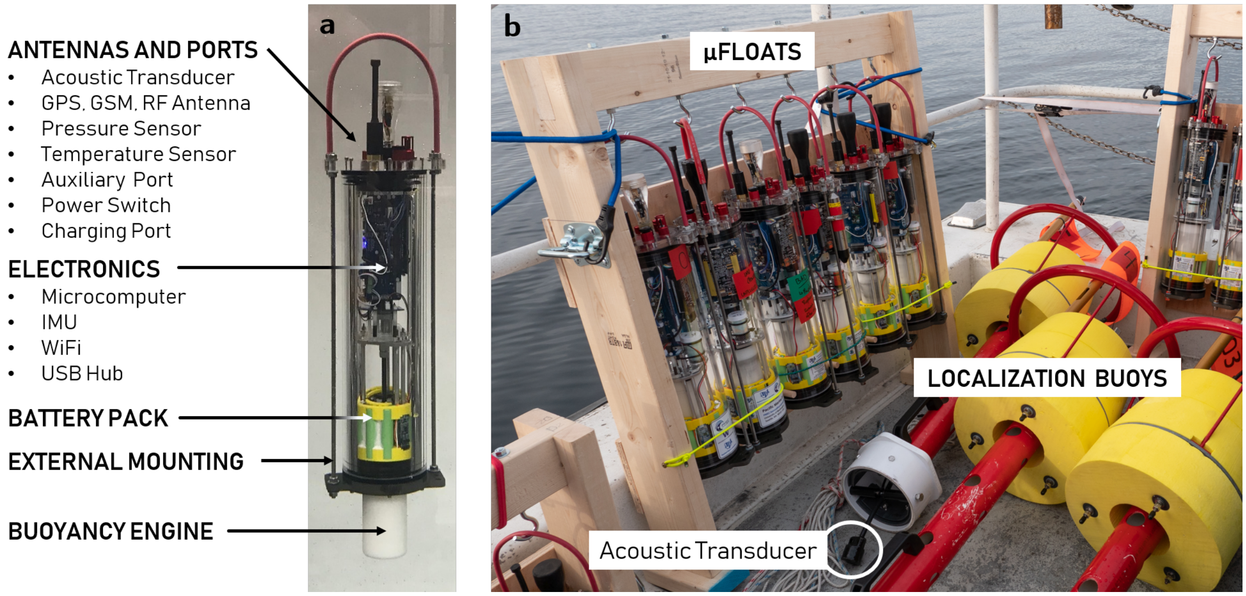

Figure 3.1: μFloat sensing system: (a) μFloat with annotated subsystems; (b) a rack of six μFloats and three surface localization buoys prior to deployment. Note the acoustic transducer extending from the bottom of the buoy spar.

3.4 μFloat Architecture

The μFloat (Fig. 3.1a) was designed to be as small as possible to increase the Lagrangianness of the float while respecting constraints for low-cost electronics, sensor suite expansion, and buoyancy engine capacity for coastal missions. To minimize cost, commercial-off-the-shelf parts were used where possible and custom pieces were designed for ease of production and assembly. The main housing is a 10 cm (4") diameter, 40 cm long acrylic tube with double O-ring flange seals (Blue Robotics) with custom endcaps. The buoyancy engine is comprised of a solid acetal (Delrin) piston that extends through a T-ring seal in the bottom endcap. The piston is actuated by a lead screw which is driven by a brushed DC motor with planetary gearbox (ServoCity) and motor controller (Pololu). Piston position is inferred by a quadrature encoder attached to the motor shaft. Limit switches are mounted at both extents of the piston position to prevent over-extension. The nominal volume of the float (piston fully retracted) is 4700 cm^3. The piston can change the volume by 450 cm^3 (± 10 cm^3 due to manufacturing variations between floats), which translates to a 9% change in total displaced volume. While additional drag surfaces could improve the Lagrangianness of the μFloat, they were omitted in the interest of operational simplicity.

The μFloat is controlled by a single-board computer (Beaglebone Black) running a Linux-Debian operating system that supports mission control, sensor telemetry, and data acquisition. When on board, programming and data offload occur via WiFi. All system status and sensor data are recorded to a 32 GB micro SD card. A GPS receiver (Adafruit) provides global position and PPS clock synchronization while on the surface. For recovery, coordinates are transmitted to a support vessel via redundant 900 MHz RF radio (XBee) and cellular (Particle Electron) modems. These communication methods also allow short data messages and commands to be exchanged among floats and the support vessel, such that floats can be re-tasked without physical retrieval. For underwater localization, we implement a system based on nanomodems [43, 106], an inexpensive (< \$200 US) underwater acoustic modem (further details in Section 3.6). An onboard inertial measurement unit (IMU) records orientation and acceleration (translational and rotational). While currently used for diagnostic purposes (e.g., revealing bottom interactions), the IMU data will eventually be used for inertial navigation to improve localization accuracy between acoustic position updates. Additional USB, serial, analog, and I^2C connections are available for auxiliary sensor integration. The top endcap hosts a pressure sensor (Honeywell) and temperature sensor (BlueRobotics). The GPS patch antenna, nanomodem acoustic transducer, and RF and cellular antennas are potted in a single, custom unit. Additionally, a charging plug, vent plug, auxiliary port and power switch are all located on the top end cap. Power is provided by a rechargeable Li-ion battery pack with ∼100 W-hr capacity. The hotel load consumes about 3-5 W, resulting in a maximum endurance of 20-30 hr.

3.5 μFloat Control

The μFloat is equipped with an isobaric controller that uses feedback from the pressure sensor. For sake of improved readability through the remainder of this dissertation, we will refer to this as depth control, rather than isobaric control, noting that pressure in dbar and depth in m are interchangeable within an accuracy of 3%. Floats are ballasted to be within 50 g of neutral buoyancy with their piston halfway extended in fresh water. While not strictly necessary, we install nominal calibrated weights when deploying in salt water to maintain balanced bidirectional performance of the buoyancy engine. Prior to deployment, a predefined schedule of target depths and associated durations at those targets is constructed. Using a graphical-user-interface (GUI) developed in MATLAB (Mathworks®), the schedule is uploaded to multiple floats simultaneously via WiFi. During a dive, depth control is achieved via a closed loop two-stage cascaded proportional-derivative (PD) controller (Fig. 3.2). In the first stage, the current position error (target depth minus current depth) is calculated. A recommended velocity is then computed based on PD_z gains and checked against a user-defined speed limit (V_{limit}), and finally outputs a target velocity. The second stage evaluates the current velocity error (target minus current) and computes the output motor command (with check for minimal and maximal values) based on PD_v gains. Float depth and velocity are tracked with the pressure sensor. A digital Butterworth filter reduces pressure sensor noise, though induces a one-second lag in the feedback loop. Current velocity is computed via a digital differentiation of the pressure signal. To mitigate errors due to absolute drift of the pressure sensor (< ± 0.5 dbar/hour, ± 1 dbar max), we sample ambient pressure whenever the float surfaces and compute dive pressure (depth) relative to the most recent surface pressure. Gains (PD_z and PD_v) were manually tuned to minimize time to target depth and maximize depth-holding stability in a series of shallow water tank trials. The gains were held constant for subsequent testing. The velocity limit ($\mathrm{V}_{\mathrm{limit}}$) was included to provide controllable profiling rates and improved transient dynamics and was a primary variable investigated in the benchmarking of μFloat buoyancy engine performance (Chapter 4).

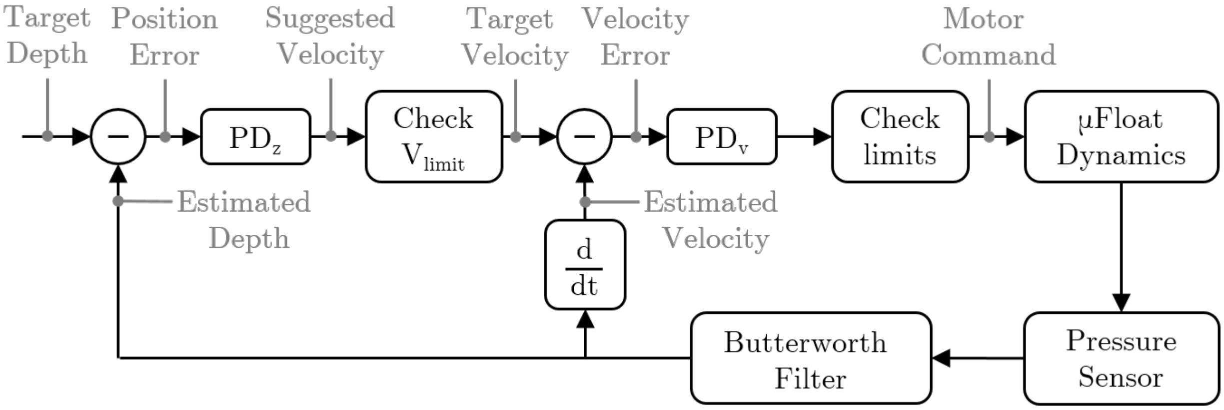

Figure 3.2: Block diagram of μFloat depth control. Control scheme is closed-loop, two-stage, cascaded proportional-derivative (PD) controller with feedback from the pressure sensor. Inputs are target depth and velocity limit V_{limit} for constraining vertical speed.

3.6 Localization

Floats are tracked via GPS when on the surface. For subsurface positioning, we utilize a network of surface localization buoys (SLBs) equipped with acoustic nanomodems (Fig. 3.1b). A minimum of three SLBs, either moored or drifting, provide a long-baseline style localization architecture [136]. Surface buoy electronics are a simplified subset of the μFloat's, similarly contained within an acrylic housing (Blue Robotics). The external structure consists of buoyant yellow foam upper and a subsurface spar (1 m long) from which the nanomodem transducer extends. SLBs can be moored or allowed to drift.

Nanomodems (v2) exchange messages on a carrier frequency band of 24-28 kHz, have a maximum data rate of 40 bit/s, and a nominal range of 2 km [43, 106]. The nanomodems were chosen as they met the communication requirements necessary for underwater localization at significantly lower cost (10x) than other commercially available acoustic modems. For localization, SLB nanomodems sequentially broadcast pings (0.275 s duration) coded with a unique ID in a round robin fashion, as this version of the hardware cannot parse overlapping messages. All nanomodems within broadcast range (i.e., both those on subsurface μFloats and on nearby SLBs) record and timestamp received pings. Post-processing steps proceed as follows and are evaluated on both SLBs and μFloat nanomodem records. Further details on these processing steps are located in Appendix C.

1. *Clean incorrectly labeled pings.* Due to interference experienced along the transmission path (ambient noise, multipathing), a considerable percentage (5-30%) of the received pings are incorrectly labeled. In post-processing, these erroneous messages are corrected by assigning the ping label expected according to the the programmed ping schedule and GPS-based estimates for message time-of-flight.

2. *Align sent and received ping.* The received ping timestamps are aligned with their corresponding sent timestamp.

3. *Compute time-of-flight from aligned timestamps, adjusted for software delays.* Software delays in ping timestamping were characterized by measuring send-receive delays with 7 cm nanomodem transducer separation in fresh water for each float-buoy pair. The fleet-average software delay was 73.1 ± 0.2 ms and remained constant over time.

4. *Calculate horizontal distance based on acoustic path length using an assumed or mea-*

sured sound speed. We multiply the time of flight by the local sound speed to calculate the acoustic path length L_a. Assuming this length is the direct path between source and receiver, the path is projected into the horizontal distance L_h by accounting for the source depth z_s and receiver depth z_r, i.e. $L_h = \sqrt{{L_a}^2 - (z_s - z_r)^2}$.

5. *Trilaterate float position from horizontal acoustic path lengths and SLB GPS locations.* Using distances from all unique pings within the round-robin cycle period, trilaterate the μFloat position by least-squares fit [111]. This assumes negligible μFloat motion within round-robin period and synchronized clocks between μFloats and SLBs.

6. *Remove egregiously incorrect localizations.* The resulting localizations are intermittent, noisy, and can indicate physically unrealistic float motion. Consequently, we first remove any localizations outside the domain, defined as being anywhere on land, or outside a physically realistic distance from last known GPS position assuming a nominal advection speed.

7. *Smooth acoustic localizations into physically realistic tracks.* To produce physically realistic tracks, we combine GPS data from times on the surface with acoustic localizations when subsurface into a single data series. We smooth the compiled track using a robust (outlier-rejecting), locally-weighted, quadratic regression (MATLAB 'smooth' function with 'rloess' option). Due to the gappy nature of the localizations, the smoothing window is programmatically adjusted for each float such that, over a given track, at least 60% of windows include at least ten points in the regression. Window span varies from 60-240 seconds at 60 second discretization. Only points at which localization data exist are retained.

8. *Compute track velocity.* To estimate velocity along the track, we apply a first-order central-difference scheme to the previously smoothed data. To ensure estimates at sparsely distributed position data, we linearly interpolate between smoothed position

data prior to differencing, but retain velocity data at only at points where localization data exist.

It is important to note that this time-stamped approach depends on synchronized clocks. Both SLB and μFloats clocks are synchronized to the GPS pulse-per-second output while on the surface. When subsurface, the μFloat clock (crystal oscillator on the Beaglebone Black) has a maximum drift of 30 parts-per-million, such that after 30 minutes underwater, the maximum offset expected is 0.054 s. Additionally, the assumption of negligible float movement between pings depends on the ping rate and water velocity. In Agate Pass, maximum velocities were 2 m/s and ping rate was 1 second. As three pings are required for localization, float position may change up to 6 m within a given ping set.

Chapter 4

μFLOAT PERFORMANCE EVALUATION IN QUIESCENT AND ENERGETIC ENVIRONMENTS

The overarching purpose of the μFloat swarm is to provide distributed, simultaneous measurements in coastal waterways. However, prior to using the swarm in a scientific context, acceptable performance must be established. This chapter describes the tests undertaken to benchmark critical μFloat subsystems, the buoyancy engine and underwater localization. Results are discussed in the context of scientific applications and compared against the capabilities of existing floats. The objective of this chapter is to establish the effectiveness of the μFloat swarm as a scientific platform.

One of the benchmarking tests presented is a full-scale swarm deployment in an energetic tidal channel. While the scientific outcomes of this deployment are the primary subject of Chapter 5, results for buoyancy engine and localization performance are presented here to provide a more direct comparison between performance in quiescent and energetic environments.

4.1 Evaluation Objectives

As is essential for all newly developed instruments, the μFloat system requires validation to establish confidence in its data products. Benchmarking tests were designed to evaluate system performance according to the objectives described in Table 4.1.

These objectives were primarily selected to provide a thorough description of system performance as relevant to tidal current measurements. Additionally, we sought to characterize baseline functionality generally applicable to future scientific objectives. The specific performance implications of each metric are discussed as the results are presented.

Table 4.1: μFloat Performance Evaluation Objectives

Buoyancy Engine	**Evaluation Objective**
Transient Response	Determine time to target depth, overshoot, and maximum profiling speed.
Isobaric/Depth Holding	Determine accuracy and stability during depth holding period.
Disturbance Response	Determine ability to hold depth in dynamic environments (e.g., vertical currents in upwelling or local water density changes)
Compressibility	Determine how much float compresses with depth and corresponding feasibility of isobaric/Lagrangian control mode.
External Sensor Capacity	Demonstrate adaptability to new scientific applications and identify any associated controller tuning requirements
Underwater Localization	
Connectivity	Determine what percentage of sent messages are received and dependence on distance, receiver depth, source depth, local sound speed, and ambient noise.
Horizontal Position	Determine the accuracy of underwater positioning and primary sources of error.
Horizontal Velocity	Determine the accuracy of velocity estimates based on position data and the primary sources of error.

4.2 System Tests

A series of indoor tank tests and field tests from late 2018 through 2020 were undertaken to evaluate performance of the μFloat system according to the previously described objectives. We restrict our attention to a subset of those tests (Table 4.2) that demonstrate the current performance characteristics. These were performed in a salt water tank, a quiescent freshwater lake (Lake Washington), and energetic tidal channel (Agate Pass). The salt water tank test examined how the isobaric control responds to environmental disturbances (e.g., upwelling, density changes). In the Lake Washington tests, we evaluated the buoyancy engine and localization in a nominally quiescent environment. In Agate Pass, we demonstrated a swarm deployment of twenty μFloats in a high-energy tidal channel to volumetrically map tidal currents. As previously discussed, results from the Agate Pass test presented in this chapter are limited to evaluation of the buoyancy engine and localization performance, while the composite performance of the swarm is presented in Chapter 5.

Table 4.2: μFloat performance benchmarking tests

Date	Objective	Location	# μF	# SLB	c_{sound} m/s	Density kg/m^3
27 July 2020	Isobaric Control Localization	Lake Washington (Quiescent)	20	5	1455	1000
8 Jan 2021	Isobaric Disturbance Response	Salt Water Tank (Quiescent)	2	N/A	~	1030
20 Aug 2020	Tidal Channel Swarm Demonstration	Agate Pass (Energetic)	24	5	1500	1022

4.2.1 Lake Washington - Quiescent Water

Quiescent-flow field tests were conducted on 27 July 2020 in Lake Washington, WA, a large freshwater lake with a muddy bottom and a depth of 30-65 m in the testing region, representing an appreciable range of the intended operating depths (up to 100 m). Winds were light

(1-2 m/s) and varied from SE to S over the course of the day. Two test periods occurred during the test day, with layouts as pictured in Figure 4.1. Test 1 lasted approximately 2 hours, during which twenty μFloats were deployed simultaneously along with five SLBs. Test 2 lasted approximately 30 minutes, with two μFloats deployed with five SLBs. Prior to testing, a profile of water density and sound speed were measured (Valeport miniSVP), revealing a strong thermocline (Fig. 4.1b).

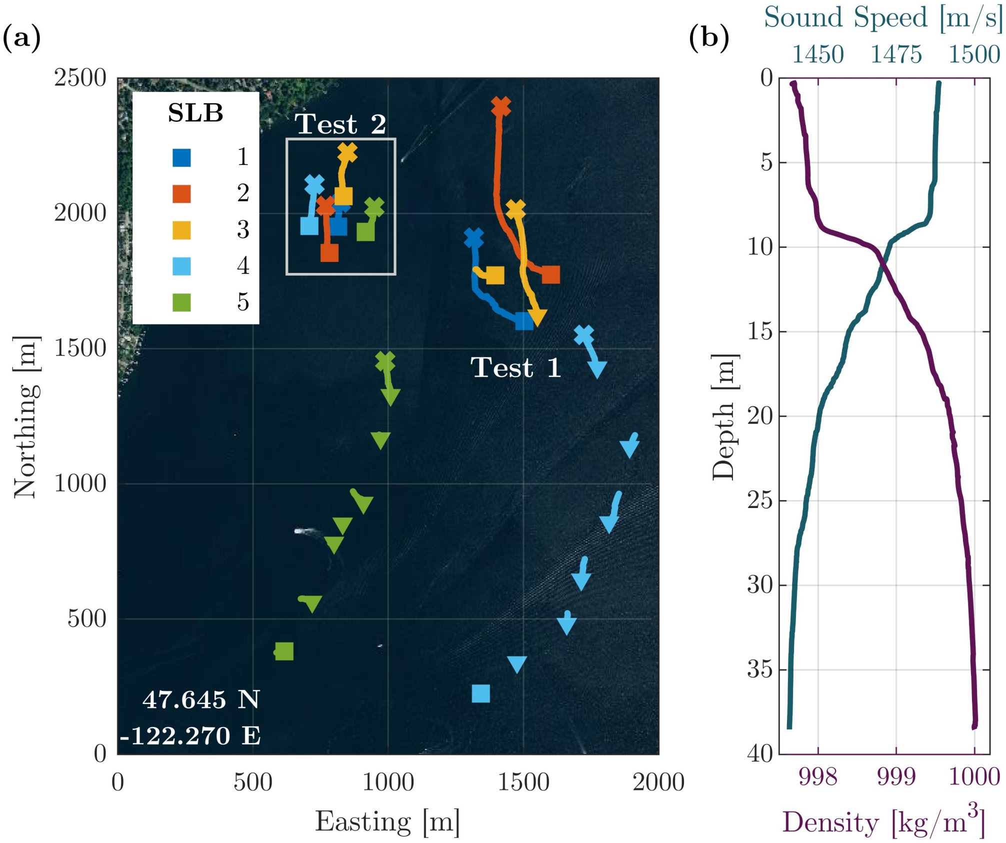

Figure 4.1: Layout of surface localization buoys (SLBs) (a) and sound speed and density profiles (b) during Lake Washington tests. ■ and ✖ mark the starting and final locations, respectively, for each test. SLBs were manually relocated during Test 1, with ▼ marking each new starting location. Twenty μFloats were deployed in the center of the triangle formed by SLB 1-2-3 in Test 1, and two floats nearly collocated with SLB 1 in Test 2. SLB movement was wind-driven, with light wind (1-2 m/s) varying from SE to S over the course of the day.

Depth Control

During Test 1, μFloats were deployed with a pre-programmed depth schedule designed to assess the transient dynamics and depth-holding accuracy of the buoyancy engine. The lake depth permitted control assessment over approximately half the float range, with target depths varying from 2.5 m to 42.5 m. The velocity limit control parameter (Fig. 3.2) ranged from 0.2 m/s (slow) to 1.0 m/s (effectively unrestricted). Test 2 had no depth control evaluation component.

To assess depth control performance during Test 1, the dive sequence was parsed into actions (any move from one depth to another). From each action, we computed the following metrics: (1) settling time - the elapsed time between when the float moved 0.25 m from its starting depth to settling within 0.25 m of the target depth for at least 30 seconds; (2) overshoot – the max deviation (m) from the target depth prior to settling; (3) depth-holding accuracy after settling, assessed as offset from target depth; and (4) deviations from the settled depth. Actions with steady-state periods less than 30 seconds were excluded due to lack of statistical convergence.

Localization

During both Lake Washington tests, the acoustic localization array was comprised of five SLBs (Fig. 4.1a). Nanomodem pings from each of the five SLBs were scheduled in a round robin fashion, each offset from the previous by two seconds, with a pause after the fifth ping, thus each pinged once every twelve seconds. Test 1 evaluated maximum broadcast range and connectivity. As such, three SLBs were deployed in an equilateral triangle (∼200 m on edge) around the floats to provide consistent localization data through the experiment. Two additional SLBs (4,5) were initially deployed about 1600 m distant and moved sequentially closer to the floats over the course of the two-hour deployment.

Test 2 was performed to evaluate optimal localization accuracy, with all five floats deployed in a + shape, with a maximum separation distance of 300 m. Additionally, to assess horizontal position uncertainty, two floats were programmed to ground themselves on the bottom for fifteen minutes, following [17].

Underwater localization relies on the receipt of pings from a minimum of three surface buoys within a short time period and is thus impacted by the underlying ‘connectivity’ between source and receiver. We evaluated connectivity as the ratio of received pings from a single SLB to pings sent by that SLB over a one minute interval (potential for 5 received pings). This metric was calculated for each combination of surface buoy and μFloat. To contextualize the relationship between connectivity, received signal strength, and ambient noise, four μFloats were deployed with an externally mounted hydrophone (OceanSonics icListen HF). The acoustic data were processed in MATLAB (Mathworks®) to extract pressure spectral density levels over the duration of the test. As a measure of ambient noise in the transmission band, we calculated the 10-second moving-median sound pressure level (SPL) within the 24-28 kHz frequency band. Pings appeared as short, distinct elevations of SPL in the transmission band. Pings were located using a matched filter and the received level for each ping was calculated as the root-mean-square SPL over the duration of the ping. The hydrophone time series was manually aligned to μFloat time series. The nanomodem pings recorded on the hydrophone were then labeled with their corresponding source SLB by reference to the known ping schedule. Additional details on hydrophone processing are provided in Appendix B.

The ultimate goal of the nanomodem array is to accurately estimate the horizontal positions of subsurface μFloats. Because the true location of the floats is unknown while underwater, system accuracy is assessed by examining acoustic localizations of the SLBs, as compared to their ‘true’ GPS data. From a localization standpoint, the SLBs are functionally equivalent to μFloats holding depth at 1.5 m. To isolate the influence of the source geometry on localization accuracy, we also applied the localization algorithm using the GPS-measured distances between source and receiver SLB as input to the trilateration process.

A comparison of acoustic path distance to GPS-estimated separation revealed that nearly 60% of nanomodem pings that were received on SLBs were suspected of following a transmission path that included a bottom reflection (i.e., time of flight substantially longer than direct path). This was unsurprising given the strong thermocline (Fig. 4.1). For those messages with suspected reflections, we computed the direct path distances by assuming a nominal depth and a triangular path from source to bottom to receiver. For additional details, see Appendix C.2.

To generate a 'true' position reference for all SLBs, their raw (1 Hz) GPS data was smoothed using a low-pass filter with 0.0167 Hz cut-off frequency (60 second period). A first-order central-difference scheme was applied to the smoothed position data to provide the 'true' horizontal velocity reference.

Compressibility

The float dive series during Test 1 also permitted evaluation of compressibility, defined as the relation between float volume and ambient pressure. Compressibility is critical to the dynamic stability of the float [27, 38] and directly impacts how frequently the piston must actuate to maintain constant depth. Consider a compressible float at depth that is neutrally buoyant and maintaining a constant piston extension. If the compressibility of the float is greater than that of the surrounding water, a slight upward movement of the float will cause float density to decrease more than the surrounding water, resulting in a positive buoyant force, pushing the float further away from the starting depth. Such a situation requires constant piston actuation to maintain the target depth. Conversely, a float that is less compressible than the surrounding water will experience a restoring force if perturbed and will thus be dynamically stable at the target depth without piston actuation. Such is the behavior of an isopycnal float. A similar dynamically stable state can occur if the water density has sufficient vertical stratification to compensate for the buoyancy lost due to float compression.

To characterize μFloat compressibility, we examined how the neutral-buoyancy piston position – the average position of the piston when holding depth – changes with hydrostatic pressure. Given the mass of the float remains constant, if the nominal float volume decreases due to compression, the piston must correspondingly extend to make up for the lost buoyancy and thus maintain neutral buoyancy. To assess float compression, we computed the difference between neutral buoyancy piston volume at 2.5 m (reference volume) and the volume for neutral buoyancy at greater depths z, normalized by the nominal float volume V_o. That is,

$$\%\Delta V_o = 100 \times \frac{V_{pist,NB,z} - V_{pist,NB,2.5m}}{V_o} \tag{4.1}$$

To relate this to water density variation, we multiplied the percentage change in volume by a reference density (1 kg/m^3 – fresh water at 15 °C), such that the compressibility metric can be interpreted as the change in nominal float density as a consequence of increasing hydrostatic pressure.

Auxiliary Sensors

The μFloat was designed to easily accommodate additional external sensors. To demonstrate this capacity and gather supplementary data, several floats were equipped with external sensors during field tests. These include the four floats with hydrophones and three floats with cameras (GoPro Hero 6 and Session 5) for visual examination of float performance and demonstration of swarm video capture.

4.2.2 Salt Water Tank - Disturbance Response

The μFloat was designed to be deployed in high energy sites with strong velocity gradients, including upwelling, as well as accommodate transitions from fresh to salt water without re-ballasting. To approximate buoyancy controller response to such disturbances, we performed calibrated tests in an indoor salt water tank (salinity 33 ppt, density 1024 kg/m^3) with dimensions 3 m x 5 m x 4 m (length, width, depth). Floats were programmed to hold 1.5 m depth for the duration of the test. While the float was holding depth, a diver placed external weights on the top endcap of the float. The magnitude of these weights were chosen such that they matched the forces imparted by a variation in water density (slow change) and upwelling currents (fast change). Specifically, a float traveling 2 km at 1.5 m/s from a fresh river mouth out to a salty bay would experience a 2% change in density over 20 minutes, equating to an approximate increase in buoyant force of 4 g/minute. To emulate this, divers added 3 g every 30 seconds for 20 minutes, with a total of 106 g added. Similarly, a float entering an upwelling current would experience a change in hydrodynamic drag proportional to the current speed. This drag force change was emulated by applying an equivalent change in ballast weight. For the μFloat, a sudden 10 g (60 g) change in weight equates to a 0.1 m/s (0.3 m/s) change in relative float velocity. Thus, divers added and removed 7 g, 13 g, 26 g, 39 g, and 52 g weights. While the float can theoretically counteract upwelling up to 0.5 m/s (just below terminal velocity of the float) corresponding to a ballast change of 170 g, the tank depth was insufficient to emulate this velocity. Testing was performed on two floats and repeated for controller velocity limits (Fig. 3.2) of 0.2, 0.3, 0.4, 0.5, and 1.0 m/s (effectively unlimited). Note that all weights indicated here are wet weights. For the slow disturbance data series, the depth-holding deviation (interquartile range around settled depth) was evaluated during the undisturbed and disturbed periods. For the fast disturbance test, we computed the peak deviation from the settled depth and excursion duration (time spent at greater than 0.1 m from settled depth).

4.2.3 Agate Pass - Energetic Tidal Channel Deployment

The first full-scale scientific demonstration of the μFloat swarm was mapping horizontal water velocities in Agate Pass, WA, a tidal channel approximately 10 m deep and 300 m wide, with currents often exceeding 1.5 m/s. On 20 August 2020, twenty floats were repeatedly deployed over an ebb-flood tidal cycle, with underwater periods lasting twenty minutes (Fig. 4.2). As the primary objective of these surveys was to perform volumetric field characterizations, μFloat settings and SLP arrangements were determined accordingly. Based on results from Lake Washington, a velocity limit of 0.3 m/s was implemented on all floats. For a given survey, all floats were programmed to hold depth (targets varied from 1-10 m) or to repeatedly profile from the surface to depth (maximum depths varied from 3-10 m). SLPs were deployed to maintain consistent underwater localization for the swarm. Auxiliary sensors were identical to those described for Lake Washington tests. GoPros were oriented looking downward and augmented with dive lights to survey the benthos, a much simpler version of [121]. During each deployment, water density and sound speed were measured mid-channel, near the bridge (Xylem CastAway CTD) and revealed minimal gradients (Fig. 4.2b). Additional details are provided in Chapter 5.

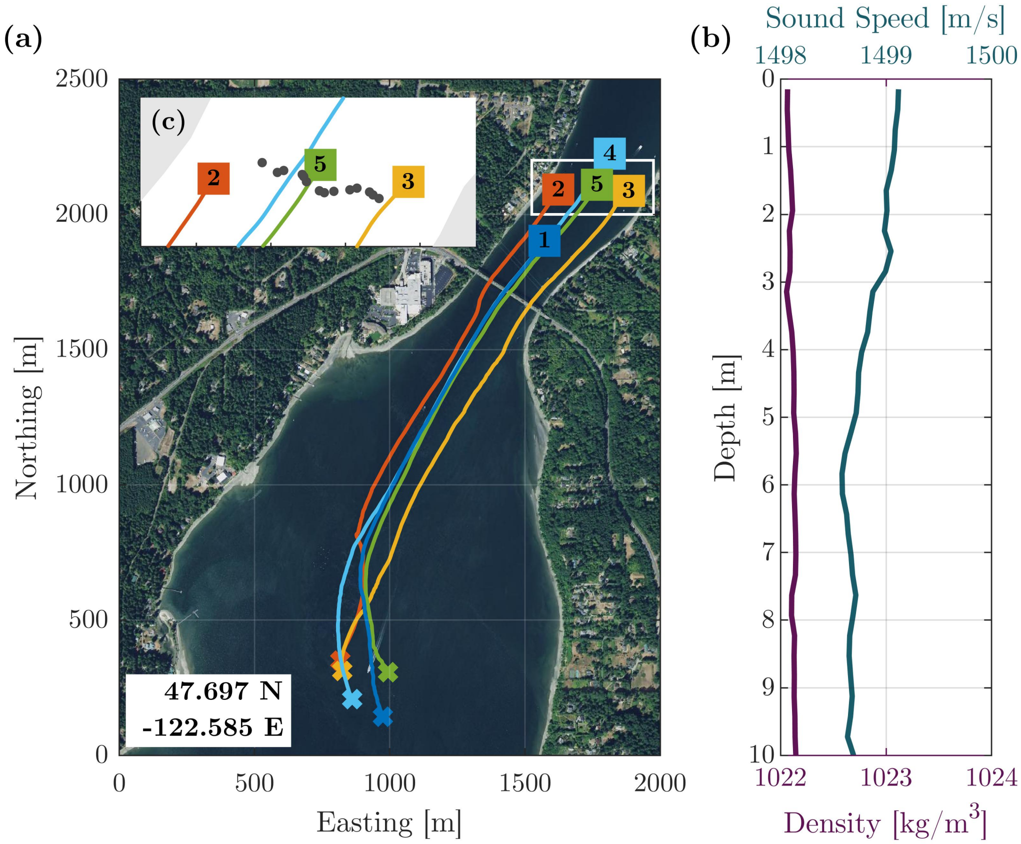

Figure 4.2: μFloat system deployment in Agate Pass during flood tide (a) and water density and sound speed as a function of depth during the test interval (b). ■ and ✖ mark the starting and final locations of the SLBs, respectively. μFloats, indicated by the grey dots in (c), were deployed moving westward from SLB 3 to SLB 2 and followed trajectories similar to the SLBs.

While performance benchmarking was not the primary objective during Agate Pass tests, the field results nonetheless demonstrated how the system performs in an energetic environment. As such, float dives were analyzed using the same process as for Lake Washington tests (Section 4.2.1) to evaluate depth control performance. Due to the water movement, the 0.25 m tolerance threshold for defining the start of the settled period used in Lake Washington was relaxed to 0.5 m for Agate Pass data. Note that all depth-holding tracks were included in the analysis, but profiling deployments were excluded. Localization analysis followed the same process as Lake Washington tests. A comparison of GPS and acoustic path lengths indicated no distinguishable bottom-reflections, which was consistent with the well-mixed, shallow (<10 m) nature of the channel. Analysis of localization accuracy in Agate Pass is restricted to a single flood deployment, as pictured in Figure 4.2a. Composite swarm data products are presented and discussed in Chapter 5.

4.3 Results

4.3.1 Depth Control

Figure 4.3 shows a representative float trajectory for a range of target depths during the Lake Washington trial. Figure 4.4 provides a detailed view of the transient response as a function of time for different velocity limits and changes in target depth. Figures 4.5a,b provide fleet-wide statistics for these metrics in Lake Washington, as well as results from Agate Pass.

For depth changes less than 20 m (e.g., Fig. 4.4 - left column), settling time is independent of the velocity limit, while overshoot increases with larger velocity limits. However, when depth changes are about 20 m or larger, the relationship between the velocity limit and the transient response becomes more idiosyncratic and trends in overshoot and settling time are more ambiguous. For these larger depth changes with relatively high velocity limits ($\geq$ 0.5 m/s), the piston may fully retract. At full retraction, the resulting imbalance between buoyancy and gravity depends on the particular ballasting of a given float. Thus, variability

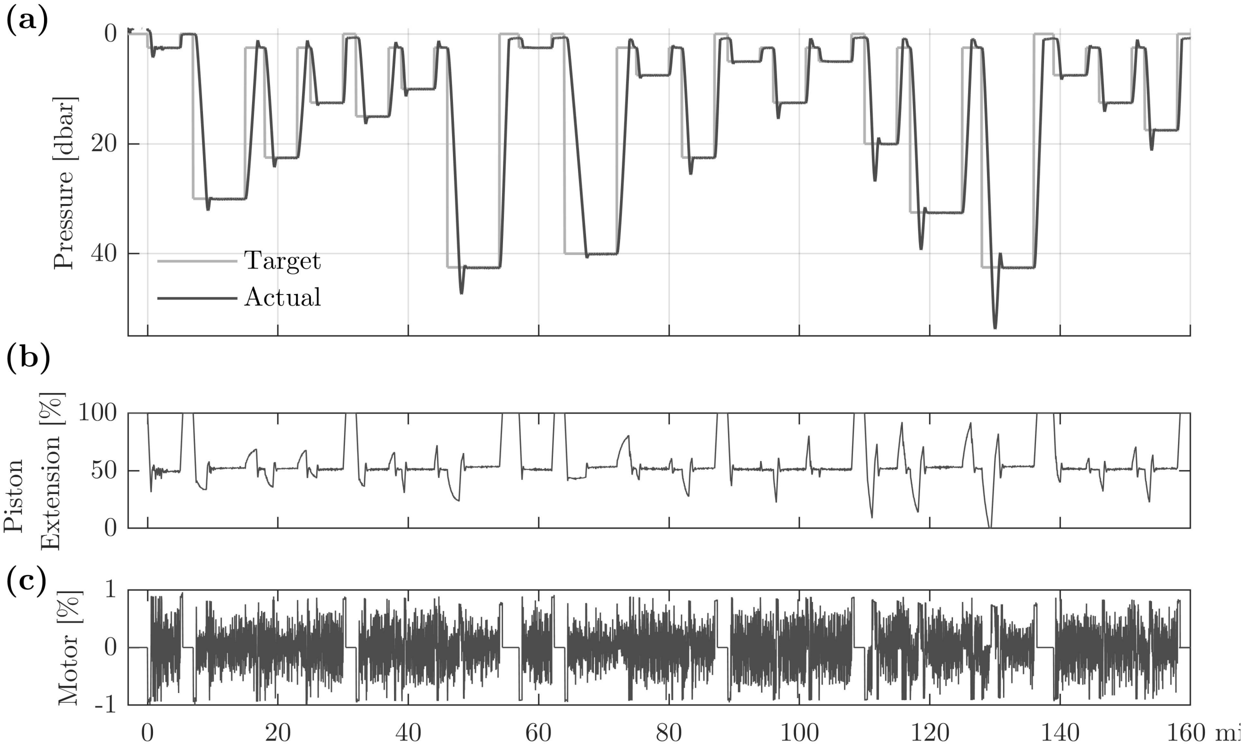

Figure 4.3: (a) Trajectory of μFloat 09 during Lake Washington test, with target depths indicated in light grey and the actual float depth in dark grey, along with piston extension (b) and motor actuation (c) required to control depth.

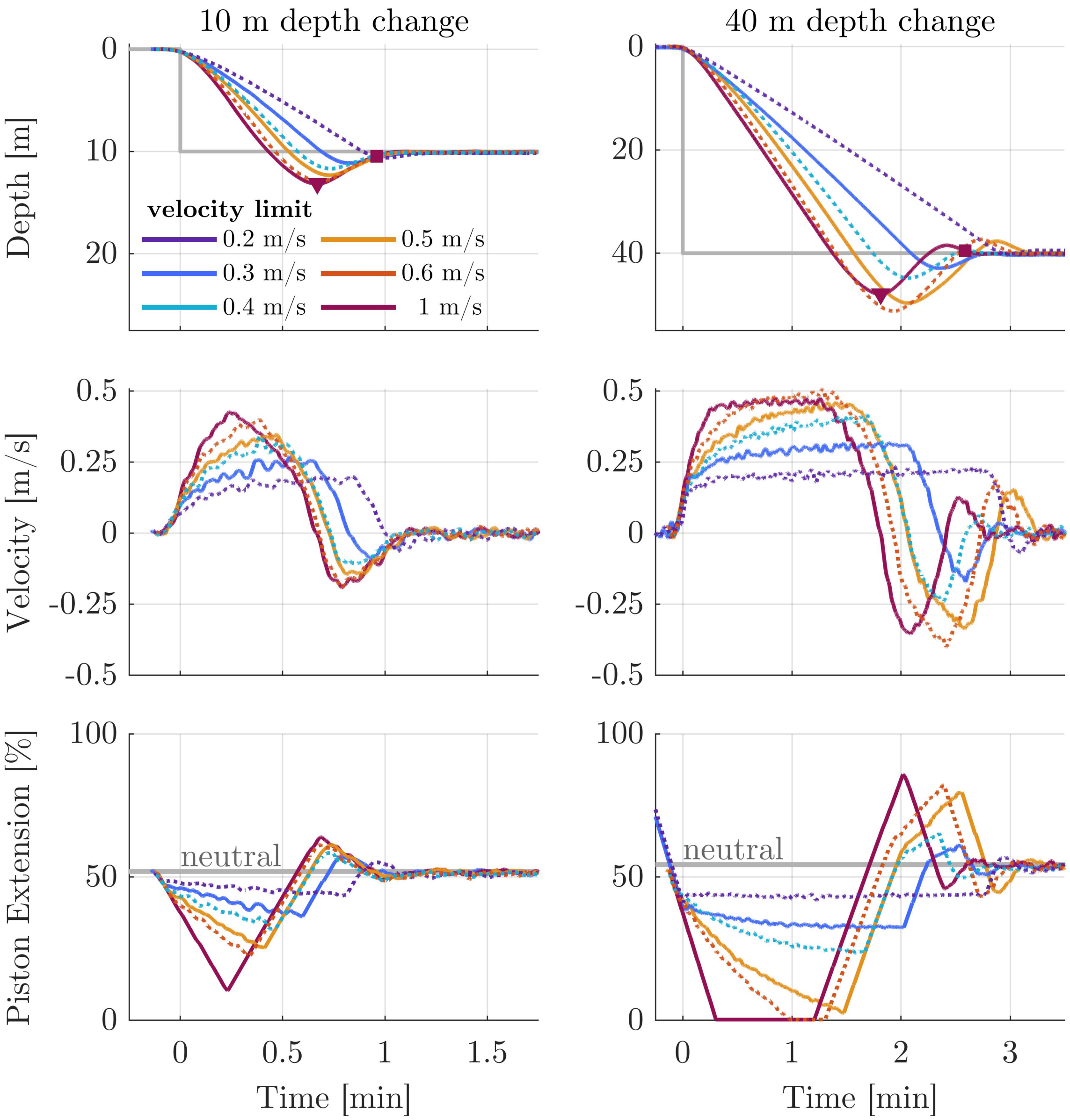

Figure 4.4: Transient response of μFloats 09 (dotted line) and 25 (solid line) performing 10 m (left column) and 40 m (right column) depth changes with varying velocity limits. Depth is plotted relative to the starting depth and time aligned such that rise starts coincide. Peak overshoot (▼) and settling time (■) are annotated for the 1 m/s velocity limit, which effectively represents no control limit on float velocity.

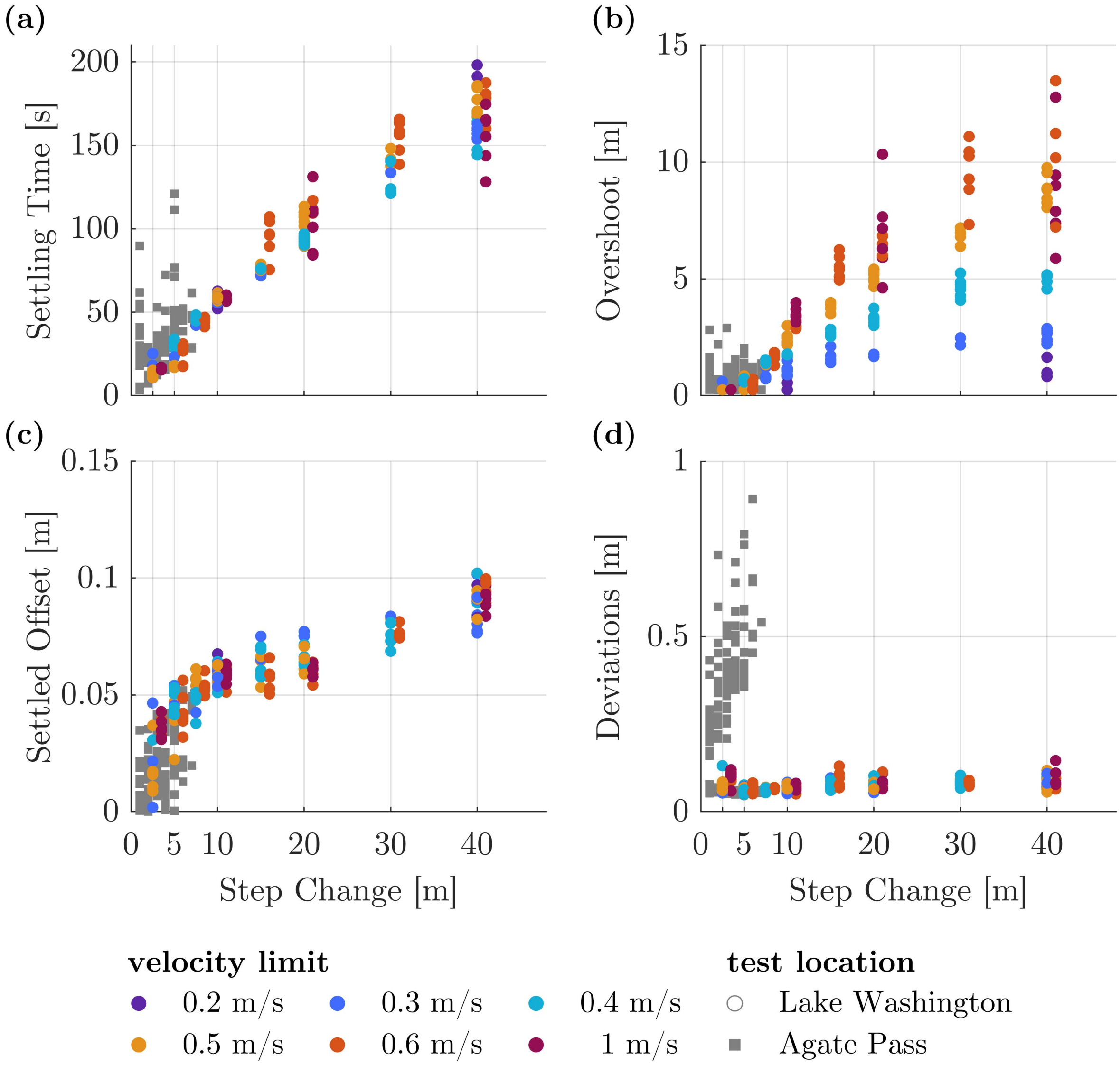

Figure 4.5: Fleet-wide statistics for depth control actions during Lake Washington (circle) and Agate Pass (square) tests. All Agate Pass floats were programmed with a 0.3 m/s velocity limit. 0.5, 0.6, and 1 m/s velocity limit data points from Lake Washington include an offset (1 m) on the horizontal axis to facilitate visualization.

in ballasting produces a range of terminal velocities that are dependent on the direction of motion. For example, a float with a smaller maximum imbalance when diving achieves a lower terminal velocity and, consequently, less overshoot and a shorter settling time. The wider variability in overshoot and settling time can be seen in Figures 4.5a,b for dives > 20 m and velocity limits ≥ 0.5 m/s. Most critically, Figures 4.5a,b reveal that for all depth changes greater than 10 m, a moderate velocity limit (0.3 m/s - 0.4 m/s) significantly improves consistency of the transient response across all floats and reduces overshoot without significantly increasing settling time. For depth changes less than 10 m, float speeds remain low enough such that the velocity limit does not play a significant role in the transient response. In the dynamic environment of Agate Pass, settling time and overshoot increase moderately relative to the quiescent performance, likely due to disturbances from turbulence during depth-seeking periods.

Qualitatively, Figure 4.3 demonstrates excellent steady-state control over all depths in a quiescent environment. Fleet-wide statistics (Fig. 4.5c,d) reveal steady state offset less than 0.1 m across all depths, increasing slightly with depth. This offset is smaller than the absolute accuracy of the pressure sensor ($\pm$ 0.5 m). In the quiescent environment of Lake Washington, deviations, calculated as the interdecile range of variations around the settled depth, (Fig. 4.5d) are < 0.1 m (± 0.05 m) and constant with depth. In the tidal channel, however, deviations around the settled depth increased with higher current speeds: at slack tide, deviation were similar to those in Lake Washington, while those deviations during flood and ebb were considerably larger, most likely due to increased vertical turbulence.

Depth-Holding Disturbance Response

Figure 4.6 demonstrates the float's ability to compensate for slow disturbances, such as those from a modest horizontal density gradient. Depth deviations during the disturbance period (0.13 m) are marginally larger than those during steady state periods before and after (0.08 m). The change in piston neutral buoyancy position equates to a 108 g increase in buoyancy, nearly matching the 106 g wet weight added during the period. Mechanical slip between encoder and linear piston position accounts for the small discrepancy.

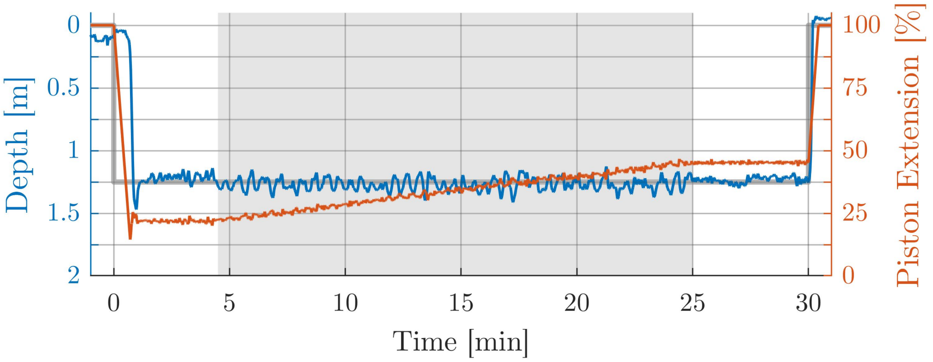

Figure 4.6: μFloat depth and piston extension as a function of time during the slow disturbance response test. Additional mass added to the float from minute 4.5 to 20 (grey region) at a rate of roughly 3.5 grams every 30 seconds, emulating a slow change in site density.

During fast disturbances, such as those expected from a sudden entry into an upwelling region or sharp density gradient, more notable deviations from the target depth occur (Fig. 4.7). Peak deviation scales approximately with upwelling velocity squared, though deviations for stronger upwelling events (> 35 cm/s) may outpace this trend (Fig. 4.7a). Duration of the excursion scales linearly with upwelling amplitude (Fig. 4.7b). While velocity limits from 0.2 m/s to 1 m/s (effectively unlimited) were tested, they were not found to change performance in this disturbance range, as float velocities never exceeded 0.2 m/s in response to the disturbances.

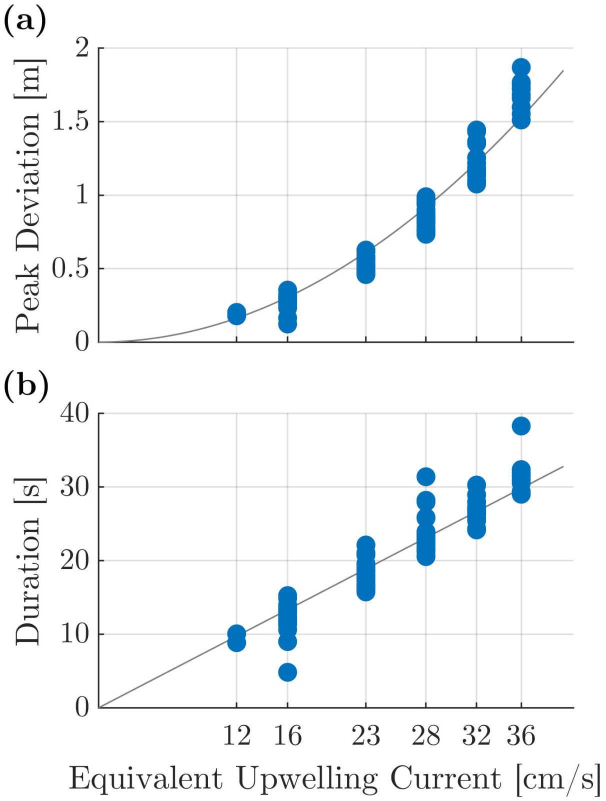

Figure 4.7: Absolute peak deviation (a) and duration of excursion (b) from target depth for depth-holding float subjected to a step change in an external force, expressed in terms of the force produced by an equivalent upwelling or downwelling current. Trendlines are quadratic (a) and linear (b) fits to the data.

4.3.2 Compressibility

Figure 4.8 shows that the floats are significantly more compressible than water, which is consistent with their structural composition. This means that in well-mixed or weakly-stratified waters, the float is isopycnally unstable, and thus requires near-constant actuation to maintain a target depth. If deployed in a stably stratified environment, the density gradient will increase buoyancy with depth, countering losses due to compressibility. Results from Lake Washington indicate that the minimum stratification necessary for isopycnal operation is approximately dρ/dz > [0.0005 kg/m3]/m, or about 0.1 PSU/m salinity gradient. Additionally, we observed a comparatively large decrease in float volume following the first dive, likely associated with regions of trapped air (e.g., near O-rings seals) being initially displaced by water. Likely sources of compressibility are compression of the cylindrical housing shell and any additional trapped air exposed to ambient pressure.

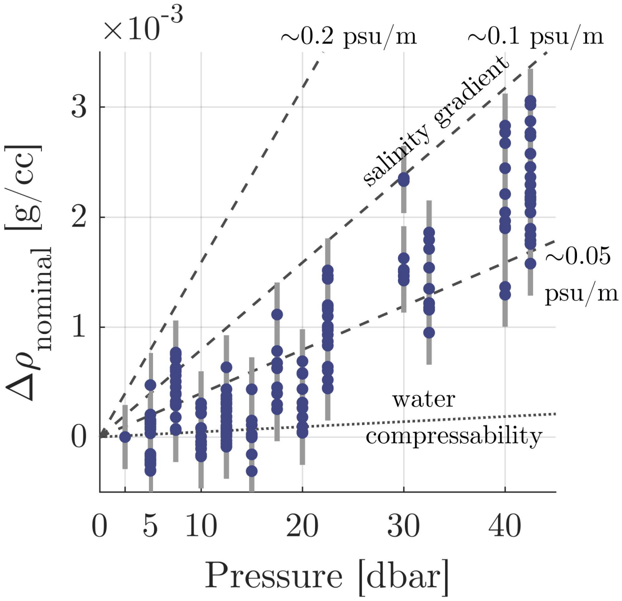

Figure 4.8: Change in nominal float density with pressure due to compressibility. Points indicate an individual measure of float compressibility, with vertical grey bars indicating confidence intervals based on mechanical slop between encoder and linear piston position. Water density changes due to compressibility (for fresh water at 15 °C, dotted line) and vertical salinity gradients (dashed lines) are indicated by dashed lines for references.

4.3.3 Underwater Localization

Nanomodem Connectivity

Figure 4.9 depicts connectivity between μFloat 27 and all surface buoys (a) during a segment of Lake Washington – Test 1. Connectivity is impacted by transmission distance (b), and receiver depth (c), and ambient noise (d,e). Distance (Fig. 4.9b) has the strongest influence on connectivity, with a maximum range of approximately 1 km and consistent connectivity within 400 m observed (e.g., connectivity with SLB-2 drops as drifts away from the float from 19:30 to 20:00). Connectivity is also strongly influenced by source and receiver depth, as expected in stratified environments. The nanomodem transducer on SLB 5 was equipped with a 1 m extension cable, placing it 2.5 m underwater. It exhibited a broadcast range almost twice that of SLB 4 (Fig. 4.9b), which had a transducer at 1.5 m depth. Receiver depth (Fig 4.9c) impacts connectivity more strongly than source depth. Nearly all periods of reduced connectivity between the float and SLBs 1-3 (the closest sources for most of the test) are during shallow dives (e.g., 19:00, 19:08, 19:23, 19:34, 19:50, 19:55, Fig. 4.9c, indicated in red). This is consistent with reduced ping received levels during the same periods (Fig. 4.9d). Finally, all pings must be detectable over the ambient sound level (Fig. 4.9d,e), so elevated sound levels generated by transiting vessels (e.g., 19:10) can inhibit connectivity, though message receptions are observed even at 0 dB signal-to-noise ratio. Additional statistics on connectivity can be found in Appendix D.

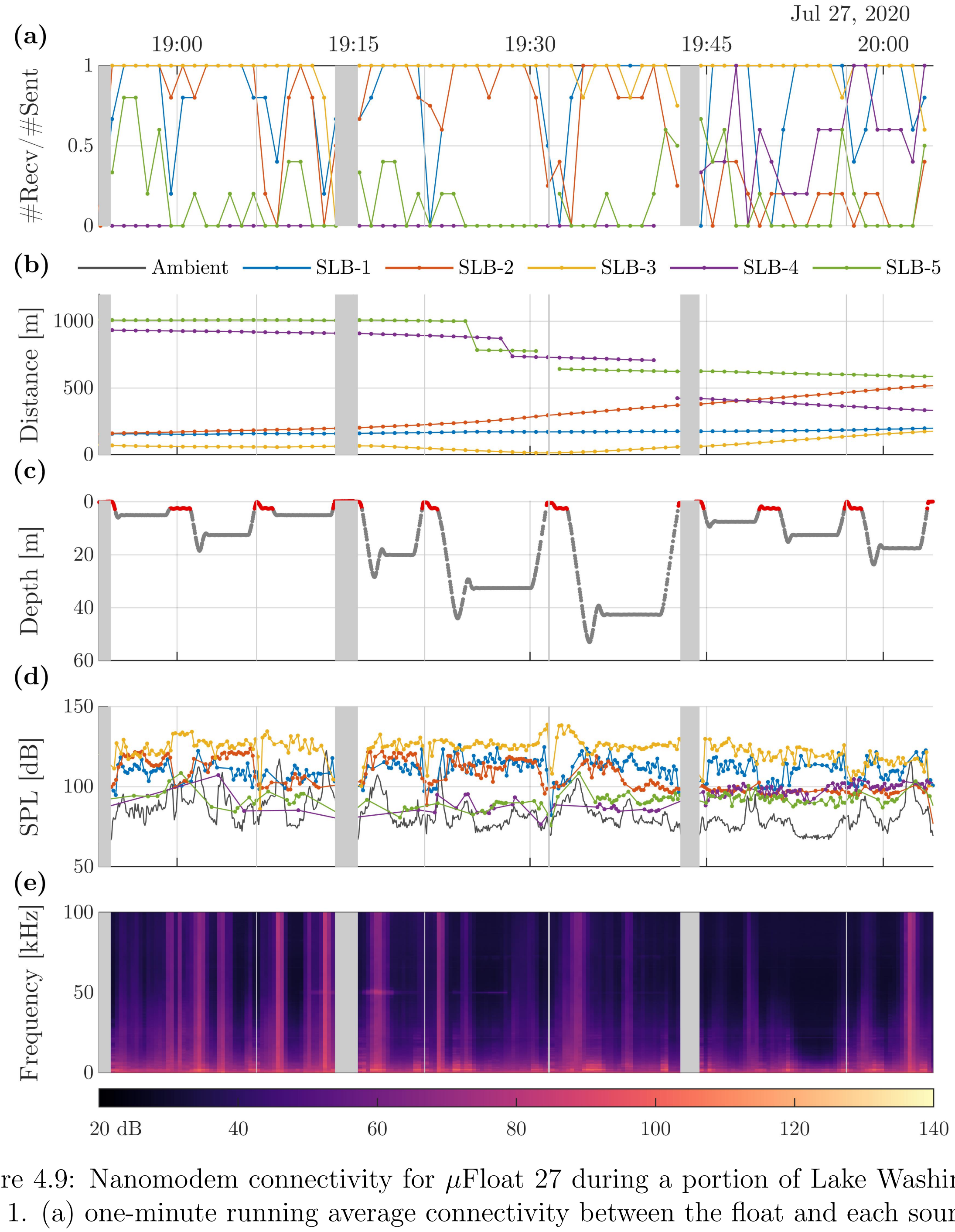

Figure 4.9: Nanomodem connectivity for μFloat 27 during a portion of Lake Washington - Test 1. (a) one-minute running average connectivity between the float and each source; (b) distance between the float and each source; (c) float depth, with dives less than 3 m indicated in red; (d) sound pressure level of received pings and ambient noise in the transmission band (24-28 kHz) (dB re 1 μPa); (e) mean-square pressure spectral density of ambient noise (dB re 1 $\mu\mathrm{Pa}^2$/Hz). Grey regions indicate times when the float was on the surface and receptions were not expected.

Localization Accuracy

Lake Washington tests (Fig. 4.10a) demonstrated acoustic position estimates for the SLBs generally matched the known GPS locations, albeit with considerable uncertainty prior to smoothing. Correcting for bottom-reflections reduced scatter, but did not eliminate it. As shown in Table 4.3, Tests 1 and 2 have similar errors before correcting for reflections, but the corrected localizations for Test 1 are twice as accurate as for Test 2. The likely cause is that Test 1 occurred over the main basin of the lake, where the nominal depth of 60 m was widely applicable. Test 2 (Fig. 4.10a) occurred over a sloped region of the lake, with depth changing 30 m from SLB 4 to SLB 5. Thus the single nominal depth and geometric simplification proved less effective.

Smoothing the data produces physically realistic tracks, though artifacts remain (e.g., offsets from GPS tracks in SLB 2, 3, and 5). To explore the source of localization errors, we considered the case where the acoustically derived distances used in the trilateration were replaced by the actual distances calculated from GPS positions. These estimated positions are almost an exact match to the SLB positions reported by GPS (Table 4.3) in Lake Washington, which suggests that the errors in acoustic-based trilateration are a consequence of uncertainty in time of flight and sound speed due to stratification rather than malformed array configurations. We note that SLB to SLB connectivity was significantly lower than SLB to μFloat connectivity when floats were deeper than 5 m, with 57% of distance estimates requiring a reflection correction. Consequently, these results may be an upper-bound on μFloat localization errors. Positioning uncertainty on the two grounded floats during Test 2 was only ±1.5 m, computed as the interdecile range of distance between the given position and the median position while grounded. No received pings were suspected of containing a reflected path. This uncertainty is similar in magnitude to GPS-trilateration accuracy and smaller than the accuracy of individual GPS receivers (± 2.5 m).

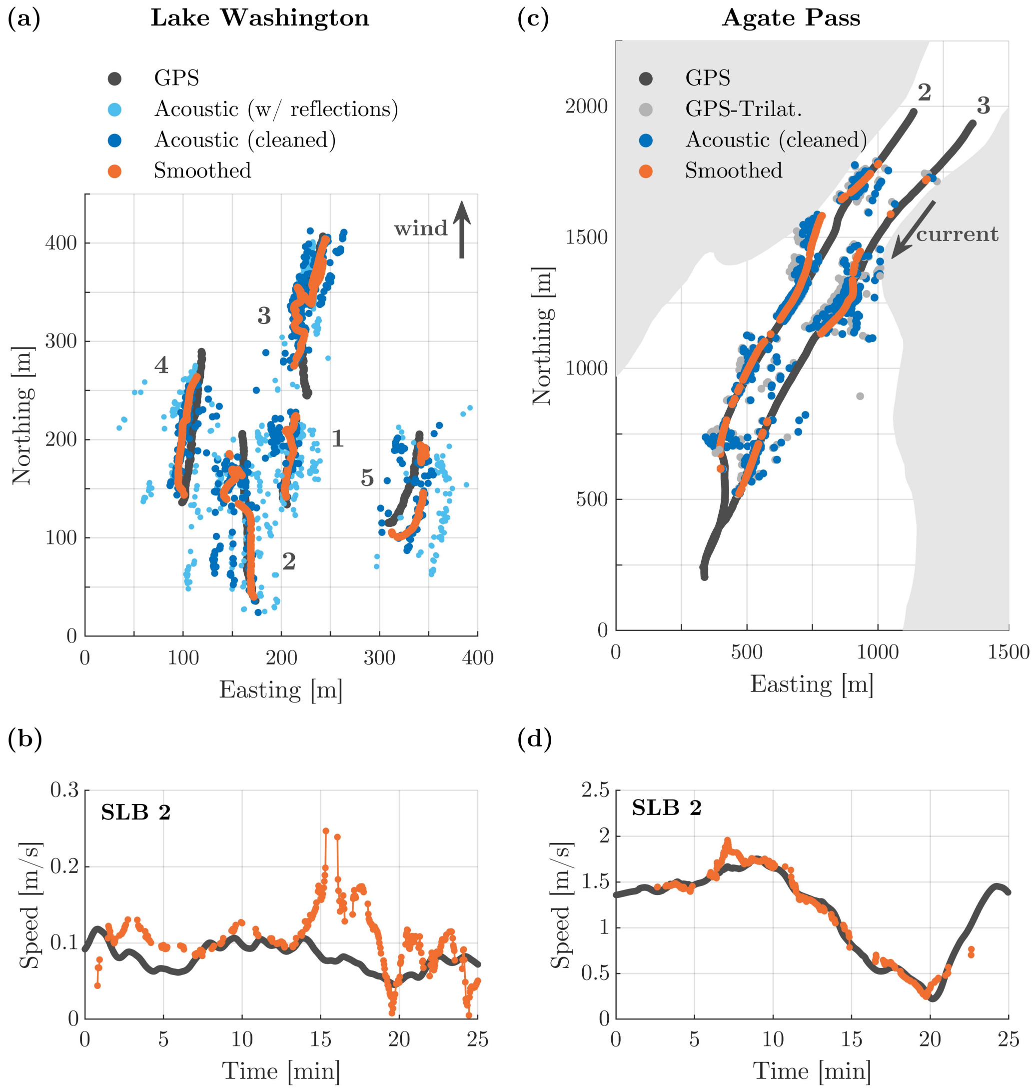

Figure 4.10: Localization system accuracy during Lake Washington - Test 2 (a,b) and Agate Pass (c,d). (a) and (c) compare acoustic localizations of SLBs relative to their known GPS positions. In Lake Washington, positions based on trilateration using GPS-estimated distances are indistinguishable from the true GPS track and omitted. No acoustic reflections were apparent in the Agate Pass data. SLBs are designated by number, with tracks from Agate Pass limited to SLB 2 and SLB 3 for clarity. (b) and (d) show velocity estimated from the smoothed acoustic position data (only at locations with valid position data) as compared to the 'true' velocity computed from the GPS tracks.

Table 4.3: Percentiles of position error (relative to 'true' GPS positions) and velocity error (relative to 'true' velocity computed from GPS positions) for SLBs in Lake Washington and Agate Pass. Nominal water velocities for each case are provided for context.

	Lake Washington - Test 1			Lake Washington - Test 2			Agate Pass		
Position (m)	50th	75th	90th	50th	75th	90th	50th	75th	90th
GPS-trilat.	0.4	0.7	1.5	0.3	0.6	1.1	12.4	35.5	76.7
Acoustic (w/ref.)	13.4	21.3	42.5	14.2	27.9	47.0	*N/A*		
Acoustic	4.1	5.2	10.5	10.4	18.5	26.5	12.2	37.1	79.2
Smoothed	4.0	4.6	7.2	8.0	12.1	17.0	5.0	15.5	30.4
Velocity (m/s)	Nominal: 0.04 ± 0.03 m/s			Nominal: 0.07 ± 0.03 m/s			Nominal: 1.4 ± 0.7 m/s		
Acoustic	0.08	0.23	0.78	0.14	0.98	3.9	4.4	17.2	53.7
Smoothed	0.008	0.013	0.019	0.020	0.033	0.046	0.035	0.063	0.117

Velocities computed from the smoothed acoustic position data are generally agree with those computed from GPS-positions (Fig. 4.10b). Errors in velocity computed from instantaneous GPS-based trilaterations and corrected acoustic data are greater than the nominal water velocity (Table 4.3) and omitted accordingly. Velocities calculated from acoustic localizations of SLBs were found to be within 0.04 m/s, which is expected to be an upper limit on float accuracy due to the poorer acoustic connectivity experienced between SLBs.

For the test in Agate Pass, accuracy of the unsmoothed acoustic localizations was inferior that achieved in Lake Washington, however the source of error was different (Table 4.3). Position errors based on trilaterated GPS-distances are effectively equivalent to acoustic errors, suggesting poor SLB array configurations, a consequence of their freely-drifting and converging paths. Fortunately, smoothing appears to significantly improve both the position and velocity estimates, with 90^{th} percentile velocity errors less than 10% of the nominal flow speed.

4.4 Discussion

4.4.1 System Performance

μFloat Dynamics

The μFloats achieved depth control within 0.1 m of target depth in quiescent flow and 0.5 m in fast-moving flows. While maintaining depth, deviations from target depth due to slow disturbances (e.g. float experiencing changes in local water density) were nearly indistinguishable from undisturbed operations. Stronger disturbances do produce noticeable deviations, though even for the moderate upwelling speeds (0.35 m/s) emulated in the salt water tank, the float remains within 2 m of the target depth and returns to the target depth within about 30 seconds. For events stronger than those tested here, the velocity control limit and terminal velocity of the float will likely slow corrective actions. While not a rigorous analysis, the relation between peak deviation and disturbance magnitude offers insight into vertical deviations observed during Agate Pass (Fig. 4.5d). The deviations were predominantly 0.25-0.5 m, suggesting vertical velocities around 0.1-0.2 m/s, or about 10% of the mean horizontal velocities, which is plausible for vertical turbulence in a tidal channel [151].

When operating in environments where the float transient response is important, limiting the maximum float velocity through the control scheme is effective at preventing undesirable overshoot and increasing the consistency of settling time across floats. For deployments less than 10 m, performance is independent of the velocity limit, as the float speed inherently remains below 0.2 m/s (the lowest limit tested) under the current control scheme.

While not presented here, depth control as shallow as 0.5 m has been achieved in pre-deployment quality control tests in a 2 m depth tank. In practice, continual disturbances due to wave motion may complicate such shallow deployments. Additionally, acoustic connectivity may be degraded near the water surface, as was observed in Lake Washington tests.

The deployments included a number of floats with external sensors with the largest external sensor being the hydrophone (~7% float nominal volume). While these floats were re-ballasted prior to deployment to accommodate the additional sensor weight, no custom control tuning was performed. Nonetheless, the dynamics (both transient and steady-state) of these floats were nearly indistinguishable from floats without ancillary sensors. This demonstrates the adaptability of the μFloats to accommodate external payloads. In theory, the buoyancy engine can tolerate a 3x increase in nominal float volume before losing the ability to accommodate a change in density from fresh to salt water, though we expect changes in nominal volume >20% would likely require re-tuning the control scheme due to the decrease in relative actuation for a given absolute change in piston position.

Localization

The results presented here demonstrate that the nanomodem is a robust, accurate, and economic localization solution. However, the composite system does face several drawbacks. First, the nanomodem version (v2) implemented on the prototype μFloats cannot receive messages simultaneously, necessitating strict scheduling with gaps for anticipated transmission time. In earlier Lake Washington tests (not discussed here), we observed pings from sources 200 m distant that were received 3 seconds later in the hydrophone record and hypothesized to be echoes off the steep walls of the glacially-carved lake. Thus, receipt of these echoes occasionally blocked scheduled transmissions from the SLBs and receptions of direct transmissions on the μFloats. Consequently, the update rate for position estimates in Lake Washington was 4 seconds (3 receptions, each delayed by 2 seconds). In Agate Pass, reflections were not a concern in the shallow channel, and thus permitted a 1-second ping interval, resulting in 2-second update rate. Technically, the position estimate update rate places a lower limit on the time/length scale of observable fluctuations in horizontal float velocity. In practice, the variable nature of the acoustic channel results in noisy and gappy data, requiring smoothing to produce physically realistic float trajectories, with the time window used in the smoothing operation limiting the resolved motions. However, combining acoustic measurements with short periods of dead reckoning from IMU data [16] could theoretically decrease that limit down to the physical responsiveness set by the float size [30, 27].

Acoustic position estimates may be degraded by five sources of error:

1. *Error in SLB GPS locations:* Surface buoy GPS error is minimized via the low-pass filter and is negligible relative to the other error sources.

2. *Poor SLB array geometry relative to receiving device:* SLB array geometry can negatively impact trilateration, as seen in Agate Pass. Remedies include increasing the number of SLBs, adding moored SLBs, adapting initial deployment positions based on experience gained in repeated deployments, active on-the-fly manipulation, or utilization of actuated reference devices, such as autonomous surface vehicles equipped with nanomodems. Additionally, alternative localization schemes, such as those implementing Bayesian methods [118, 17, 154] could improve results without hardware interventions.

3. *Sound speed measurement error and/or site variation:* Sound speed variation and ambient noise in the acoustic channel is a fundamental challenge, due to the variety of oceanographic conditions exhibited in coastal water, as well as the prevalence of human activity. With regards ambient noise, the nanomodems are relatively sensitive, with receptions possible at nearly 0 dB SNR. But sound speed gradients, such as those observed in Lake Washington, will always impact localization performance, and the specific degradation and any corresponding corrections must be addressed on a case-by-case basis.

4. *Clock drift between μFloats and surface buoys:* The maximum clock drift expected between floats and SLBs is approximately 0.1 seconds per hour, which in an environment with 1500 m/s nominal sound speed, would result in maximum path length errors of 150 m. The accuracy achieved during Lake Washington and Agate Pass deployments suggests that clock drift was not a significant source of error, relative to sound speed

gradients and array geometry. Additionally, if drift is found to be problematic in certain conditions (e.g., extreme temperatures), occasional surfacing to re-synchronize the μFloats with GPS PPS should mitigate this error.

5. *SLB and μFloat movement within localization time periods:* As both μFloats and SLBs are freely drifting, in fast currents such as those experienced in Agate Pass, they may move within the time period necessary to transmit and receive the three pings necessary for localization. Given the 1-second ping interval and 2 m/s maximum currents, this amounts to 6 m of ambiguity in float position. While it may be possible to account for these movements using an iterative post-processing method, the error was sufficiently small relative to the sound speed and array geometry errors to not warrant correction.

Because the nanomodems are capable of bidirectional communications, the inverse architecture (with μFloats transmitting and DAISYs receiving) is also possible and would allow real-time monitoring of float positions. However, for a swarm of more than a few μFloats, the requirement for the v2 nanomodems to schedule non-overlapping pings would severely reduce the position update rate for each float. Additionally, the nanomodems permit transmission of small data packets, which could enable sharing of environmental information, real-time coordination of float activity, and float awareness of position (i.e., underwater GPS architecture). While an area of active research for more mobile AUVs, such adaptive sampling has not yet been demonstrated for buoyancy-actuated float swarms. All of these capabilities will benefit from improvements to nanomodem hardware. The new generation (v3) features binary-phased-shift-keyed signals with a 10-fold increase in data rate, shorter and overlapping ping receptions, and improved error handling. Pings are shorter, allowing faster repeat rates and correspondingly improved position update rates.

Operations

Operation of the μFloat system proved straightforward. The μFloats are lightweight and robust enough to permit an individual to rapidly deploy them from small vessels. The surface buoys are larger but still easy to handle by an individual, and can either drift or be moored. Float recovery was sometimes challenging due to the small form factor. The radio and cellular relay of GPS locations proved essential to guide recovery vessels within visual distance, at which point retrieval with a boat hook was simple. Glare, wave action, and fog complicated float sighting and recovery. With the only vessel requirement being sufficient deck space to fit equipment and a minimal personnel (captain and up to two crew members), operations were relatively inexpensive. For the Agate Pass test, the repeat rate (i.e., interval between recovery and redeployment) ranged from 40-80 minutes and could be reduced further with operational practice or multiple recovery vessels.

Endurance of the μFloats is constrained by both the hotel load and the buoyancy engine. While one advantage of buoyancy controlled floats in open ocean applications is their energy efficiency, the μFloat system was designed for short-term deployments ($<$ 1 day) and prioritized cost-effectiveness and adaptability over energy efficiency. As such, the hotel load is approximately 4 W. When both depth-seeking and depth-holding, the buoyancy engine motor runs nearly continuously. Due to low drivetrain efficiency, consumption varies only slightly with depth, with average buoyancy engine loads ranging between 3 and 4 W. This results in practical deployment lengths of about 12 hours. Additional details are located in Appendix E.1. Improving endurance could be achieved by redesigning the electronics suite around a lower power microcontroller, reducing buoyancy engine actuation time, and improving drivetrain efficiency.

4.4.2 Comparison to Other Floats

Through benchmarking activities, we have demonstrated several advantages of the μFloat over other floats. The most notable of these is cost: at \$2.4k per float and \$3k per surface buoy, a swarm of 20 floats and 5 localization buoys costs ∼\$65k. Only the M-AUEs are comparable at \$6k per float but their smaller form factor reduces buoyancy actuation and the ability to host auxiliary sensors. Our cost reduction is a consequence of using inexpensive, commercial-off-the-shelf components and sensors and a minimal standard sensor suite. The second advantage offered is the μFloat's comparatively large buoyancy engine (9% actuation), which provides capacity for external sensors, even in areas with sharp density gradients. A recently developed high-capacity float (Gene Massion, pers. comm.) is similar at 8% actuation, but is equipped with a full suite of coastal oceanography instruments, making it significantly more expensive, larger (2 m, 5x), and heavier (100 kg, 25x) than the μFloat, thus requiring an A-frame for deployment. The commercially produced ALAMO float (4.2% actuation) can similarly traverse strong density gradients, but are significantly more expensive (>$20k). The third advantage of the μFloat system is the nanomodem-based acoustic localization, which can provide position accuracy similar to GPS, as well as the ability to send commands and data between floats and the surface. While the M-AUE localization provides similar accuracy (± 1.2 m) and longer range (<5 km), the system is restricted to one-directional localization [71] and cannot be used for general-purpose communication. Roman et al. utilizes ultra-short baseline localization that has lower accuracy (± 15 m) and shorter range (250-1000 m), but supports higher bandwidth communications (14 kbit/s). Casagrande et al. [17] has recently investigated enhancements to these floats via terrain-based particle filter with visual odometry to improve positioning accuracy. The RAFOS localization system, installed in ocean basins and implemented on ARGO and MLF floats, does not support general-purpose communication and while its 1400 km range is impressive, the coarse 1 km accuracy is ill-matched for coastal-scale research. As such, the nanomodem array provides a compelling balance of range, accuracy, flexibility, and cost for distributed sensor platforms in coastal environments and new generations of the hardware promise higher bandwidth and shorter message durations, improving connectivity and accuracy. In addition, we have achieved the highest depth-holding accuracy reported for a buoyancy controlled float, matching that of Roman's hybrid propulsion approach [139], albeit with slower dynamics.

The μFloat system does have several limitations. First, relative to other floats, the standard sensor suite (pressure, temperature, and IMU) is minimal. At a similar cost, the M-AUE includes a satellite modem for data transfer and recovery beyond the range of cellular networks, as well as a hydrophone for acoustic monitoring, though motor noise causes significant contamination when changing or holding depth [71](Paul Roberts, pers. comm.). The larger floats (ALAMO, D'Asaro, Roman) can support a suite of additional sensors, including salinity, pH, dissolved oxygen, acoustic Doppler velocimeters, altitude sensors, and optical cameras. The carrying capacity of the μFloats mitigates the sparse standard suite, as the float can be equipped with additional sensors on an as-needed basis. As many sensors of interest (e.g., dissolved oxygen, pH) are more expensive than the μFloat itself, cost will primarily scale with the number of auxiliary sensors, and can be adjusted to the needs and budget of the end user. The second primary limitation is endurance. The μFloats are designed for short-duration (< 1 day) deployments and constrained by the consumer-grade single-board-computer and inefficient buoyancy engine. The M-AUEs and Roman floats have similar endurance to the μFloat, but the ALAMO and D'Asaro floats are better suited for studying long-duration phenomena. Third, only depth control has been robustly demonstrated for the μFloat. Profiling (the primary Argo mode) and Lagrangian/isopycnal control (implemented by D'Asaro) are also scientifically relevant and desirable. Additional control modes include bottom-tracking, as implemented on the Roman float for visual surveys of biological communities [121, 139], and intermittent bottom-stationing, which was first demonstrated by Langebrake et al. [79] with an Argo-style float. Finally, true Lagrangian behavior is optimized by reducing float size, and in this respect, the M-AUEs are superior.

Chapter 5

CROSS-PLATFORM EVALUATION IN AGATE PASS, WA

This chapter describes the the first application of the μFloat swarm towards small-scale (< 1 km), high resolution (< 5 m) measurements characterizing mean currents in energetic tidal channels, which took place in Agate Pass, WA in August 2020. While some results from this test were presented in Chapter 4 in the context of buoyancy engine and localization performance, the objective of this chapter is to demonstrate how, when considered in aggregate, the μFloat swarm provides a unique ability to characterize horizontal and vertical gradients of water currents while simultaneously measuring *in situ* properties like temperature. These measurements are validated against data products from ADCPs and a CTD.

5.1 Introduction

Tidal currents play a central role in our coastal waters, impacting water quality [34, 33], larval transport [95], algae blooms [88], marine navigation [22][21], and energy production [11, 116]. Because they are driven by astronomical forcing, tides are predictable on a decadal time scale. However, the resulting water movements are less predictable [54]. Local bathymetry can produce currents exceeding 4 m/s, strong horizontal and vertical heterogeneity, and significant variability over a matter of minutes [98]. Waterway management, ecosystem health monitoring, and improved scientific understanding all benefit from accurate characterization of local currents on horizontal spatial scales O(0.1-10) km, vertical scales O(0.1-100) m, and time evolution from O(minutes to months).

Since their introduction in the early 1980s, acoustic Doppler current profilers (ADCPs) have become the standard instrument for measuring water velocity [35]. To produce estimates of 3D velocity at discrete distances from the instrument head, the ADCP emits a ping from four (or five) diverging transducers and measures the Doppler shift on echoes returned from scattering sources in the water (e.g., particulate, bubbles) [149]. A flexible instrument, they can be deployed on stationary platforms such as bottom-landers [61] or moored buoys [97], or on mobile platforms such as autonomous underwater vehicles [5, 13, 103, 159], vessels [51, 165], or drifting surface-buoys [59, 134]. Stationary deployments provide long-duration O(days to months) time-series essential for extracting tidal harmonic constituents at a given site [74, 116, 45]. However, the spatial coverage of such data is correspondingly limited. While time-limited O(hours to days), mobile deployments can map horizontal variations in water velocity [51]. Platform motion (e.g., translation velocity, heave) has largely been addressed by commercial systems through bottom tracking and/or integration with GPS and inertial measurement units that correct for motion [161, 66, 104, 44]. Similarly, Doppler noise can reduce accuracy, but is addressed by averaging multiple independent samples [89, 149]. For stationary platforms, this is an effective measure, but for mobile platforms, such averaging convolves spatial and temporal variability. Thus, there is a direct trade-off between spatial coverage and accuracy.

Underwater floats have a long history in oceanography [57]. The Argo program, with nearly 4000 floats distributed worldwide, and over a million profiles taken over the 20 year program history, has provided incomparable data on ocean state variables (salinity, pressure, and temperature), as well as unprecedented resolution of ocean circulation patterns [73]. Given the demonstrated success for basin-scale problems, there is growing interest in extending this distributed sensing paradigm to smaller scale, coastal processes. As such, a number of new buoyancy-controlled floats have recently been developed for coastal environments that can operate in stronger density gradients, shallow and variable bathymetry, and faster currents [71, 99, 121]. For example, Jaffe et al. deployed a swarm to measure larval dispersion resulting from interactions with internal waves [71] and Roman et al. developed a system with increased actuation and bottom-tracking ability for coastal bathymetric surveys [99, 121]. As discussed in Chapter 2, virtual experiments comparing float swarms and mobile ADCP surveys suggest that float swarms may provide similar accuracy estimates of three-dimensional current fields while simultaneously gathering *in situ* water property data (e.g., temperature). The μFloats were developed specifically to investigate this observational paradigm in practice.

This chapter presents an experimental comparison of three-dimensional measurements of water velocity produced by a μFloat swarm (~20 floats) to four drifting, downward-looking ADCPs and a station-keeping, vessel-mounted ADCP. Section 5.2 describes the test site, equipment, and data processing methods. Section 5.3 presents the observed site characteristics and comparisons across platforms, and implications from the outcomes are discussed in Section 5.4.

5.2 Methods

5.2.1 Site Description

Agate Pass, WA (Fig. 5.1a,b) is a tidal channel in Puget Sound, WA, bordered on the south by Bainbridge Island and on the north by the Kitsap Peninsula. The channel connects Port Madison, a bay (40-60 m deep) that is part of the main basin of Puget Sound, to Port Orchard, a shallower strait (20-30 m deep) separating Bainbridge Island from the Kitsap Peninsula. Tides in the region are mixed semi-diurnal, with water level ranges reaching 4 m in Port Madison. At its narrowest point, Agate Pass is only 300 m wide and 9 m deep, which generates currents exceeding 2 m/s during periods of peak exchange. As a result of these high flow speeds, the site is of interest tidal energy development, which motivated its selection for this study.

5.2.2 Instruments

Vessel-Mounted ADCP

Fig. 5.2a depicts the RDI Workhorse Mariner (1200 kHz) four-beam ADCP mounted on a davit for deployment. Five-minute station-keeping surveys at three locations (Fig. 5.1(b), SK1-3) were repeated during each deployment period. During these surveys, the vessel oper-

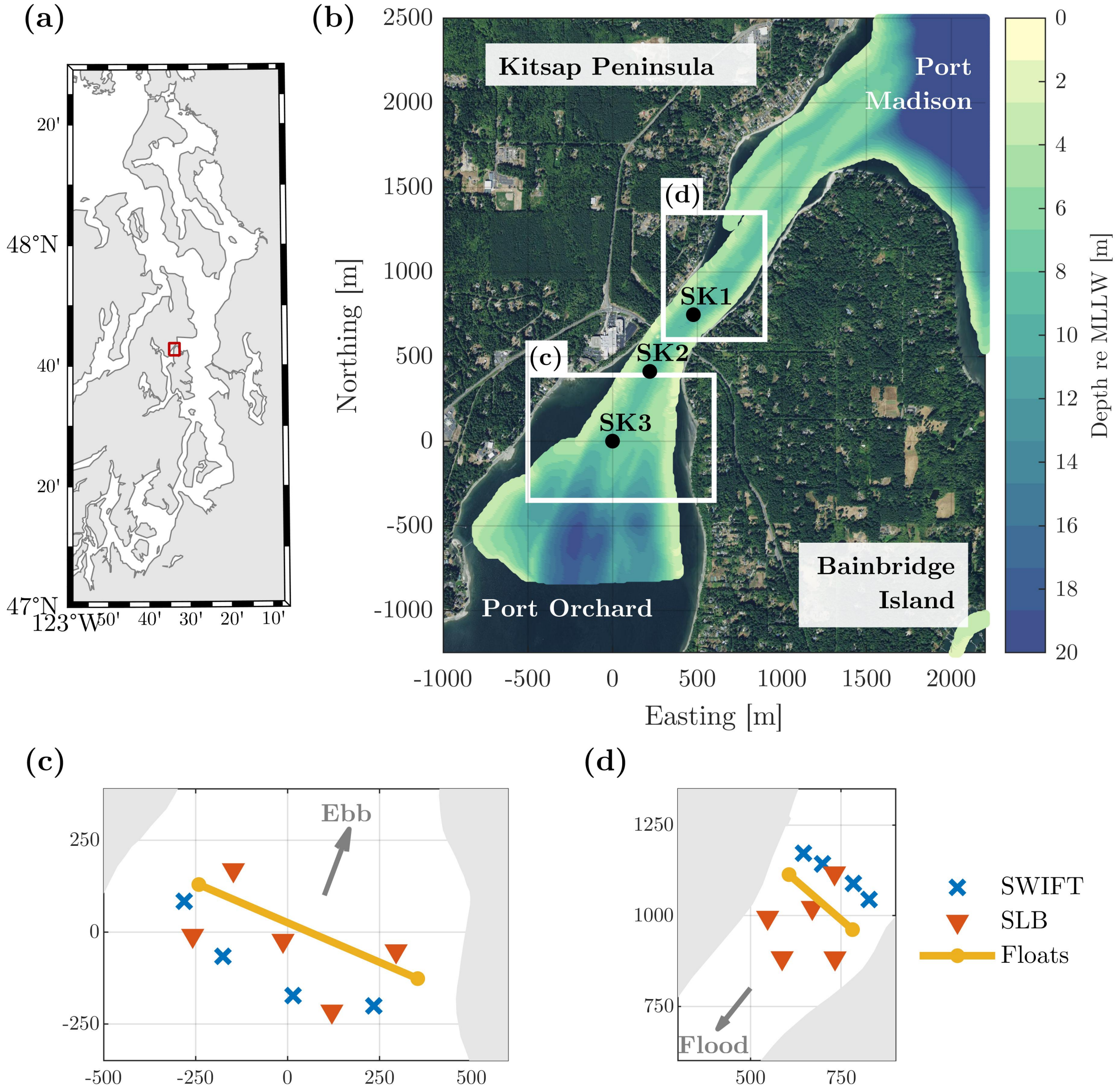

Figure 5.1: Map of Puget Sound (a) and Agate Pass, WA (b). Station-keeping (SK) locations are indicated in (b) and remained the same during ebb and flood. (c) and (d) depict initial drifting instrument positions during ebb and flood, respectively, with ~20 μFloats deployed at regular intervals along the indicated line.

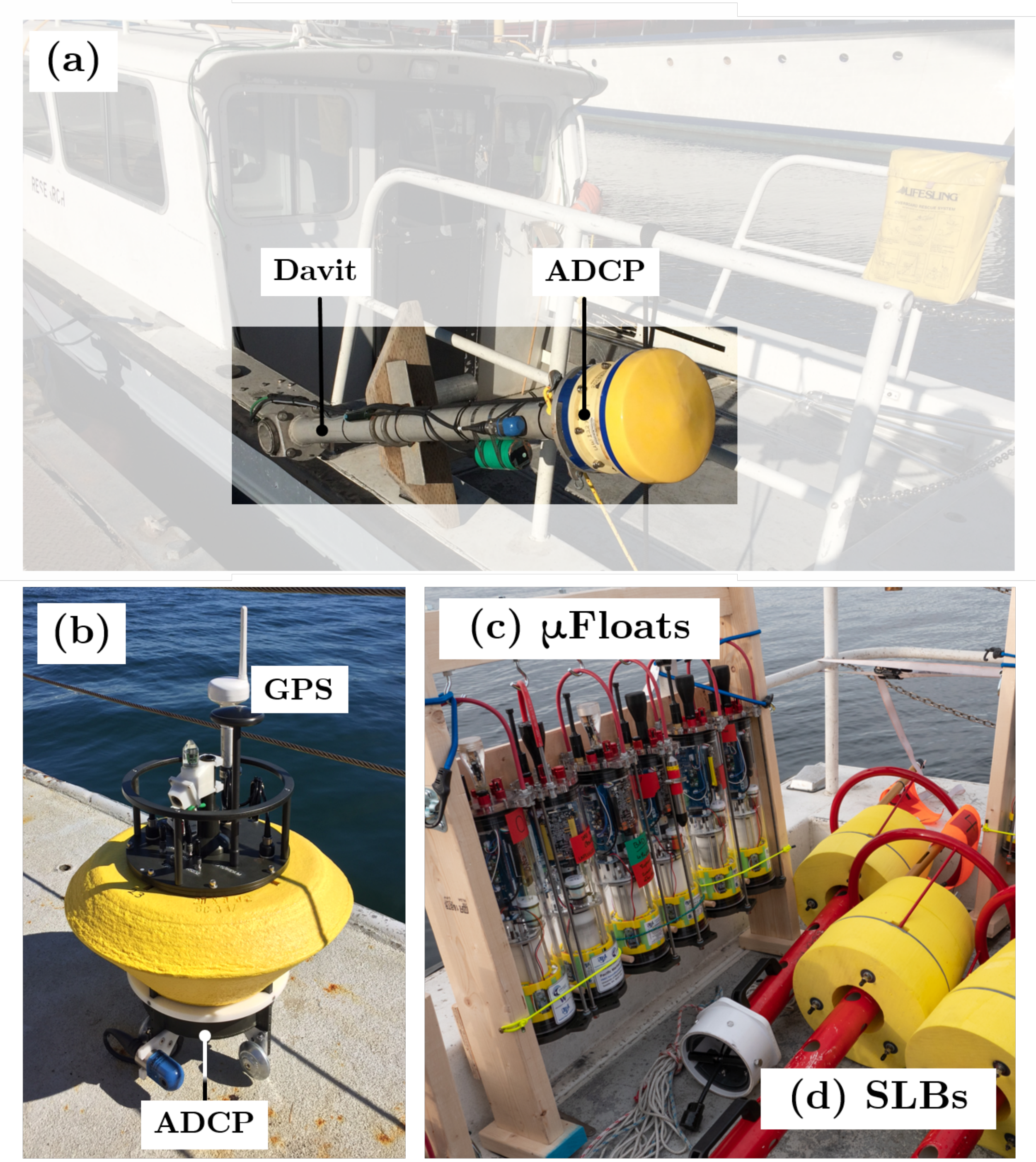

Figure 5.2: Primary instruments used in this survey: a vessel-mounted ADCP (a), four SWIFTs (b), twenty μFloats (c), five surface localization buoys (SLBs) (d).

ator held station to within 50 m of the target location. To compensate for residual motion, the RDI VMDAS software integrated bottom track velocities from the ADCP to convert the measurements from a moving to a fixed reference frame. Ancillary GPS data recorded in VMDAS were integrated to provide positions and timestamps for the measurements. The raw ADCP data were sampled at 2 Hz and then screened to retain broadband Doppler correlations above 50%. The velocity profiles were trimmed to remove spurious values below the seafloor based on bottom-tracking depth. The remaining data were assembled into five-minute ensemble averages at each of the three stations during each survey cycle. Station-keeping provided sufficient samples to reduce Doppler noise in the ensemble averages, while allowing moderate horizontal coverage [114]. Here, the ensemble velocity uncertainty was 0.012 m/s.

SWIFTs

The SWIFT (Fig. 5.2b) is a drifting surface buoy equipped with a downward-facing Nortek Signature1000 five-beam ADCP, Sutron Xpert data logger and processing board, and SBG Ellipse GPS and inertial navigation system (INS) developed by Thomson et al. [155, 154]. An Airmar WX200 provides supplementary wind speed and direction. The ADCP collected 1 Hz data in broadband mode during 512 s bursts. These repeated every 720 s (i.e., 5 bursts per hour), with the intermediary period used for onboard processing of the ADCP data. The ADCP was configured to collect data in 40 depth bins with a resolution of 0.5 m, with a 0.35 m blanking distance, with a corresponding max range of about 20 m. In post-processing, the drift velocity of the buoy was added to the observed profiles to estimate the true velocity profile in a fixed reference frame. As for the vessel-mounted ADCP, the velocity profiles were trimmed to remove values beyond the seafloor using an altimeter return from the center beam. Then, 30-second ensemble averages of the drift-corrected profiles were calculated, resulting in effective uncertainty of 0.005 m/s [60]. We note that for the highest drift speed of 2 m/s, the ensembles effectively average over 60 m of along-track positions.

μFloats and Surface Localization Buoys

As presented in Chapter 3, the μFloat (Fig. 5.2c) is a prototype underwater float developed specifically for coastal environments. Equipped with a solid-piston buoyancy engine, the float can change its density by 9%, providing vertical actuation speeds of $\pm$ 0.4 m/s and depth-holding accuracy within $\pm$20 cm in quiescent water. Primary sensors include pressure (used for depth control), temperature, and inertial measurement unit. The large buoyancy engine capacity allows for the addition of external sensors without re-ballasting. When on the surface, the μFloats broadcast their GPS location via cellular and radio signals to facilitate recovery.

An array of five GPS-tracked surface localization buoys (SLBs) are deployed concurrently to track the μFloats while underwater (Fig. 5.2d). SLBs and μFloats are equipped with small acoustic ‘nanomodems’ [43, 106]. The surface buoys broadcast uniquely coded pings on a round-robin schedule. All nanomodems within range record and timestamp these pings. In post-processing, sent and received pings are aligned and time-of-flight is calculated from the associated time stamps. Distances between each source and receiver are then estimated based on sound speed. Sets of three or more pings from unique surface buoys are used to trilaterate float position [111]. Position data are smoothed by a robust moving local regression with a moving window size between 60 and 240 seconds, adjusted for each float depending on ping connectivity rates to ensure decent regression statistics. Velocity is estimated by a first-order central-difference of smoothed position data. Resulting position and velocity uncertainty is $\pm$ 15 m and $\pm$ 0.06 m/s respectively. Additional details on the localization process are presented in Chapter 3 and Appendix C. To provide an apples-to-apples comparison with SWIFT data, we subsequently apply the same 30-second ensemble averaging procedure to the float and SLB tracks, reducing position and velocity uncertainty to $\sim$ 3 m and $\sim$ 0.01 m/s.

During each survey cycle, between 18 and 20 floats were deployed. Two floats were lost during the experiment, with one subsequently recovered. For a given deployment, all floats were programmed to either hold constant depth or repeatedly profile between the surface and a target depths. Constant depth deployments were intended to provide consistent observational distributions. Profiling deployments were used to ensure along-track localizations by ‘bread-crumbing’ GPS data in case of poor acoustic connectivity, with the awareness that such a method may smear horizontal velocity measurements vertically through the water column. As the μFloats are prototype instruments, some float data ($< 10\%$) was corrupted by mechanical or electrical malfunctions, as well as human programming errors. These data were discarded. Similarly, data were discarded from any periods in which the floats were suspected to be in contact with the seabed. Consequently, analytical results from each survey cycle consisted of data from 14-18 floats, with the exact number indicated where relevant.

Water Properties

A hand-deployed Xylem CastAway CTD was used to profile temperature and salinity and, from these quantities, calculate density and sound speed. One profile was collected during each survey cycle, though position ranged between SK3 and SK2, depending on flow speed and direction. Each cast took about 30 seconds to perform. The sound velocity data at this position was assumed representative of the channel and used to localize all μFloats during the survey cycle.

5.2.3 Deployment Layouts and Times

On the 20 August 2020, four surveys were performed during ebb tide (E1-F4) and five during flood tide (F1-F5), for a total of nine surveys, each indicated by the grey regions in Figure 5.3. Surveys were performed by two small vessels (30 ft), each with a pilot and two crew members. The μFloats were programmed for underwater survey periods lasting 20 minutes, the approximate time necessary to traverse the region of interest at a speed of 1.5 m/s. Survey start times were chosen to coincide with the beginning of SWIFT data collection intervals to maximize data overlap in the region of interest. Approximately three minutes prior to the start of the survey period, the vessels performed a coordinated deployment

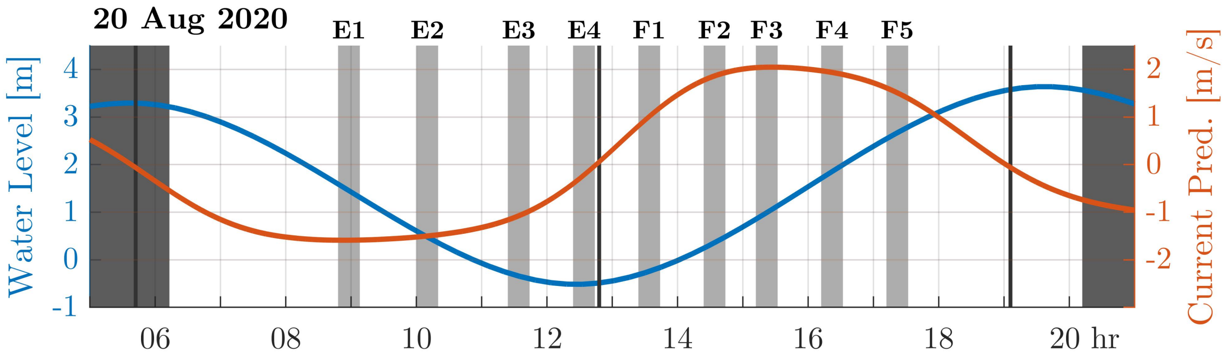

Figure 5.3: Predicted water level and tidal currents over the test day. Survey periods are indicated in light grey. Dark grey vertical lines indicate slack tide.

of the drifting devices, following the layout stencils shown in Figure 5.1c,d. One vessel primarily deployed SWIFTs and upstream SLBs while the other vessel deployed the μFloats and downstream SLBs. For float deployments, the vessel maintained a steady, low speed (3 m/s), and floats were tossed overboard every 5 s. Target depths (or max depths for profiling modes) were adjusted across the channel to provide a decent balance of vertical and horizontal sample distributions. SLBs were deployed around floats with the goal of maintaining robust connectivity of the nanomodems. Based on lessons learned about drift rates and paths during each survey cycle, SLB and SWIFT placements were adjusted to improve correspondence with μFloat tracks. In addition, during two of of the flood tests, one SLB was caught in an eddy just after passing under the highway bridge. These trapped SLBs were recovered and manually relocated back into the main channel to ensure continued connectivity. After all instruments were deployed, the first vessel executed the station-keeping ADCP surveys, while the second vessel drifted downstream with the SWIFTs, μFloats, and SLBs, as well as acquiring CTD profiles. Once the μFloats resurfaced and the station-keeping measurements were completed, both vessels participated in recovery efforts. Most instruments were found primarily by sight, but locating some μFloats relied on reference to a custom-built cellular-based GPS tracking app. Once all instruments were recovered, they were redistributed to their respective deployment vessel, vessels returned upstream, floats were reprogrammed with a new start time, and the process began again. Because of the variable time required to recover all the instruments, the interval between surveys was irregular (Figure 5.3). Recovery and reset during ebb tide typically took longer ($\sim$ 1 hour), with some instruments washing ashore on the north side of the channel and requiring assistance from friendly beach walkers, and some traveling out into Port Madison, where larger waves made visually locating μFloats particularly challenging. For flood tide, most instruments converged to within a small area, resulting in faster recovery and reset times ($\sim$ 40 min).

5.2.4 Data Analysis

To evaluate the effectiveness of μFloat data against SWIFT and station-keeping ADCP data, we compared horizontal velocity measurements across platforms in the following three modes: (1) time-evolution, (2) vertical profiles, and (3) horizontal gradients. Our secondary objective was to describe spatial and temporal current variations in Agate Pass.

We examined the mean-flow time-evolution by comparing measurements from all three instrument platforms against the NOAA current prediction [109]. NOAA predictions are provided at 2.7 m (9 ft) depth relative to mean-lower-low-water (MLLW) at a location approximately 50 m NE from SK2. As all instruments sample in a surface-relative coordinate frame, they must be shifted to a MLLW-reference coordinate frame by subtracting the time-varying water level. To compute the water level for each survey cycle, we interpolated the depth relative to MLLW from NOAA bathymetric data [108] at SK2. We then subtracted this nominal depth from the bottom-tracking depths measured by the vessel-keeping ADCP during the survey cycle and calculated the mean to produce the nominal water level for the given survey. This water level was then used to shift sample positions of all platforms to a MLLW-reference frame. For all platforms, SK2 served as the reference location for comparison to the NOAA predictions. For SWIFT data, the nearest profile within 150 m of SK2 was interpolated at 2.7 m depth. For μFloat data, all samples within 50 m horizontal radius of SK2 were binned by depth (0.5 m bin width) and bin averaged to produce a vertical profile. The profile was then linearly interpolated to 2.7 m depth. During slack tide (E4), no

μFloat samples were obtained near the NOAA prediction location. Note that for all other inter-platform comparisons, data was left in surface-referenced coordinates.

To examine vertical structure, we compared velocity profiles from all platforms at each station-keeping location, using vessel-mounted ADCP data as reference ground truth. For SWIFT data, the closest profile within 50 m of the station-keeping location was selected. For μFloats, we assembled all 30-second-averaged μFloat data into a three-dimensional linear interpolation function. We queried the interpolation function at the station-keeping locations at 0.5 m depth intervals from surface to sea-floor. Due to insufficient coverage during ebb deployments, interpolation at SK3 was not possible.

To extend these comparisons over the entire channel, the μFloat swarm data was compared to the SWIFT data. The interpolation functions constructed from μFloat data were queried at each SWIFT data point. Median, interquartile range, and interdecile range of the difference between SWIFT and swarm measurements were computed from all samples in a given survey cycle. The median absolute difference (MAD) serves as the overall figure of merit.

To examine the horizontal distribution of horizontal velocity magnitude, we interpolated the swarm data at 2 m depth over the entire domain (as shown in Section 5.3, μFloat resolution was superior to the SWIFTs for this data product). The nominal horizontal extent of the μFloat samples was identified using MATLABs 'boundary' function, adjusting the 'shrink' parameter to produce a realistic boundary. No extrapolations were made outside this boundary.

To compare the spatial coverage provided by the swarm relative to the SWIFTs, we computed the approximate horizontal and vertical sample distributions for each platform across all survey cycles. Horizontal coverage was defined as the area within the sample boundary. Horizontal resolution was computed by spatially binning samples taken by the given platform onto a uniform grid with 100 m resolution, and reported as the mean number of unique samples per grid cell. For SWIFTs, one profile was counted as one horizontal sample. Vertical resolution is similarly computed by vertically binning samples in 1 m depth bins, and reported as the mean number of samples per bin for the given survey and platform.

5.3 Results

5.3.1 Time Evolution

Figure 5.4 shows the time evolution of water level (a) and horizontal velocity (b) as compared with NOAA predictions, as well as the observed sound speed and density profiles taken during each survey cycle (c,d). A phase lag of about 1 hour is evident in both water level and maximum ebb velocity, though not on the flood. Observed water velocity accelerates more quickly on flood than predicted, as recorded in prior bottom-mounted ADCP measurements [163], indicating the presence of an 'aharmonic' feature of the tidal currents [116]. Overall, sound speed and density profiles are relatively consistent in time. The mild sound speed and density gradient on ebb and slack (E4) surveys derives from a slight thermocline (Fig. 5.4c,d), indicating that the shallower waters of Port Orchard are warmer than Puget Sound. Additionally, the relatively uniform sound speed profile is favorable for acoustic localizations (i.e., the sound speed profile does not trap localization pings above float depth).

5.3.2 Vertical Profiles

Figure 5.5 depicts the depth-varying water speed at each station-keeping location as a function of time. As typical for open-channel flows, currents are strongest at the surface and diminish with depth. The velocity profiles observed are blunt, with relatively strong velocities near the seabed during all periods excepting slack tide (E4). The velocity profiles estimated by from the μFloats match the SWIFT and vessel-keeping data quite well (e.g., SK1 during F1-F5 and SK2 during E2 and F2-F4). Due to the variable coverage of the drifting platforms, data was insufficient for some surveys and stations. The sharp drop in surface currents indicated by some μFloat profiles (e.g., SK1 - E1,E3; SK2 - E1,F5; and SK3 - F5) are suspected interpolation artifacts, not erroneous measurements.

An examination of the difference between SWIFT and float measurements across the

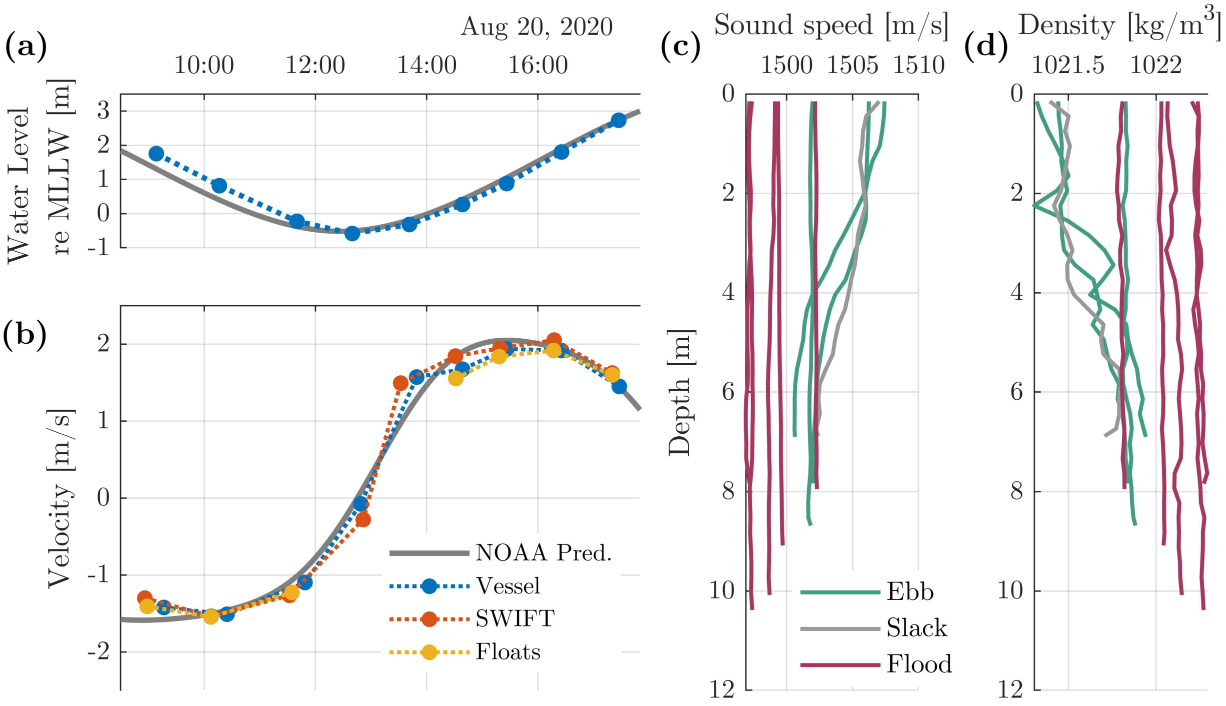

Figure 5.4: Time evolution of (a) water level estimated from vessel-keeping ADCP and (b) horizontal velocity measured from all devices, as compared to NOAA prediction. Profiles of sound speed (c) and water density (d) were taken during each survey cycle.

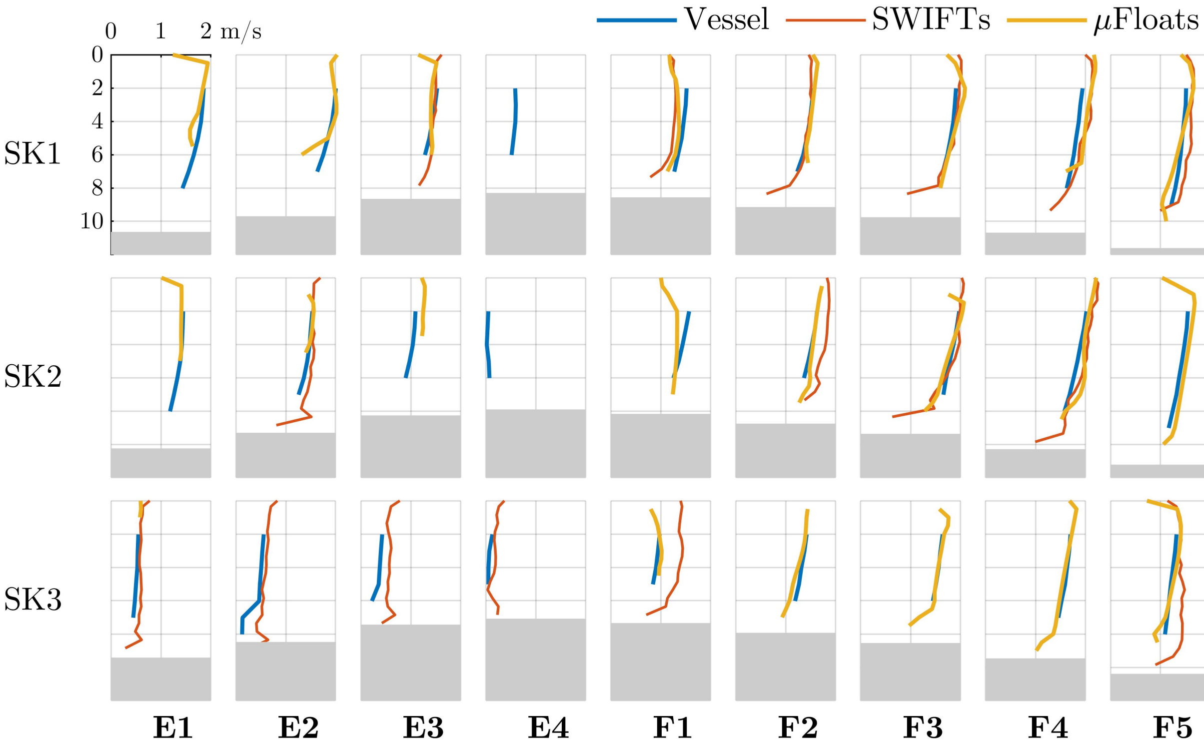

Figure 5.5: Current speed vs. depth at each station-keeping location. Variable coverage and deployment locations resulted in insufficient data for float profiles at SK3 during ebb, and all stations at slack (E4), Similarly, SWIFT coverage was insufficient for various surveys and locations.

Table 5.1: Measurement differences between SWIFTs and μFloats over tidal cycle. The white lines, thick grey bars, and thin grey lines indicate median, interquartile range, and interdecile range respectively. Percentage is MAD/Speed.

Survey	Speed [m/s]	nEval	$U_{\mu\text{Float}}$ - U_{SWIFT}	MAD [m/s]	%
E1	1.4	587	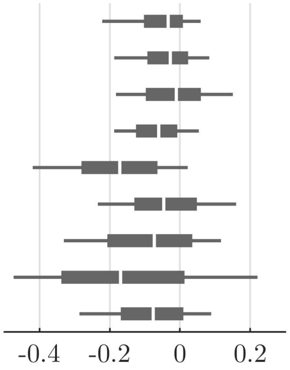	0.06	4.2
E2	1.5	611		0.06	4.0
E3	1.1	746		0.08	7.1
E4	0.1	313		0.08	95.0
F1	1.6	1103		0.17	11.1
F2	1.7	1076		0.10	5.7
F3	1.9	927		0.12	6.2
F4	1.9	776		0.22	11.4
F5	1.4	1232		0.10	7.1

all surveys (Table 5.1) reveals median absolute deviations (MAD) within about 10% of the nominal velocity (with the exception of slack tide E4, where flow speed is near zero). Additionally, no significant difference is observed between profiling (E1, E3, F1, F3, F5) and depth-tracking (E2, E4, F2, F4) float control modes.

5.3.3 Coverage and Resolution

As evident in the profile data, the SWIFTs and μFloats provide variable spatial coverage resulting from changes in deployment distribution and advection trajectories. Figures 5.6 and 5.7 offer an inter-platform comparison of float and SWIFT sampling during a representative ebb (E2) and flood (F4) deployment, respectively. Because both SWIFTs and floats were deployed at similar stream-wise locations and distributed evenly across the channel, the across-channel measurement extents are roughly equivalent and the along-channel extents are proportional to the advective velocity (Table 5.2). While the SWIFTs provide about twice as many samples as the float swarm (Table 5.2), they are horizontally sparse. Thus, the float swarm provides better horizontal resolution than the SWIFTs, as shown in Figure

Table 5.2: Sampling statistics for SWIFTs and μFloats over tidal cycle

			SWIFTs			μFloats			
Tide	Speed m/s	Coverage km^2	Samples	Horz. Res. #/(100 m)^2	Vert. Res. #/1 m	Samples	Horz. Res. #/(100 m)^2	Vert. Res. #/1 m	Mode
E1	1.4	0.48	1619	4	316	639	9	90	Profiling
E2	1.5	0.55	1412	3	277	715	10	72	Constant
E3	1.1	0.36	1419	3	236	720	12	94	Profiling
E4	0.1	0.14	1348	8	246	364	12	57	Constant
F1	1.6	0.28	2257	3	267	617	11	70	Constant
F2	1.7	0.27	2073	3	234	834	14	100	Profiling
F3	1.9	0.35	3184	3	283	691	11	72	Constant
F4	1.9	0.43	2442	2	223	837	11	74	Profiling
F5	1.4	0.31	2472	3	250	610	12	59	Constant

5.6(a,d) and 5.7(a,d). The SWIFTs provide consistent vertical resolution of 0.5 m from surface to the sea floor, with full range up to 20 m. Vertical coverage provided by the floats is less consistent and coarser, with sampling determined either by the set of depths for constant-depth floats, or the max depth for profiling floats. Profiling mode does appear to offer better distribution of vertical samples (Table 5.2), but may vertically average horizontal velocity in locations with stronger vertical shear than Agate Pass.

Horizontal Distribution of Currents

Figure 5.8 shows the horizontal velocity magnitude at 2 m depth over the domain, as resolved by the float swarm. During the ebb tide (E2, E3), the flow accelerates as it enters the channel, with peak currents observed in the center of the channel. On the flood tide (F3, F4), both the distributions and constituent floats trajectories (e.g., Fig. 5.7b) reveal a jet exiting the south end of the channel and extending along the thalweg the bay (for bathymetry, refer to Fig. 5.1b).

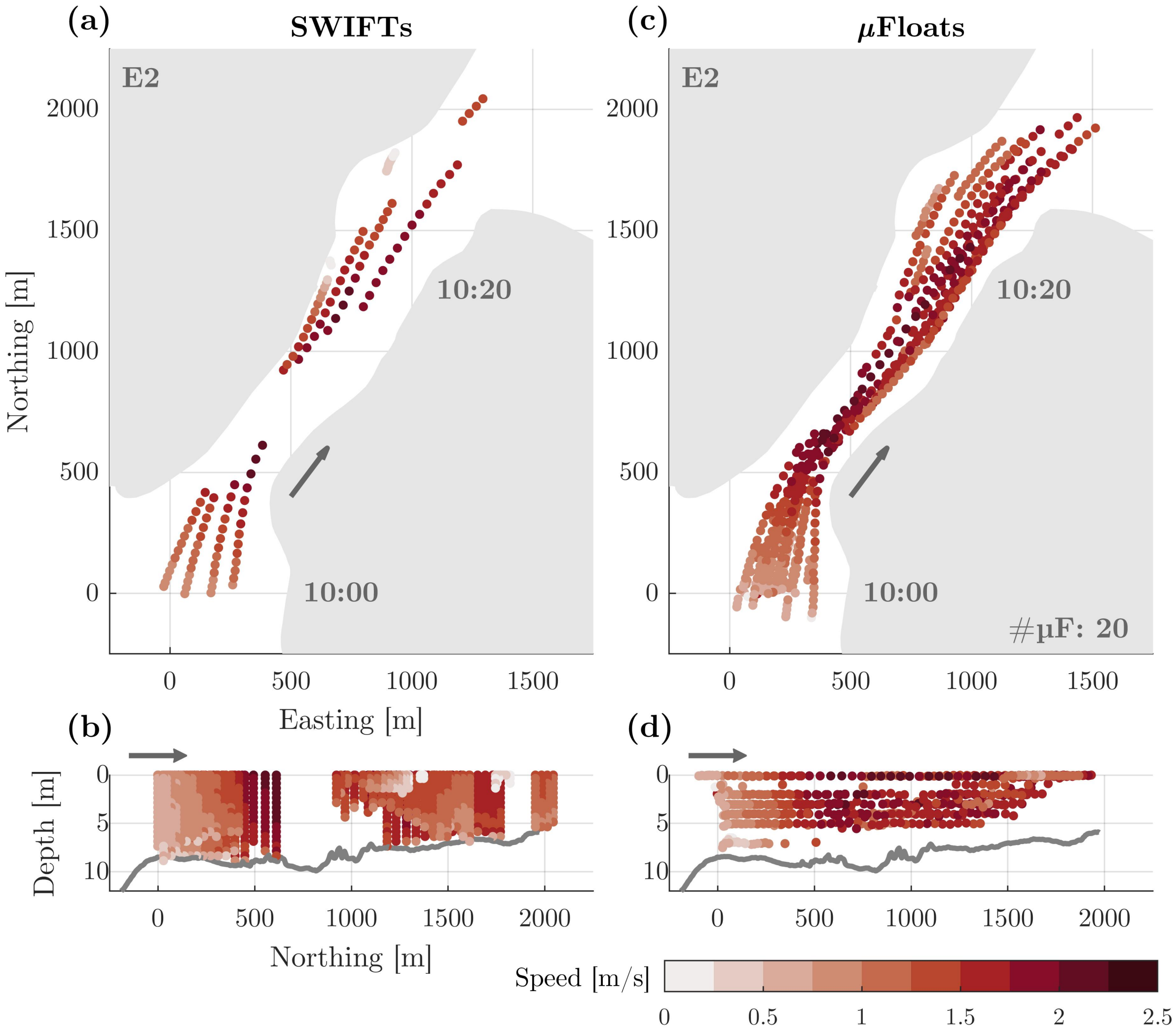

Figure 5.6: Distribution of SWIFT (a,b) and float (c,d) samples during E2 deployment. Gaps in SWIFT data occur during onboard processing periods. Floats were programmed to hold constant depth during this survey cycle. Note (b,d) are projected onto the Northing ordinate, with west pointing into the page. The grey line indicates bathymetry along the thalweg.

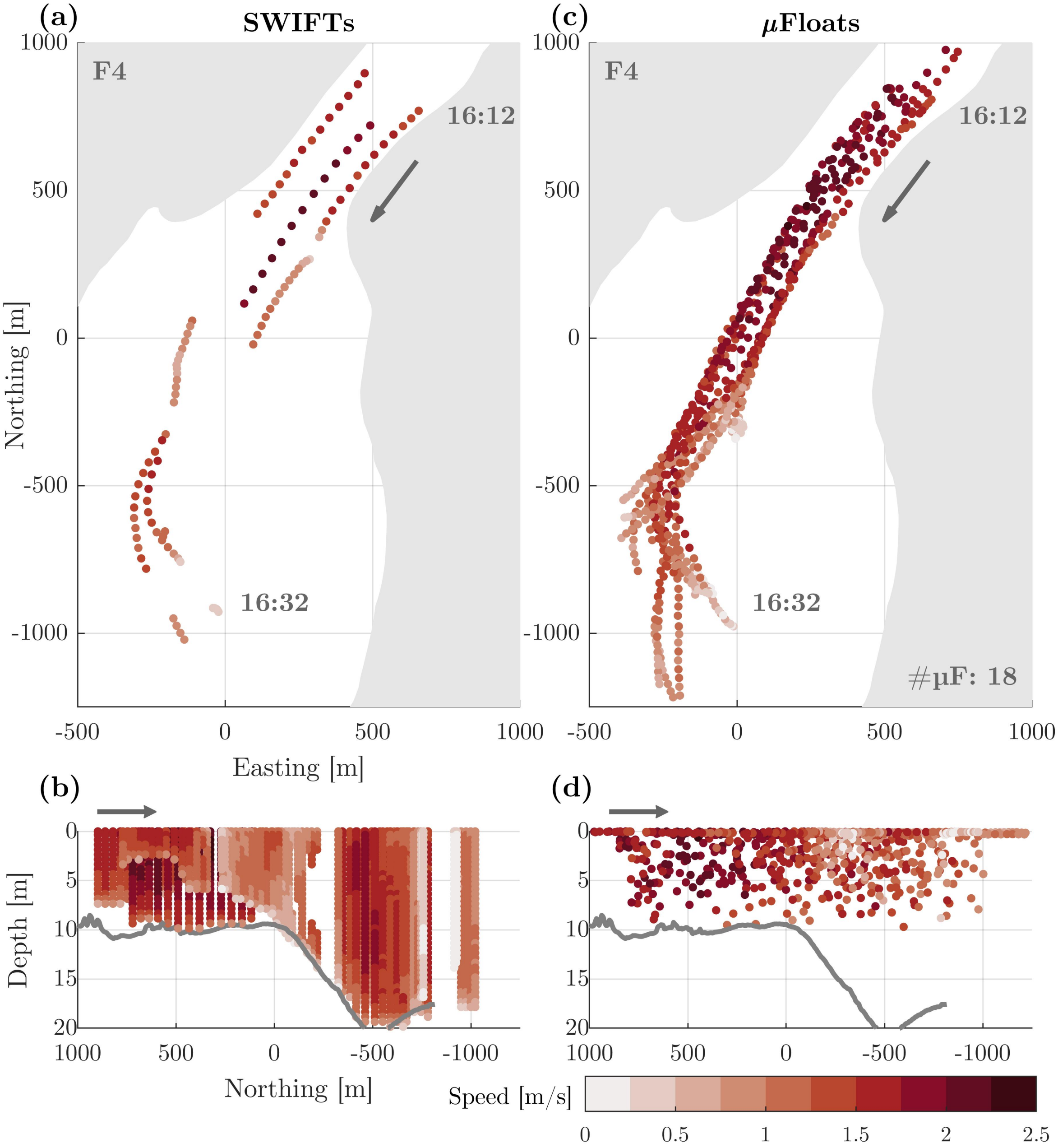

Figure 5.7: Distribution of SWIFT (a,b) and float (c,d) samples during F4 deployment. Floats were programmed to profile during this survey. Note (b,d) are projected onto the Northing ordinate, with east pointing into the page. The grey line indicates bathymetry along the thalweg.

5.3.4 Eddies

Examination of the μFloat tracks during F3 and F4 reveal circular trajectories on the southeastern edge of the jet, indicating eddies shed from the jet (Fig. 5.8). Approximately five minutes after entering the eddies, the floats began recovery mode, and consequently surfaced and rejoined the primary flow. This behavior, along with the variations in trajectory with float depth (e.g., during F3, the three floats that were entrained in the eddy were at 2, 4, and 5 m) suggests a sub-surface flow feature with depth-varying structure.

5.4 Discussion

5.4.1 Characteristics of Agate Pass Tidal Currents

The nine surveys provide significant spatial and temporal detail of the tidal current at the south end of Agate Pass, a domain roughly 2 km long and varying from 300 m across in the channel to 1 km across in Port Orchard. As tides here are mixed-semidiurnal, ebb and flood velocities vary considerably throughout the lunar month. As such, a full site characterization would require repeated surveys over multiple days. The surveys presented here only resolved one strong exchange from peak ebb to peak flood. Flow dynamics and the resulting horizontal and vertical gradients for weaker exchanges are expected to be quite different. As floats may quickly leave the area of interest and thus require near-constant supervision, they are not well-suited for long-duration surveys to extract tidal constituents. Such a task is better suited to bottom-mounted, stationary ADCPs for vertical resolution [100] or shore-mounted X-band radar systems for horizontal resolution [10]. A comprehensive characterization of flow conditions could be achieved by coupling distributed sampling (such as that performed by the SWIFTs and float swarms) over a number of days that include a representative set of tidal current magnitudes with continuous, multi-month data from a bottom-mounted ADCP.

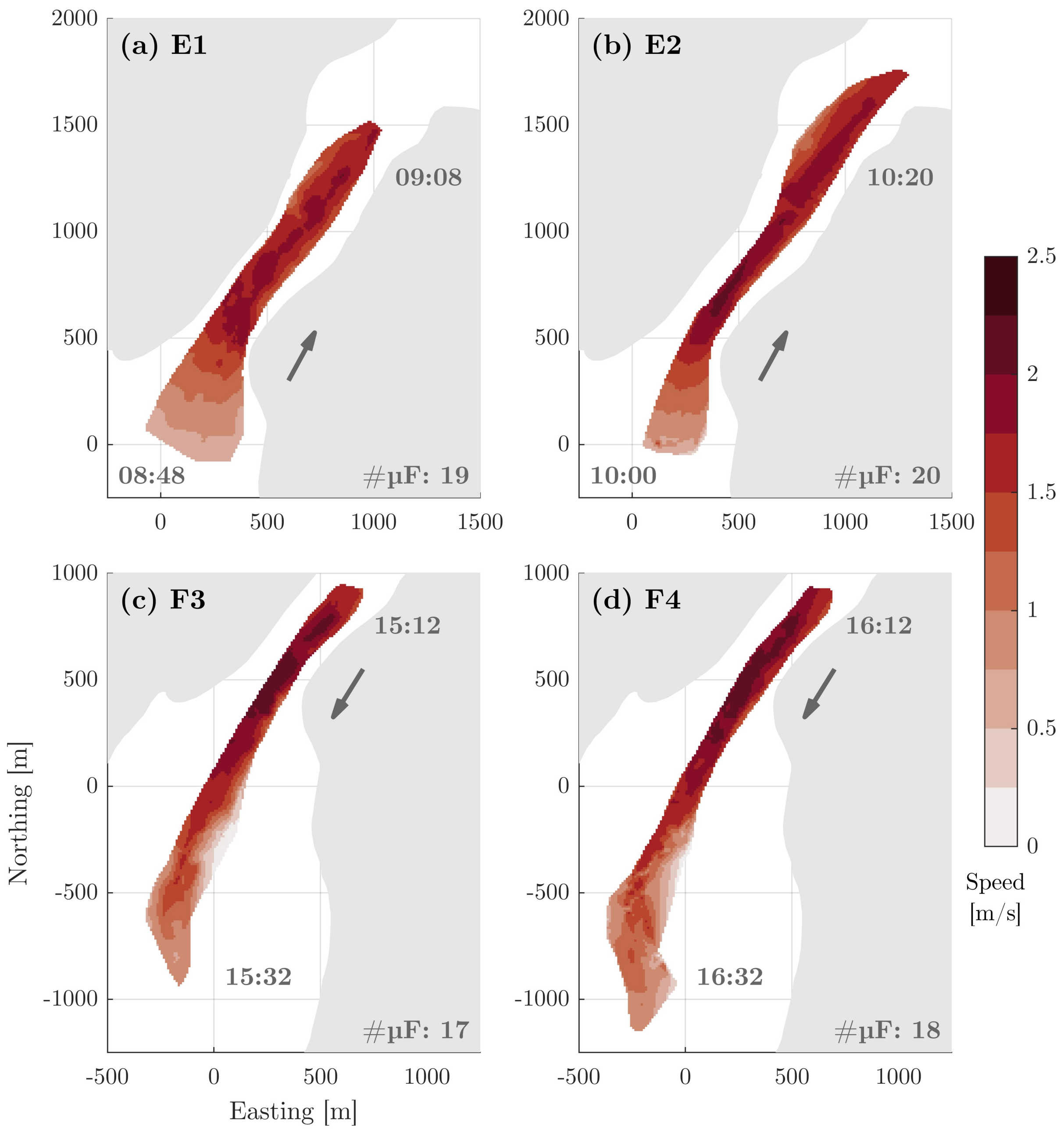

Figure 5.8: Horizontal distribution of currents at 2 m depth, as interpolated from μFloat swarm data, for surveys E1, E2, F3 and F4.

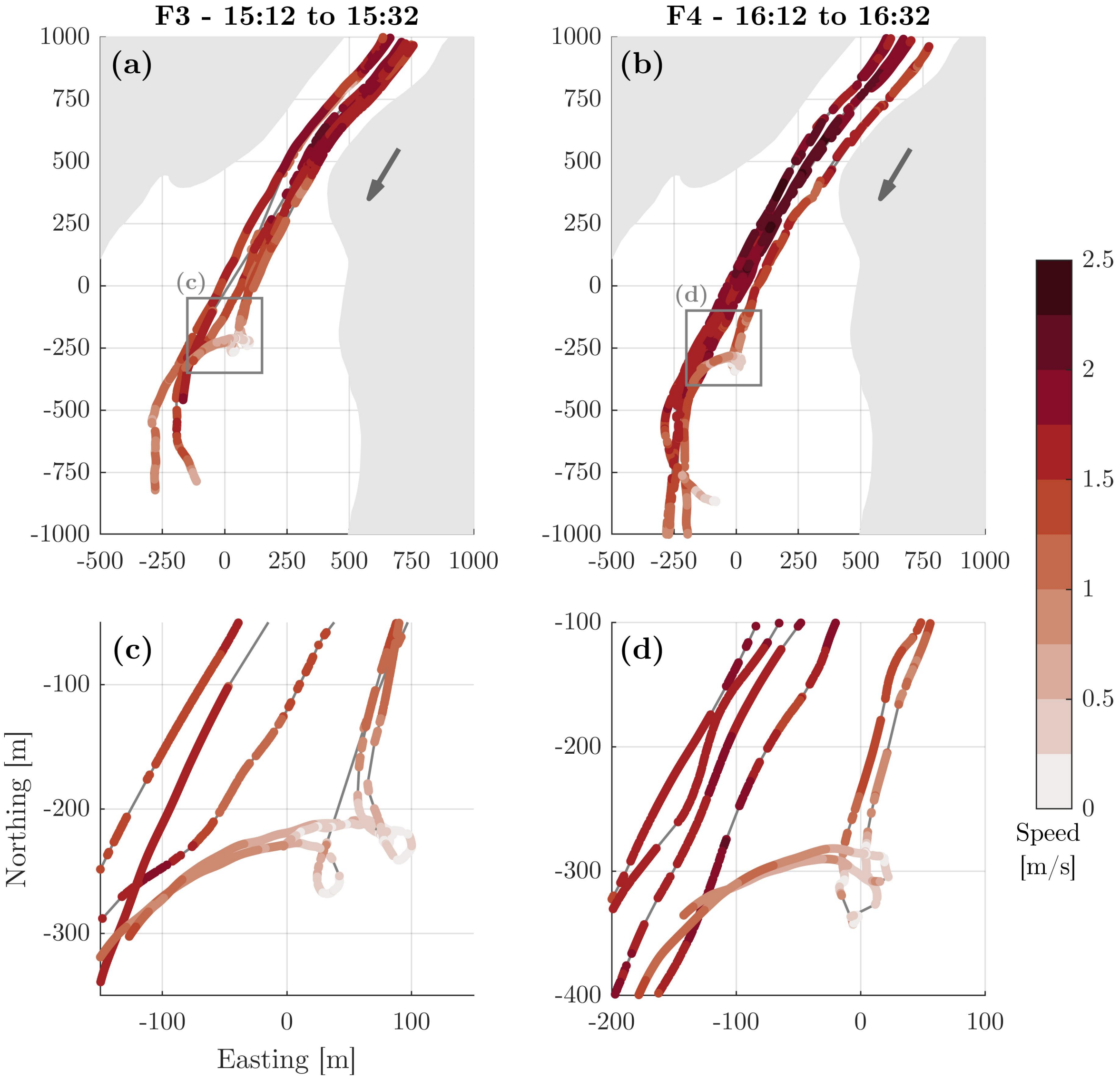

Figure 5.9: Float tracks during flood surveys F3 (a) and F4 (b) showed evidence of entrainment in eddies shedding from channel jet. (c) and (d) provide detail of float trajectories in the region of the probable eddy. Only a subset of tracks are shown for clarity and include floats at multiple depths. Note that this is the full-resolution float data, rather than the 30-s averages used for comparison with ADCP data.

5.4.2 Inter-platform Comparison

In general, we see excellent agreement between water velocity inferred from μFloat trajectories and velocity measured by station-keeping and drifting ADCPs. This suggests that the μFloats are acceptably Lagrangian and can provide accurate horizontally and vertically distributed measurements of horizontal water velocity. Evidence of μfloat Lagrangianness is bolstered by individual float tracks that suggest entrainment in depth-varying eddies (Fig. 5.9). However, since the μFloats are actively controlling depth, they cannot be considered fully Lagrangian, particularly with regards to tracking vertical motion.

The μFloat swarm provides more economic sampling coverage and horizontal resolution than the four SWIFTs, as the swarm and SLB cost is approximately one quarter that of four SWIFTS ($75k vs $300k), albeit with some noteable caveats. First, recovery of twenty-five drifting instruments – especially the μFloats which are smaller and harder to see – takes considerably more time than recovery of four SWIFTs. By deploying only SWIFTs, the inter-survey gaps could be reduced, thus increasing temporal coverage and total samples. Also, SWIFT recovery is not restricted by the pre-programmed time interval (as on the floats), allowing more flexible deployment schedules and locations. Conversely, the floats capture Lagrangian dynamics the ADCPs cannot easily resolve, such as the eddy tracks observed during surveys F2 and F3.

5.4.3 Contributions from SLBs

While the SLBs are necessary for localizing the μFloats, they are themselves surface drifters. Thus, if their motion is Lagrangian, their track data can be combined with the μFloat data to augment swarm coverage. To assess this possibility, we combined the SLB tracks (30-second averages, matching the processing of the SWIFTs and μFloats), and incorporated these points into the vertical velocity profiles at the station-keeping locations in Figure 5.10. The SLBs remove interpolation errors observed near the surface in profiles derived solely from the μFloat swarm (Fig. 5.5) and suggests that, for this survey, the SLBs acted as Langrangian

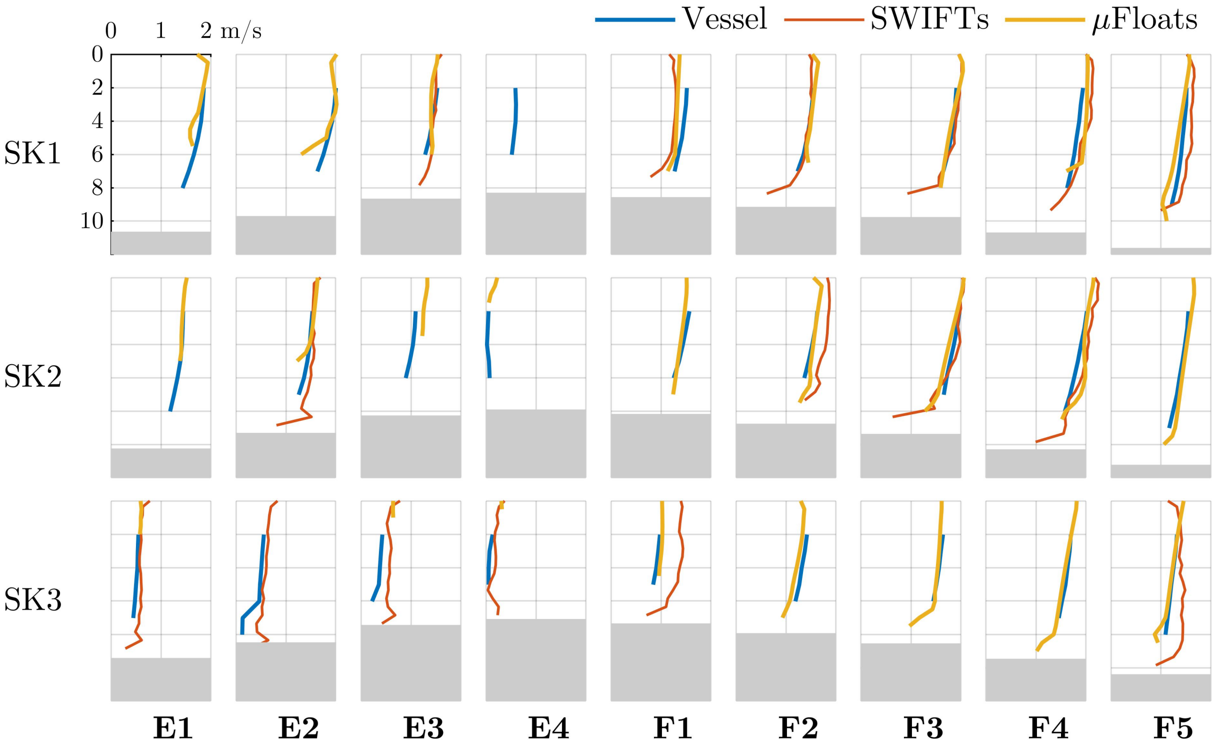

Figure 5.10: Velocity profiles at all station keeping locations over all surveys. This figure is identical to Fig. 5.5, except that μFloat profiles include data from SLB tracks, contributing to improved near-surface velocity measurements.

drifters in the near-surface currents. Such dynamics are not universally guaranteed due to potential for wind-induced relative motion. The surface expression of the SLBs is quite large relative to the subsurface expression ($\sim$ 1:1 ratio). As a result, even light winds can generate relative velocities between the SLB and surface currents, as was observed in quiescent flow lake tests when benchmarking the μFloat system (Chapter 4). Thus, SLB tracks can provide additional useful information, though careful consideration of wind effects is critical when integrating SLB and μFloat data.

5.4.4 In-situ Swarm Sampling

As discussed in Section 2.4.6, an important benefit of a Lagrangian float swarm is the potential to obtain *in situ* data that, unlike velocity, cannot be remotely sensed. The μFloats are all equipped with a temperature sensor (Blue Robotics, ±0.1 °C accuracy, 1 second response time). Figure 5.11 shows the vertical temperature gradients estimated from μFloat data over the ebb cycles. To produce these estimates, we depth-binned the float data at 0.5 m resolution, then performed a distance-weighted average of samples within 100 m of the CTD profile location. The μFloat data matches the CTD reasonable well, with deviations likely resulting from the spatial interpolation. Figure 5.12 displays float trajectories during surveys F2-F5, colored by temperature. This reveals a consistent temperature gradient across the channel, with water cooler on the southern edge and warmer on the northern, which may be indicative of water originating from different locations in Puget Sound. While further benchmarking of μFloat temperature measurements are required, this is a compelling demonstration of swarm measurements that capture vertical and horizontal gradients of *in situ* properties.

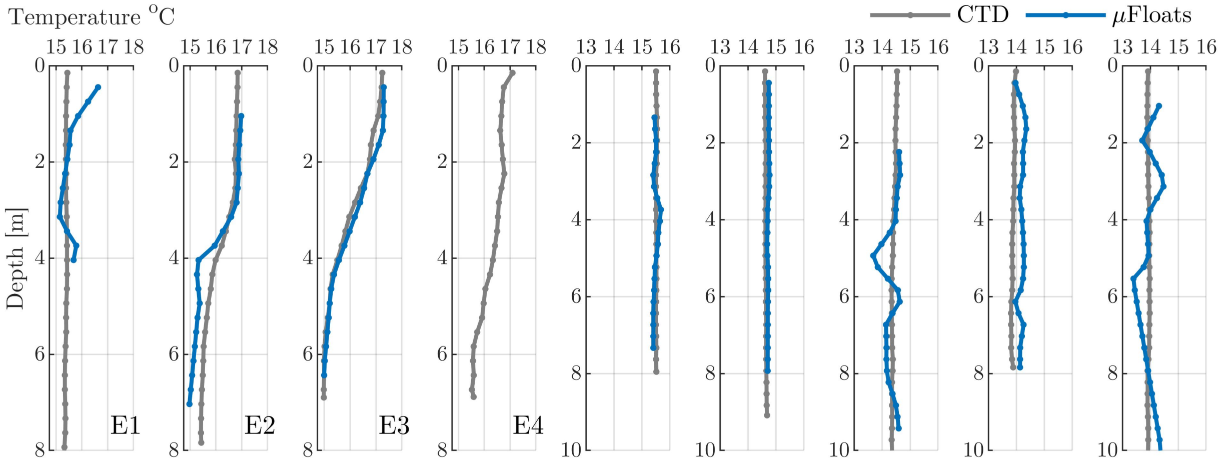

Figure 5.11: Temperature profiles estimated from the μFloats relative to CTD measurements.

Additionally, one μFloat was equipped with a downward facing camera (GoPro Session 5) and LED dive lights for opportunistic benthic composition surveys between SK2 and SK3. The resulting data was of variable quality, but did show that bottom composition in the area of the channel with strong currents was primarily scoured to cobble, as expected for high energy sites. A video taken during slack tide east of this region revealed a sandy bottom populated by crabs, starfish, and a few fish – evidence that flow in that area remains low throughout the tidal cycle. However, two control behaviors of the μFloat degrade the quality of benthic surveys. First, the buoyancy engine motor induces considerable rotational motion while holding depth. Second, because the float holds constant depth, the relative distance to bottom is difficult to assess and the size of objects on the bottom is ambiguous. Addition of an altimeter, as implemented by Roman et al. [121], would improve these results, as would a control algorithm that reduces actuation.

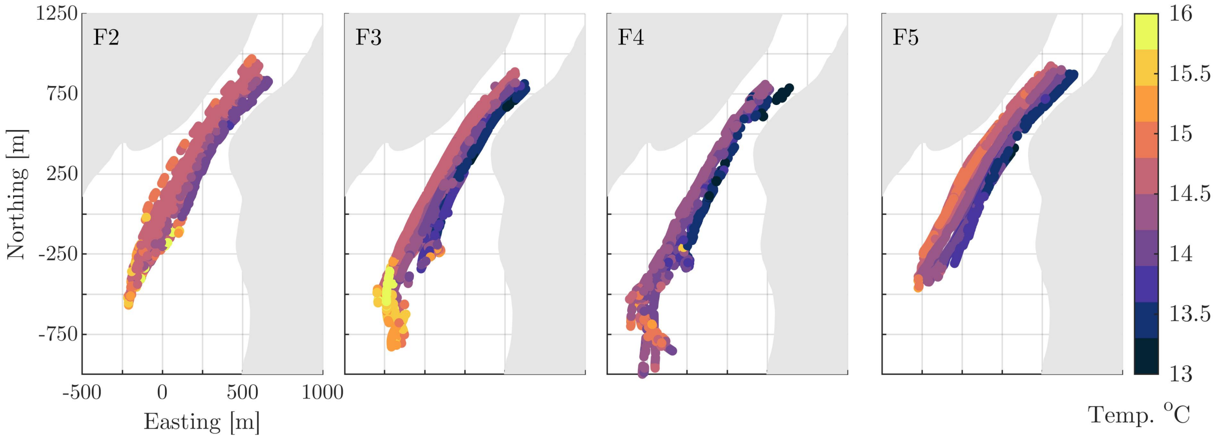

Figure 5.12: Horizontal distributions of temperature as measured by the μFloats during surveys F2-F4. Note that float depths vary along the tracks, but temperature during flood is well-mixed vertically, as seen in Fig. 5.11)

Chapter 6

CONCLUSIONS AND FUTURE WORK

6.1 Conclusion

This thesis describes the potential benefit and demonstrated success of underwater float swarms towards the objective of distributed, high-resolution, three-dimensional measurements in coastal waterways.

Chapter 2 addresses two questions. First, could a swarm of underwater floats, comprised of an operationally feasible number ($<$ 100 floats), provide an accurate assessment of tidal currents? Second, how would the resulting measurements compare against observations from standard methods? To answer these questions, a virtual field experiment compared volumetric mapping of tidal currents by floats swarms against standard platforms (X-band radar and ADCPs). Results suggested that, for high-resolution $O(1)$ m, small area surveys $O(1 \text{ km})$, mobile surveys with vessel-mounted ADCPs provide the highest accuracy, though float swarms are nearly as accurate. The performance hierarchy persists over most locations and stages of the tide. However, for longer duration surveys ($> O(1\text{-}10)$ days), a combined deployment with a stationary ADCP and X-band radar system is the best choice. Lastly, float swarms offer a unique benefit over the other platforms: they can simultaneously map *in situ* measurements of scalar properties (e.g., salinity, temperature, dissolved oxygen) while resolving tidal currents.

In Chapter 3, we reviewed the design requirements for a coastal float and introduced the μFloat, a buoyancy-controlled float designed specifically for adaptable, economic, swarm sensing in coastal waterways. The μFloat is equipped with a high-capacity buoyancy engine that provides a 9% density change, enabling automatic ballasting and vertical control from fresh to salt water ($\sim$ 3% density change), while maintaining reserve capacity for external sensors. An array of GPS-tracked surface localization buoys (SLBs) based on inexpensive, low-bandwidth, bi-directional acoustic nanomodems provides subsurface localization. The low unit cost (\$2.4k/μFloat and \$3k/SLB) permitted construction of twenty five μFloats and five SLBs for a total system cost of \$75k. With the reduction in unit cost and oversize buoyancy engine capacity, the μFloat fills the technological gap in available coastal float platforms outlined in the Introduction (1.4).

To benchmark μFloat system performance and establish the scientific validity of gathered data sets, we performed a multitude of laboratory, test tank, and field tests. Chapter 4 describes the most recent tests evaluating float performance, specifically performance of the buoyancy engine and localization systems. The three tests discussed are a quiescent-flow test in Lake Washington, a controlled disturbance test in a salt water test tank, and a tidal-current mapping demonstration in Agate Pass, WA. A summary of the system performance characteristics observed in these tests, along with their operational and scientific implications, are provided in Table 6.1. Most critically, the floats displayed depth-holding accuracy equivalent to the best previously reported. However, μFloats are relatively inefficient due to high hotel power loads and near-constant piston movements when depth-seeking and depth-holding. Additionally, several floats were equipped with external sensors (¡10% nominal float volume) without appreciably altering their dynamic response. Performance of the nanomodem-based SLB array was shown to localize the floats within ± 5 m, with primary errors resulting from sound speed gradients (in Lake Washington) and unfavorable array geometry (in Agate Pass). These results clearly demonstrate that the depth control and positioning accuracy sufficient for producing scientifically accurate and relevant data sets throughout the range of conditions present in coastal waterways.

In Chapter 5, we described the tidal channel deployment of the μFloat swarm in Agate Pass, WA over a series of nine survey cycles performed from ebb to flood, during which maximum observed currents exceeded 2 m/s. While the hydrodynamics of Agate Pass were not scientifically novel, the results were technologically compelling. We showed that μFloat measurements of horizontal velocity magnitude matched those from the drifting ADCPs

Table 6.1: μFloat System Performance Metrics

Metric	μFloat	Performance Implication	Science Capability
Buoyancy Control – Vertical Position			
Settling Time (step change)	15 s + 0.4 s/dbar	Impacts scheduling	Path-planning; precision of intended sampling distribution of field measurements.
Overshoot (step change)	< 5 m (control dependant)	Prevent actuation beyond 100 m limit or undesired bottom interactions	Path-planning; precision of intended sampling distribution of field measurements.
Depth-holding accuracy	$< \pm 0.2$ m (still water) $< \pm 0.5$ m (energetic flows)	Trustworthy sampling	Mean current measurement; biogeochemical measurements; internal wave sensing; creeping flows
Pressure drift	$< \pm 0.5$ dbar/hr ± 1 dbar max	For 1 hour at depth without pressure reset, float remains within 1.0 m of target depth.	Path-planning; internal wave sensing; time-evolution of biogeochemical field; residence time measurements.
Isobaric Disturbance Response	< 2 m deviation and max. 30 s away from target depth for upwelling ≤ 0.3 m/s	Maintain time at target depth; compensate for water density changes *in situ*	Mean current measurement; biogeochemical measurements; internal wave sensing;
Buoyancy Control – Vertical Velocity			
Maximum terminal magnitude	0.5 m/s	Quicker step-changes, improved success with path-planning; counter large vertical flow velocities in eddies	Path-planning; responding to vertical field accelerations;
Standard error	0.05 m/s	Controllable profile speed	Scalar field measurements at regular vertical intervals (salinity, DO, pH, etc.)
Buoyancy Control – Neutral Buoyancy			
Median volume deviation while holding depth	± 10 cc	Lagrangian-ness; power efficiency	Lagrangian statistics of flow; turbulence statistics; measurement of creeping flows
Underwater acoustic localization			
Range	~ 1 km	Distribution of GPS-tracked reference buoys; largest sensing spatial scale	Mean flow velocity measurements; path-planning
Position accuracy	± 10 m	Resolve horizontal gradients $> O(1)$ m	Mean flow velocity measurements; precision of known sampling distribution for field measurements
Velocity accuracy	± 0.1 m/s (High Flow) ± 0.05 m/s (Low Flow)	Dependent on localization connectivity; mean flow	Mean flow velocity measurements
Update rate	3 s	Resolve horizontal flow gradients $< O(10)$ m in 2 m/s currents	Mean flow velocity measurements; precision of known sampling distribution for field measurements;
Connectivity	50-70%	All pings contribute to localizations; Improved velocity estimates	Position accuracy; *in situ* command robustness;

within 10% of the nominal flow speed, validating the Lagrangian nature of the μFloats. Further evidence of their flow-following nature was observed in the looping tracks that suggested entertainment in eddies. Additionally, we demonstrated that a modest μFloat swarm comprised of twenty floats was able to resolve vertical gradients with accuracy near that of stationary and drifting ADCPs, while significantly improving horizontal coverage and resolution at lower instrument cost. Additionally, the μFloats provided *in situ* temperature measurements that approximately matched those from CTD profiles and was able to resolve strong horizontal gradient, bearing out the results from Chapter 2 simulation results. This test represented the first application of float swarms towards small-scale (< 1 km), high resolution (< 5 m) measurements that characterized mean currents and temperature in energetic tidal channels.

6.2 Future Work

The demonstrated success of the μFloat system enables several new avenues for engineering and scientific advancement.

6.2.1 Continued μFloat Development

First, the μFloat system is a prototype swarm and suffers from the usual challenges associated with immature technologies: software bugs, occasional mechanical issues, and idiosyncratic leaks resulted in loss of ~10% of field data, as well as five floats (two of which were later recovered, proving the value of 'If lost, call...' stickers). Continued design improvements, both incremental and generational, are likely necessary to improve the overall system robustness.

Second, the depth control mode demonstrated here limits scientific applicability, motivating expansion to profiling and isopycnal modes. Profiling was achieved in Agate Pass by careful scheduling of depth-control commands and implementation of a vertical velocity limit. More sophisticated methods, such as LQG control [110] or other state-space feedback control system [99] may improve performance for profiling and possibly reduce actuation required for depth control. Additionally, while the float is horizontally Lagrangian, the active depth control precludes truly three-dimensional Lagrangian behavior, as observed when floats were entrained in eddies in Agate Pass (Sec. 5.3.4). Thus, measurement of Lagrangian statistics, such as those achieved by D'Asaro's float [30], will require an isopyncal control mode. This may necessitate upgrading the float housing to reduce compressibility.

Third, the nanomodems currently implemented on the μFloats are already obsolete. The new generation (v3) features binary-phased-shift-keyed signals with a 10-fold increase in data rate, shorter and overlapping ping receptions, and improved error handling. This enables underwater GPS architecture (Jeff Neasham, pers. comm.) in which the μFloats could have knowledge of their current position while *in situ*. Once integrated, these promise improved connectivity as well as position and velocity measurements superior to those demonstrated here.

Fourth, we are investigating localization algorithm improvements. While localization accuracy from the trilateration method is excellent when acoustic conditions and SLB array distributions are favorable, a breakdown in either results in considerable errors. Potential improvements include probabilistic methods [152, 118, 17], or integration of inertial measurements for dead-reckoning between acoustic localizations [16, 36].

6.2.2 Scientific Applications

Having proven operational feasibility in tidal channels, we are now planning additional sensor integration to expand the μFloat scientific applications beyond water velocity and temperature measurements.

The μFloat system is potentially well suited to observing tidal plumes, fronts, and tidal bores. These systems have spatial extents on the order of 50 m–5 km wide [67], with dynamics evolving on tidal time scales (0.25-12 hours), matching the sensing scale of the swarm. Most critically, density gradients in these regions can range from mild in well-mixed regions to nearly step-changes between fresh and salt water across tidal bores – extreme conditions unmanageable for previous floats. As demonstrated by the disturbance test, the μFloat buoyancy engine capacity can handle such density gradients. A swarm of μFloats instrumented with salinity sensors could volumetrically map salinity to improve salt flux estimates [94].

Distributed acoustic monitoring is another application for floats. While in benchmark studies we used hydrophones to characterize the nanomodem performance, hydrophones are an important tool for studying underwater soundscapes, a critical parameter for the health of many ecosystems [37]. While traditional acoustic surveys use vertical or horizontal arrays of hydrophones [166, 93, 117], the μFloats would allow more flexible array arrangement that can be configured *in situ*. Additionally, the Lagrangian nature of the float should reduce flow-noise across the hydrophone element [9, 52, 84], improving fidelity of low-frequency noise measurements. This will require modifications to the depth control method to eliminate self-noise from near-constant motor actuation (for example, see Appendix B.1). The resulting motor noise contaminates environmental measurements, especially at low frequencies where a drifting platform promises improved performance. Additional benefits could be achieved by reducing float compressibility, adding a drag plate to dampen vertical motion, or upgrading the motor.

Lastly, the μFloats are a compelling platform for preliminary evaluation of environmentally-aided navigation techniques [79, 76, 69, 138] in which the float selects target depth based on hydrodynamic models of the local currents to perform a navigation task (e.g., station-keep, movement between points). Such a technique could enable float persistence in an energetic area of interest. While theoretical work has been performed, field testing remains sparse due to lack of appropriate technology. In coastal systems where such a technique is likely feasible (e.g., tidal channels), stationarity of the current field can be as short as 5 minutes [98]. The fast profiling speed of the μFloat provides access to its entire depth range within that time span and is thus suitable for evaluating these path-planning algorithms. However, because the methods rely on multiple tidal cycles, the current μFloat endurance is somewhat restrictive. Active ‘replenishment’ (i.e. exchanging an exhausted float for a fresh one) could work for early tests. With future advances in system efficiency and co-deployment with other autonomous platforms, such as surface vehicles [87, 77] for robotic swarm management (e.g. recovery and redeployment), the μFloat could become an integral part of coastal autonomous sampling networks [25, 24].

6.3 Final Words

Understanding the health and dynamics of our coastal waterways is of vital importance. Observational platforms, both remote and *in situ*, are critical to this endeavour. This dissertation expanded the suite of tools available to scientists studying coastal waters and the phenomena they contain with the introduction of the μFloat. While not the first float designed for coastal swarm deployments – that honor goes to Jaffe et al. [71] – the μFloat features a lower unit cost and oversize buoyancy engine that enables economic float swarm sensing across the wide range of conditions experienced in coastal environments. The research performed herein has shown, in both simulation and experimental tests, the ability of float swarms to simultaneously map tidal currents and *in situ* water properties in three-dimensions and high resolution, a capacity not previously demonstrated. Given the adaptable and inexpensive nature of the system, the μFloats are well-suited for future expansions. The benchmarking of core μFloat systems – buoyancy engine and underwater localization – will provide future scientists with a clear sense of platform capabilities and operational guidance. This work lays a foundation for the continued use of float swarms toward exploring the dynamics, physical properties, and soundscapes of our coastal waters.

BIBLIOGRAPHY

[1] Argo's status. https://argo.ucsd.edu/about/status/, 2021.

[2] Thomas AA Adcock, Scott Draper, and Takafumi Nishino. Tidal power generation–a review of hydrodynamic modelling. *Proceedings of the Institution of Mechanical Engineers, Part A: Journal of Power and Energy*, 229(7):755–771, 2015.

[3] Matthew H Alford, Michael C Gregg, and Eric A D'Asaro. Mixing, 3d mapping, and lagrangian evolution of a thermohaline intrusion. *Journal of physical oceanography*, 35 (9):1689–1711, 2005.

[4] G.P. Allen, J.C. Salomon, P. Bassoullet, Y. Du Penhoat, and C. De Grandpre. Effects of tides on mixing and suspended sediment transport in macrotidal estuaries. *Sedimentary Geology*, 26(1):69–90, 1980. ISSN 1365-3075, 0033-4545. doi: 10.1351/pac198052010233.

[5] Edgar An, Manhar R. Dhanak, Lynn K. Shay, Samuel Smith, and John Van Leer. Coastal Oceanography Using a Small AUV. *Journal of Atmospheric and Oceanic Technology*, 18(1):215–234, 2001. ISSN 0739-0572. doi: 10.1175/1520-0426(2001)018⟨0215:COUASA⟩2.0.CO;2.

[6] Katie K Arkema, Gregory M Verutes, Spencer A Wood, Chantalle Clarke-Samuels, Samir Rosado, Maritza Canto, Amy Rosenthal, Mary Ruckelshaus, Gregory Guannel, Jodie Toft, et al. Embedding ecosystem services in coastal planning leads to better outcomes for people and nature. *Proceedings of the National Academy of Sciences*, 112 (24):7390–7395, 2015.

[7] R. N. Bannister. A review of operational methods of variational and ensemble-variational data assimilation. *Quarterly Journal of the Royal Meteorological Society*, 143(703):607–633, 2017. ISSN 1477870X. doi: 10.1002/qj.2982.

[8] Edward B Barbier, Sally D Hacker, Chris Kennedy, Evamaria W Koch, Adrian C Stier, and Brian R Silliman. The value of estuarine and coastal ecosystem services. *Ecological monographs*, 81(2):169–193, 2011.

[9] Christopher Bassett, Jim Thomson, Peter H Dahl, and Brian Polagye. Flow-noise and turbulence in two tidal channels. *The Journal of the Acoustical Society of America*, 135(4):1764–1774, 2014.

[10] Paul S. Bell, John Lawrence, and Jennifer V. Norris. Determining currents from marine radar data in an extreme current environment at a tidal energy test site. *International Geoscience and Remote Sensing Symposium (IGARSS)*, pages 7647–7650, 2012. ISSN 2153-6996. doi: 10.1109/IGARSS.2012.6351856.

[11] LS Blunden and AS Bahaj. Tidal energy resource assessment for tidal stream generators. *Proceedings of the Institution of Mechanical Engineers, Part A: Journal of Power and Energy*, 221(2):137–146, 2007.

[12] Kenneth F Bowden. *Physical oceanography of coastal waters.* Ellis Horwood Series on Marine Science, 1983.

[13] Jenna Brown, Chris Tuggle, Jamie MacMahan, and Ad Reniers. The use of autonomous vehicles for spatially measuring mean velocity profiles in rivers and estuaries. *Intelligent Service Robotics*, 4(4):233–244, 2011. ISSN 18612776. doi: 10.1007/s11370-011-0095-6.

[14] Mario Cáceres, Arnoldo Vell-Levinson, and Larry Atkinson. Observations of cross-channel structure of flow in an energetic tidal channel. *Journal of Geophysical Research*, 108(C4):1–10, 2003. ISSN 0148-0227. doi: 10.1029/2001JC000968.

[15] Jeffrey Campana, Eric J. Terrill, and Tony de Paolo. A new inversion method to obtain upper-ocean current-depth profiles using X-band observations of deep-water waves. *Journal of Atmospheric and Oceanic Technology*, 34(5):957–970, 2017. ISSN 15200426. doi: 10.1175/JTECH-D-16-0120.1.

[16] Francois Caron, Emmanuel Duflos, Denis Pomorski, and Philippe Vanheeghe. Gps/imu data fusion using multisensor kalman filtering: introduction of contextual aspects. *Information fusion*, 7(2):221–230, 2006.

[17] David Casagrande, Kristopher Krasnosky, and Chris Roman. Localization of a drifting underwater vehicle using a terrain-based particle filter. In *OCEANS 2019 MTS/IEEE SEATTLE*, pages 1–8. IEEE, 2019.

[18] David S. Casagrande. *Real-time featureless visual odometry for sea floor imaging with a Lagrangian float.* Master of science in ocean engineering, University of Rhode Island, 2013.

[19] B Castelle, T Scott, R W Brander, and R J Mccarroll. Earth-Science Reviews Rip current types , circulation and hazard. *Earth Science Reviews*, 163:1–21, 2016. ISSN 0012-8252. doi: 10.1016/j.earscirev.2016.09.008.

[20] Grace C Chang and Tommy D Dickey. Interdisciplinary sampling strategies for detection and characterization of harmful algal blooms. *Real-time observation systems for ecosystem dynamics and harmful algal blooms. UNESCO, Paris*, 2005.

[21] Chen Chen, Shigeaki Shiotani, and Kenji Sasa. Numerical ship navigation based on weather and ocean simulation. *Ocean Engineering*, 69:44–53, 2013.

[22] Ralph T Cheng and Richard E Smith. A nowcast model for tides and tidal currents in san francisco bay, california. In *Ocean Community Conference, Baltimore, USA*. Citeseer, 1998.

[23] Daniel L. Codiga. A marine autonomous surface craft for long-duration, spatially explicit, multidisciplinary water column sampling in coastal and estuarine systems. *Journal of Atmospheric and Oceanic Technology*, 32(3):627–641, 2015. ISSN 15200426. doi: 10.1175/JTECH-D-14-00171.1.

[24] Thomas B Curtin and James G Bellingham. Progress toward autonomous ocean sampling networks. *Deep Sea Research Part II: Topical Studies in Oceanography*, 56(3-5): 62–67, 2009.

[25] Thomas B. Curtin, James G. Bellingham, Josko Catipovic, and Doug Webb. Autonomous oceanographic sampling networks. *Oceanography*, 6(3):86–94, 1993. ISSN 10428275, 2377617X. URL `http://www.jstor.org/stable/43924649`.

[26] Eric D'Asaro. Surface Wave Measurements from Subsurface Floats. *Journal of Atmospheric and Oceanic Technology*, 32(4):816–827, 2015. ISSN 0739-0572. doi: 10.1175/JTECH-D-14-00180.1.

[27] Eric A. D'Asaro. Performance of autonomous Lagrangian floats. *Journal of Atmospheric and Oceanic Technology*, 20(6):896–911, 2003. doi: https://doi.org/10.1175/1520-0426(2003)020⟨0896:POALF⟩2.0.CO;2.

[28] Eric A D'Asaro. Lagrangian trajectories on the oregon shelf during upwelling. *Continental shelf research*, 24(13-14):1421–1436, 2004.

[29] Eric A D'Asaro. Turbulence in the upper-ocean mixed layer. *Annual review of marine science*, 6:101–115, 2014.

[30] Eric A. D'Asaro, David M. Farmer, James T. Osse, and Geoffrey T. Dairiki. A Lagrangian Float. *Journal of Atmospheric and Oceanic Technology*, 13(6):1230–1246, 1996. doi: 10.1175/1520-0426(1996)0132.0.CO;2.

[31] Eric A. D'Asaro, Kriag B. Winters, and Ren-Chieh Lien. Lagrangian analysis of a convective mixed layer. *Journal of Geophysical Research*, 107(C5), 2002. ISSN 0148-0227. doi: 10.1029/2000JC000247.

[32] Russ E. Davis. Observing the general circulation with floats. *Deep Sea Research Part A. Oceanographic Research Papers*, 38:S531–S571, jan 1991. ISSN 01980149. doi: 10.1016/S0198-0149(12)80023-9.

[33] Zafer Defne and Neil K Ganju. Quantifying the residence time and flushing characteristics of a shallow, back-barrier estuary: Application of hydrodynamic and particle tracking models. *Estuaries and Coasts*, 38(5):1719–1734, 2015.

[34] R Walt Deppe, Jim Thomson, Brian Polagye, and Christopher Krembs. Hypoxic intrusions to puget sound from the ocean. In *2013 OCEANS-San Diego*, pages 1–9. IEEE, 2013.

[35] Tommy Dickey, Albert J Plueddemann, and Robert A Weller. Current and water property measurements in the coastal ocean. In Kenneth H. Brink and Allan R. Robinson, editors, *The Sea*, volume 10, pages 367–398. John Wiley & Sons, Inc., 1998.

[36] Glenn T Donovan. Position error correction for an autonomous underwater vehicle inertial navigation system (ins) using a particle filter. *IEEE Journal of Oceanic Engineering*, 37(3):431–445, 2012.

[37] Carlos M. Duarte, Lucille Chapuis, Shaun P. Collin, Daniel P. Costa, Reny P. Devassy, Victor M. Eguiluz, Christine Erbe, Timothy A. C. Gordon, Benjamin S. Halpern, Harry R. Harding, Michelle N. Havlik, Mark Meekan, Nathan D. Merchant, Jennifer L. Miksis-Olds, Miles Parsons, Milica Predragovic, Andrew N. Radford, Craig A. Radford, Stephen D. Simpson, Hans Slabbekoorn, Erica Staaterman, Ilse C. Van Opzeeland, Jana Winderen, Xiangliang Zhang, and Francis Juanes. The soundscape of the

anthropocene ocean. *Science*, 371(6529), 2021. ISSN 0036-8075. doi: 10.1126/science.aba4658. URL `https://science.sciencemag.org/content/371/6529/eaba4658`.

[38] Eric D'Asaro. Oceanographic floats: principles of operation. *Observing the oceans in real time*, pages 77–98, 2017.

[39] Eric A D'Asaro and Geoffrey T Dairiki. Turbulence intensity measurements in a wind-driven mixed layer. *Journal of physical oceanography*, 27(9):2009–2022, 1997.

[40] Eric A D'Asaro and Ren-Chieh Lien. Lagrangian measurements of waves and turbulence in stratified flows. *Journal of physical oceanography*, 30(3):641–655, 2000.

[41] Jeffrey Epler, Brian Polagye, and Jim Thomson. Shipboard acoustic Doppler current profiler surveys to assess tidal current resources. *MTS/IEEE Seattle, OCEANS 2010*, 2(1), 2010. doi: 10.1109/OCEANS.2010.5664387.

[42] Jon M Erlandson and Scott M Fitzpatrick. Oceans, islands, and coasts: current perspectives on the role of the sea in human prehistory. *Journal of Island & Coastal Archaeology*, 1(1):5–32, 2006.

[43] Davide Fenucci, Andrea Munafo, Alexander B Phillips, Jeffrey Neasham, Naomi Gold, Jeremy Sitbon, Iain Vincent, and Terry Sloane. Development of smart networks for navigation in dynamic underwater environments. In *2018 IEEE/OES Autonomous Underwater Vehicle Workshop (AUV)*, pages 1–6. IEEE, 2018.

[44] Derek A. Fong and Stephen G. Monismith. Evaluation of the accuracy of a ship-mounted, bottom-tracking adcp in a near-shore coastal flow. *Journal of Atmospheric and Oceanic Technology*, 21(7):1121–1128, 2004. doi: 10.1175/1520-0426(2004)021⟨1121:EOTAOA⟩2.0.CO;2.

[45] Michael GG Foreman, William R Crawford, and Richard F Marsden. De-tiding: Theory and practice. *Coastal and estuarine studies*, pages 203–203, 1995.

[46] Lee Freitag, Keenan Ball, James Partan, Peter Koski, and Sandipa Singh. Long range acoustic communications and navigation in the arctic. In *OCEANS 2015-MTS/IEEE Washington*, pages 1–5. IEEE, 2015.

[47] Josh Friedman. *Development of an X-band Radar Depth Inversion Model at the Sand Motor*. Master of science, Delft University of Technology, 2014.

[48] Oliver B Fringer, Clint N Dawson, Ruoying He, David K Ralston, and Y Joseph Zhang. The future of coastal and estuarine modeling: Findings from a workshop. *Ocean Modelling*, 143:101458, 2019.

[49] Lee-Lueng Fu and Rosemary Morrow. Remote sensing of the global ocean circulation. In *International Geophysics*, volume 103, pages 83–111. Elsevier, 2013.

[50] Rune Gangeskar. Ocean Current Estimated From X-Band Radar Sea Surface Images. *IEEE Transactions on Geoscience and Remote Sensing*, 40(4):783–792, 2002.

[51] W. Rockwell Geyer and Richard Signell. Measurements of tidal flow around a headland with a shipboard acoustic Doppler current profiler. *Journal of Geophysical Research*, 95(C3):3189, 1990. ISSN 0148-0227. doi: 10.1029/JC095iC03p03189.

[52] Jason I Gobat and Mark A Grosenbaugh. Modeling the mechanical and flow-induced noise on the surface suspended acoustic receiver. In *Oceans' 97. MTS/IEEE Conference Proceedings*, volume 2, pages 748–754. IEEE, 1997.

[53] Lonneke Goddijn-Murphy, David K Woolf, and Matthew C Easton. Current Patterns in the Inner Sound (Pentland Firth) from Underway ADCP Data. *Journal of Atmospheric and Oceanic Technology*, 30:96–111, 2013. doi: 10.1175/JTECH-D-11-00223.1.

[54] Gabriel Godin. On the predictability of currents. *The International Hydrographic Review*, 1983.

[55] Juan A. González-Castro and Marian Muste. Framework for Estimating Uncertainty of ADCP Measurements from a Moving Boat by Standardized Uncertainty Analysis. *Journal of Hydraulic Engineering*, 133(12):1390–1410, 2007. ISSN 0733-9429. doi: 10.1061/(ASCE)0733-9429(2007)133:12(1390).

[56] John Gould, Bernadette Sloyan, and Martin Visbeck. In situ ocean observations: A brief history, present status, and future directions. In *International Geophysics*, volume 103, pages 59–81. Elsevier, 2013.

[57] W John Gould. From swallow floats to argo—the development of neutrally buoyant floats. *Deep Sea Research Part II: Topical Studies in Oceanography*, 52(3-4):529–543, 2005.

[58] Florian Grossmann, Matthijs Gawehn, Sierd de Vries, Floris P de Wit, and Stefan GJ Aarninkhof. Comparison of currents derived from x-band radar and collected in-situ data in ameland inlet. *Coastal Structures 2019*, pages 416–425, 2019.

[59] Maricarmen Guerra and Jim Thomson. ORPC RivGen Wake Characterization. In *Marine Energy Technology Symposium*, Washington, D.C., 2016.

[60] Maricarmen Guerra and Jim Thomson. Turbulence measurements from five-beam acoustic doppler current profilers. *Journal of Atmospheric and Oceanic Technology*, 34 (6):1267–1284, 2017. ISSN 15200426. doi: 10.1175/JTECH-D-16-0148.1.

[61] Maricarmen Guerra, Rodrigo Cienfuegos, Jim Thomson, and Leandro Suarez. Tidal energy resource characterization in chacao channel, chile. *International journal of marine energy*, 20:1–16, 2017.

[62] D. B. Haidvogel, H. Arango, W. P. Budgell, B. D. Cornuelle, E. Curchitser, E. Di Lorenzo, K. Fennel, W. R. Geyer, A. J. Hermann, L. Lanerolle, J. Levin, J. C. McWilliams, A. J. Miller, A. M. Moore, T. M. Powell, A. F. Shchepetkin, C. R. Sherwood, R. P. Signell, J. C. Warner, and J. Wilkin. Ocean forecasting in terrain-following

coordinates: Formulation and skill assessment of the Regional Ocean Modeling System. *Journal of Computational Physics*, 227(7):3595–3624, 2008. ISSN 00219991. doi: 10.1016/j.jcp.2007.06.016.

[63] Trevor Harrison, Kristen M. Thyng, and Brian Polagye. Comparative evaluation of volumetric current measurements in a tidally dominated coastal setting: A virtual field experiment. *Journal of Atmospheric and Oceanic Technology*, 37(4):533–552, 2020. doi: 10.1175/JTECH-D-19-0131.1.

[64] Trevor W. Harrison, Kristen M. Thyng, and Brian Polayge. Supplementary matlab toolbox and data for 'comparative evaluation of volumetric current measurements in a tidally-dominated, coastal setting with an emphasis on float swarms'. `http://hdl.handle.net/1773/43825`, 2019. last accessed August 8, 2019.

[65] M. Reza Hashemi, Simon P. Neill, Peter E. Robins, Alan G. Davies, and Matt J. Lewis. Effect of waves on the tidal energy resource at a planned tidal stream array. *Renewable Energy*, 75:626 – 639, 2015. ISSN 0960-1481. doi: https://doi.org/10.1016/j.renene.2014.10.029.

[66] R. Heitsenrether, L. Fiorentino, D. W. Velasco, and W. D. Wilson. Evaluating performance of acoustic current profiler sensor on small, dynamic surface buoy. In *OCEANS 2018 MTS/IEEE Charleston*, pages 1–8, Oct 2018. doi: 10.1109/OCEANS.2018.8604697.

[67] Alexander R Horner-Devine, Robert D Hetland, and Daniel G Macdonald. Mixing and Transport in Coastal River Plumes. *Annual Review of Fluid Mechanics*, 2015. doi: 10.1146/annurev-fluid-010313-141408.

[68] Weimin Huang, Ruben Carrasco, Chengxi Shen, Eric W. Gill, and Jochen Horstmann. Surface current measurements using X-band marine radar with vertical polarization.

IEEE Transactions on Geoscience and Remote Sensing, 54(5):2988–2997, 2016. ISSN 01962892. doi: 10.1109/TGRS.2015.2509781.

[69] Van T Huynh, Matthew Dunbabin, and Ryan N Smith. Convergence-Guaranteed Time-Varying RRT Path Planning for Profiling Floats in 4-Dimensional Flow. In *Proceedings of the Australiasian Conference on Robotics and Automation*, 2014.

[70] Frederick H Imlay. The complete expressions for added mass of a rigid body moving in an ideal fluid. Technical report, DAVID TAYLOR MODEL BASIN WASHINGTON DC, 1961.

[71] Jules S Jaffe, Peter J S Franks, Paul L D Roberts, Diba Mirza, Curt Schurgers, Ryan Kastner, and Adrien Boch. A swarm of autonomous miniature underwater robot drifters for exploring submesoscale ocean dynamics. *Nature Communications*, 8:1–8, 2017. doi: 10.1038/ncomms14189.

[72] Steven R Jayne and Neil M Bogue. Air-deployable profiling floats. *Oceanography*, 30 (2):29–31, 2017.

[73] Steven R. Jayne, Dean Roemmich, Nathalie Zilberman, Stephen C. Riser, Kenneth S. Johnson, Gregory C. Johnson, and Stephen R. Piotrowicz. The argo program: Present and future. *Oceanography*, 30(2):18–28, 2017. ISSN 10428275, 2377617X. URL `http://www.jstor.org/stable/26201840`.

[74] Guangzhen Jin, Haidong Pan, Qilin Zhang, Xianqing Lv, Wei Zhao, and Yuan Gao. Determination of harmonic parameters with temporal variations: An enhanced harmonic analysis algorithm and application to internal tidal currents in the south china sea. *Journal of atmospheric and oceanic technology*, 35(7):1375–1398, 2018.

[75] Richard W. Johnson. *Handbook of fluid dynamics*. CRC Press, Boca Raton, FL, second edition. edition, 2016. ISBN 9781439849576.

[76] Jerome Jouffroy, Qiuyang Zhou, and Oliver Zielinski. Towards selective tidal-stream transport for lagrangian profilers. *Oceans 2011*, pages 1–6, 2011. URL `http://ieeexplore.ieee.org/xpls/abs{\_}all.jsp?arnumber=6107000`.

[77] Peter Kimball, John Bailey, Sarah Das, Rocky Geyer, Trevor Harrison, Clay Kunz, Kevin Manganini, Ken Mankoff, Katie Samuelson, Thomas Sayre-McCord, et al. The whoi jetyak: An autonomous surface vehicle for oceanographic research in shallow or dangerous waters. In *2014 IEEE/OES Autonomous Underwater Vehicles (AUV)*, pages 1–7. IEEE, 2014.

[78] D. Kruger, R. Stolkin, A. Blum, and J. Briganti. Optimal auv path planning for extended missions in complex, fast-flowing estuarine environments. In *Proceedings 2007 IEEE International Conference on Robotics and Automation*, pages 4265–4270, April 2007. doi: 10.1109/ROBOT.2007.364135.

[79] Lawrence C Langebrake, Chad E Lembke, Robert H Weisberg, Robert H Byrne, D Randy Russell, Graham Tilbury, and Raymond Carr. Design and initial results of a bottom stationing ocean profiler. *OCEANS 2002*, 2002. doi: 10.1109/OCEANS.2002.119325.

[80] Xinya Li, Zhiqun Daniel Deng, Lynn T. Rauchenstein, and Thomas J. Carlson. Contributed review: Source-localization algorithms and applications using time of arrival and time difference of arrival measurements. *Review of Scientific Instruments*, 87(4): 041502, 2016. doi: 10.1063/1.4947001.

[81] T. Liblik, J. Karstensen, P. Testor, P. Alenius, D. Hayes, S. Ruiz, K.J. Heywood, S. Pouliquen, L. Mortier, and E. Mauri. Potential for an underwater glider component as part of the global ocean observing system. *Methods in Oceanography*, 17:50–82, 2016. ISSN 2211-1220. doi: https://doi.org/10.1016/j.mio.2016.05.001. URL `https://www.sciencedirect.com/science/article/pii/S2211122016300056`. Special section on Novel instrumentation in Oceanography: a dedication to Rob Pinkel.

[82] R-C. Lien, E. a. D'Asaro, and M. J. McPhaden. Internal Waves and Turbulence in the Upper Central Equatorial Pacific: Lagrangian and Eulerian Observations. *Journal of Physical Oceanography*, 32(9):2619–2639, 2002. ISSN 0022-3670. doi: 10.1175/1520-0485-32.9.2619.

[83] Ren-Chieh Lien, Eric a. D'Asaro, and Geoffrey T. Dairiki. Lagrangian frequency spectra of vertical velocity and vorticity in high-Reynolds-number oceanic turbulence. *Journal of Fluid Mechanics*, 362:177–198, 1998. ISSN 00221120. doi: 10.1017/S0022112098008787.

[84] Michael James Lighthill. On sound generated aerodynamically ii. turbulence as a source of sound. *Proceedings of the Royal Society of London. Series A. Mathematical and Physical Sciences*, 222(1148):1–32, 1954.

[85] FMS Lima. Using surface integrals for checking archimedes' law of buoyancy. *European journal of physics*, 33(1):101, 2011.

[86] Yonggang Liu, Heather Kerkering, and Robert H. Weisberg. Chapter 1 - introduction to coastal ocean observing systems. In Yonggang Liu, Heather Kerkering, and Robert H. Weisberg, editors, *Coastal Ocean Observing Systems*, pages 1–10. Academic Press, Boston, 2015. ISBN 978-0-12-802022-7. doi: https://doi.org/10.1016/B978-0-12-802022-7.00001-8. URL `https://www.sciencedirect.com/science/article/pii/B9780128020227000018`.

[87] Zhixiang Liu, Youmin Zhang, Xiang Yu, and Chi Yuan. Unmanned surface vehicles: An overview of developments and challenges. *Annual Reviews in Control*, 41:71–93, 2016. ISSN 1367-5788. doi: https://doi.org/10.1016/j.arcontrol.2016.04.018. URL `https://www.sciencedirect.com/science/article/pii/S1367578816300219`.

[88] Robert J Livingston. *Eutrophication processes in coastal systems: origin and succession*

of plankton blooms and effects on secondary production in Gulf Coast estuaries. CRC press, 2000.

[89] Youyu Lu and Rolf G Lueck. Using a broadband adcp in a tidal channel. part i: Mean flow and shear. *Journal of Atmospheric and Oceanic Technology*, 16(11):1556–1567, 1999.

[90] Björn Lund, Hans C. Graber, H. Tamura, C. O. Collins III, and S. M. Varlamov. A new technique for the retrieval of near-surface vertical current shear from marine X-band images. *Journal of Geophysical Research: Oceans*, 120:8466–8486, 2015. doi: 10.1002/2015JC010961.

[91] Björn Lund, Brian K. Haus, Jochen Horstmann, Hans C. Graber, Ruben Carrasco, Nathan J.M. Laxague, Guillaume Novelli, Cédric M. Guigand, and Tamay M. Özgökmen. Near-surface current mapping by shipboard marine X-band radar: A validation. *Journal of Atmospheric and Oceanic Technology*, 35(5):1077–1090, 2018. ISSN 15200426. doi: 10.1175/JTECH-D-17-0154.1.

[92] Junhai Luo, Ying Han, and Liying Fan. Underwater acoustic target tracking: A review. *Sensors*, 18(1), 2018. ISSN 1424-8220. doi: 10.3390/s18010112.

[93] Jamie Macaulay, Jonathan Gordon, Douglas Gillespie, Chloë Malinka, Simon Northridge, Jamie Macaulay, Jonathan Gordon, and Douglas Gillespie. Passive acoustic methods for fine-scale tracking of harbour porpoises in tidal rapids. *The Journal of the Acoustical Society of America*, 1120, 2017. doi: 10.1121/1.4976077.

[94] Daniel G MacDonald, Louis Goodman, and Robert D Hetland. Turbulent dissipation in a near-field river plume: A comparison of control volume and microstructure observations with a numerical model. *Journal of Geophysical Research: Oceans*, 112(C7), 2007.

[95] Amala Mahadevan. The impact of submesoscale physics on primary productivity of plankton. *Annual review of marine science*, 8:161–184, 2016.

[96] P A Matthews. The Impact of Nonsynoptic Sampling on Mesoscale Oceanographic Surveys with Towed Instruments. *Journal of Atmospheric and Oceanic Technology*, 14(1):162–174, feb 1997. ISSN 0739-0572. doi: 10.1175/1520-0426(1997)014⟨0162:TIONSO⟩2.0.CO;2.

[97] Dennis A Mayer, Jyotika I Virmani, and Robert H Weisberg. Velocity comparisons from upward and downward acoustic doppler current profilers on the west florida shelf. *Journal of Atmospheric and Oceanic Technology*, 24(11):1950–1960, 2007.

[98] Katherine McCaffrey, Baylor Fox-Kemper, Peter E. Hamlington, and Jim Thomson. Characterization of turbulence anisotropy, coherence, and intermittency at a prospective tidal energy site: Observational data analysis. *Renewable Energy*, 76:441–453, 2015. ISSN 09601481. doi: 10.1016/j.renene.2014.11.063.

[99] B McGilvray and C Roman. Control system performance and efficiency for a mid-depth lagrangian profiling float. *IEEE OCEANS 2010 - SYDNEY*, 2010.

[100] Justine M. McMillan and Alex E. Hay. Spectral and structure function estimates of turbulence dissipation rates in a high-flow tidal channel using broadband adcps. *Journal of Atmospheric and Oceanic Technology*, 34(1):5 – 20, 01 Jan. 2017. doi: 10.1175/JTECH-D-16-0131.1. URL `https://journals.ametsoc.org/view/journals/atot/34/1/jtech-d-16-0131.1.xml`.

[101] Miros AS. Wavex v5.7: Product Specification, 2019. URL `https://www.miros-group.com/wp-content/uploads/2019/04/Miros-Wavex-5.7-Datasheet.pdf`.

[102] Harold O Mofjed and Lawrence H Larsen. Tides and tidal currents of the inland water of western Washington. Technical report, Pacific Marine Environmental Laboratory, Seattle, Washington, 1984.

[103] Jerry Mullison, Darryl Symonds, and Neil Trenaman. ADCP data collected from a liquid robotics Wave Glider. *2011 IEEE/OES/CWTM 10th Working Conference on Current, Waves and Turbulence Measurement, CWTM 2011*, pages 266–272, 2011. doi: 10.1109/CWTM.2011.5759563.

[104] M. Muste, K. Yu, and M. Spasojevic. Practical aspects of adcp data use for quantification of mean river flow characteristics; part i: moving-vessel measurements. *Flow Measurement and Instrumentation*, 15(1):1–16, 2004. ISSN 0955-5986. doi: https://doi.org/10.1016/j.flowmeasinst.2003.09.001.

[105] United Nations. Factsheet: People and oceans. In *The Ocean Conference*, New York, 2017.

[106] Jeff Neasham. Usmart project website. `https://research.ncl.ac.uk/usmart/`. Accessed May 2021.

[107] John Nicholas Newman. *Marine hydrodynamics*. The MIT press, 2018.

[108] NOAA. Nos hydrographic survey - h12216. bathymetric data. `https://www.ngdc.noaa.gov/nos/H12001-H14000/H12216.html`, 2010. Accessed August 4, 2020.

[109] NOAA. Tidal current predictions. pug1501 agate passage, south end; depth: 9 feet. 2020-08-19 to 2020-08-21. `https://tidesandcurrents.noaa.gov/noaacurrents/Predictions?id=PUG1501_6`, 2020. Accessed August 4, 2020.

[110] Jessica Noe. *Dynamics of an Underwater Drifting Instrument: System Modeling and Controller Design for the uFloat*. Master of mechanical engineering, University of Washington, 20202.

[111] Abdelmoumen Norrdine. An algebraic solution to the multilateration problem. In *2012 International Conference on Indoor Positioning and Indoor Navigation*, 11 2012.

[112] Jeffrey D. Paduan and Libe Washburn. High-Frequency Radar Observations of Ocean Surface Currents. *Annual Review of Marine Science*, 5(1):115–136, 2013. ISSN 1941-1405. doi: 10.1146/annurev-marine-121211-172315.

[113] Hans W. Paerl. Assessing and managing nutrient-enhanced eutrophication in estuarine and coastal waters: Interactive effects of human and climatic perturbations. *Ecological Engineering*, 26(1):40–54, 2006. ISSN 09258574. doi: 10.1016/j.ecoleng.2005.09.006.

[114] Michael Palodichuk, Brian Polagye, and Jim Thomson. Resource mapping at tidal energy sites. *IEEE Journal of Oceanic Engineering*, 38(3):433–446, 2013. ISSN 03649059. doi: 10.1109/JOE.2012.2227578.

[115] Vijay Panchang, G. Cheng, and Carter Newell. Modeling Hydrodynamics and Aquaculture Waste Transport in Coastal Maine. *Estuaries*, 20(1):14, 1997. ISSN 01608347. doi: 10.2307/1352717.

[116] B Polagye and J Thomson. Tidal energy resource characterization: methodology and field study in Admiralty Inlet, Puget Sound, WA (USA). *Proceedings of the Institution of Mechanical Engineers, Part A: Journal of Power and Energy*, 227(3):352–367, 2013. doi: 10.1177/0957650912470081.

[117] Brian Polagye and Chris Bassett. Risk to marine animals from underwater noise generated by marine renewable energy devices. In A.E. Copping and L.G. Hemery, editors, *2020 State of the Science Report: Environmental Effects of Marine Renewable Energy Development Around the World. Report for Ocean Energy Systems (OES).*, pages 66–85. OES-Environmental, 2020. doi: 10.2172/1633082.

[118] Emanuele Raggi. *Localization of a Drifting Underwater Vehicle Using a Terrain-Based Particle Filter.* PhD thesis, 2019. URL `https://search.proquest.com/dissertations-theses/localization-drifting-underwater-vehicle-using/docview/2316558056/se-2?accountid=14784`. Copyright - Database copyright

ProQuest LLC; ProQuest does not claim copyright in the individual underlying works; Last updated - 2020-11-03.

[119] Marshall Richmond, Samuel Harding, and Pedro Romero-Gomez. Numerical performance analysis of acoustic Doppler velocity profilers in the wake of an axial-flow marine hydrokinetic turbine. *International Journal of Marine Energy*, 11:50–70, 2015. ISSN 22141669. doi: 10.1016/j.ijome.2015.05.004.

[120] Stephen C Riser, Howard J Freeland, Dean Roemmich, Susan Wijffels, Ariel Troisi, Mathieu Belbeoch, Denis Gilbert, Jianping Xu, Sylvie Pouliquen, Ann Thresher, Pierre-Yves Le Traon, Guillaume Maze, Birgit Klein, M Ravichandran, Fiona Grant, Pierre-Marie Poulain, Toshio Suga, Byunghwan Lim, Andreas Sterl, Philip Sutton, Kjell-Arne Mork, Pedro Joaquin Velez-Belchi, Isabelle Ansorge, Brian King, Jon Turton, Molly Baringer, and Steven R Jayne. Fifteen years of ocean observations with the global Argo array. *Nature Clim. Change*, 6(2):145–153, 2016. ISSN 1758-678X. doi: 10.1038/nclimate2872.

[121] Chris Roman, Gabrielle Inglis, and Bryan McGilvray. Lagrangian floats as sea floor imaging platforms. *Continental Shelf Research*, 31(15):1592–1598, 2011. doi: 10.1016/j.csr.2011.06.019.

[122] T Rossby. Evolution of lagrangian methods in oceanography. *Lagrangian Analysis and Prediction of Coastal and Ocean Dynamics*, pages 1–38, 2007.

[123] T Rossby and D Webb. Observing abyssal motions by tracking swallow floats in the sofar channel. In *Deep Sea Research and Oceanographic Abstracts*, volume 17, pages 359–365. Elsevier, 1970.

[124] T Rossby, D Dorson, and J Fontaine. The rafos system. *Journal of atmospheric and oceanic technology*, 3(4):672–679, 1986.

[125] Rutter Inc. sigma S6 WaMoS II: Product Specification, 2019. URL `https://secureservercdn.net/166.62.111.84/773.24a.myftpupload.com/wp-content/themes/RutterWebsite/pdfs/sigmaS6WaMoSIISystemDescription.pdf`.

[126] Lena M Schulze Chretien and Kevin Speer. Observing plumes and overturning cells with a new coastal bottom drifter. *Journal of Atmospheric and Oceanic Technology*, 35(8):1675–1686, 2018.

[127] Alex Schwithal and Chris Roman. Development of a new Lagrangian float for studying coastal marine ecosystems. *OCEANS 2009 - Europe*, pages 1–6, 2009. doi: 10.1109/OCEANSE.2009.5278296.

[128] Brian Sellar, Gareth Wakelam, Duncan R.J. Sutherland, David M. Ingram, and Vengatesan Venugopal. Characterisation of Tidal Flows at the European Marine Energy Centre in the Absence of Ocean Waves. *Energies*, 11(1):176, 2018. ISSN 1996-1073. doi: 10.3390/en11010176.

[129] C. M. Senet, J. Seemann, and F. Ziemer. The near-surface current velocity determined from image sequences of the sea surface. *IEEE Transactions on Geoscience and Remote Sensing*, 39(3):492–505, 2001. ISSN 01962892. doi: 10.1109/36.911108.

[130] Christian M. Senet, Joerg Seemann, Stylianos Flampouris, and Friedwart Ziemer. Determination of bathymetric and current maps by the method DiSC based on the analysis of nautical X-band radar image sequences of the sea surface (November 2007). *IEEE Transactions on Geoscience and Remote Sensing*, 46(8):2267–2279, 2008. ISSN 01962892. doi: 10.1109/TGRS.2008.916474.

[131] Alexei Sentchev and Max Yaremchuk. VHF radar observations of surface currents off the northern Opal coast in the eastern English Channel. *Continental Shelf Research*, 27(19):2449–2464, 2007. ISSN 02784343. doi: 10.1016/j.csr.2007.06.010.

[132] Lynn K. Shay, Thomas M. Cook, and P. Edgar An. Submesoscale coastal ocean flows detected by very high frequency radar and autonomous underwater vehicles. *Journal of Atmospheric and Oceanic Technology*, 20(11):1583–1599, 2003. ISSN 07390572. doi: 10.1175/1520-0426(2003)020⟨1583:SCOFDB⟩2.0.CO;2.

[133] Alexander F. Shchepetkin and James C. McWilliams. The regional oceanic modeling system (ROMS): A split-explicit, free-surface, topography-following-coordinate oceanic model. *Ocean Modelling*, 9(4):347–404, 2005. ISSN 14635003. doi: 10.1016/j.ocemod.2004.08.002.

[134] Andrey Y. Shcherbina, Eric A. D'Asaro, and Sven Nylund. Observing finescale oceanic velocity structure with an autonomous nortek acoustic doppler current profiler. *Journal of Atmospheric and Oceanic Technology*, 35(2):411–427, 2018. ISSN 15200426. doi: 10.1175/JTECH-D-17-0108.1.

[135] Chengxi Shen, Weimin Huang, Eric W. Gill, Ruben Carrasco, and Jochen Horstmann. An algorithm for surface current retrieval from X-band marine radar images. *Remote Sensing*, 7(6):7753–7767, 2015. ISSN 20724292. doi: 10.3390/rs70607753.

[136] Julius Smith and Jonathan Abel. Closed-form least-squares source location estimation from range-difference measurements. *IEEE Transactions on Acoustics, Speech, and Signal Processing*, 35(12):1661–1669, 1987.

[137] Ryan N. Smith and Matthew Dunbabin. Controlled drift: an investigation into the controllability of underwater vehicles with minimal actuation. In *Proceedings of the Australasian Conference on Robotics and Automation 2011*, pages 1–10, Melbourne, VIC, Australia, 2011. Australian Robotics & Automation Assoication. ISBN 9780980740424.

[138] Ryan N. Smith and Van T. Huynh. Controlling buoyancy-driven profiling floats for applications in ocean observation. *IEEE Journal of Oceanic Engineering*, 39(3):571–586, 2014. ISSN 03649059. doi: 10.1109/JOE.2013.2261895.

[139] William Snyder, Chris Roman, and Stephen Licht. Hybrid actuation with complementary allocation for depth control of a lagrangian sea-floor imaging platform. *Journal of Field Robotics*, 35(3):330–344, 2018.

[140] Elizabeth L Steffen and Eric A D'Asaro. Deep convection in the labrador sea as observed by lagrangian floats. *Journal of Physical Oceanography*, 32(2):475–492, 2002.

[141] David A. Sutherland, Parker MacCready, Neil S. Banas, and Lucy F. Smedstad. A model study of the salish sea estuarine circulation. *Journal of Physical Oceanography*, 41(6):1125–1143, 2011. ISSN 0022-3670. doi: 10.1175/2011JPO4540.1.

[142] John C Swallow. A neutral-buoyancy float for measuring deep currents. *Deep Sea Research (1953)*, 3(1):74–81, 1955.

[143] John C Swallow. Some further deep current measurements using neutrally-buoyant floats. *Deep Sea Research (1953)*, 4:93–104, 1957.

[144] John C Swallow and LV Worthington. An observation of a deep countercurrent in the western north atlantic. *Deep Sea Research (1953)*, 8(1):1–IN3, 1955.

[145] Cilia M. Swinkels, Herman Peters, and Jos van Heesen. Analysis of Current Patterns in Coastal Areas Using X-Band Radar Images. *Coastal Engineering*, pages 1–10, 2012.

[146] Zoltan B. Szuts, Amy S. Bower, Kathleen A. Donohue, James B. Girton, Julia M. Hummon, Katsuro Katsumata, Rick Lumpkin, Peter B. Ortner, Helen E. Phillips, H. Thomas Rossby, Lynn Keith Shay, Charles Sun, and Robert E. Todd. The scientific and societal uses of global measurements of subsurface velocity. *Frontiers in Marine Science*, 6:358, 2019. ISSN 2296-7745. doi: 10.3389/fmars.2019.00358. URL `https://www.frontiersin.org/article/10.3389/fmars.2019.00358`.

[147] Hwee Pink Tan, Roee Diamant, Winston K G Seah, and Marc Waldmeyer. A survey of techniques and challenges in underwater localization. *Ocean Engineering*, 38(14-15): 1663–1676, 2011. ISSN 00298018. doi: 10.1016/j.oceaneng.2011.07.017.

[148] Longbin Tao and Daniel Dray. Hydrodynamic performance of solid and porous heave plates. *Ocean engineering*, 35(10):1006–1014, 2008.

[149] Teledyne RDI. Acoustic Doppler current profiler: Principles of operation, a practical primer., 2019.

[150] K B Theriault. Incoherent multibeam Doppler current profiler performance: Part II - Spatial Response. *IEEE Journal of Oceanic Engineering*, OE-11(1):7–15, 1986. ISSN 03649059. doi: 10.1109/JOE.1986.1145146.

[151] Maxime Thiébaut, Jean-François Filipot, Christophe Maisondieu, Guillaume Damblans, Christian Jochum, Levi F Kilcher, and Sylvain Guillou. Characterization of the vertical evolution of the three-dimensional turbulence for fatigue design of tidal turbines. *Philosophical Transactions of the Royal Society A*, 378(2178):20190495, 2020.

[152] D. J. M. Thomson, S. E. Dosso, and D. R. Barclay. Modeling auv localization error in a long baseline acoustic positioning system. *IEEE Journal of Oceanic Engineering*, 43 (4):955–968, 2018. doi: 10.1109/JOE.2017.2771898.

[153] J. Thomson, B. Polagye, V. Durgesh, and M. C. Richmond. Measurements of Turbulence at Two Tidal Energy Sites in Puget Sound, WA. *IEEE Journal of Oceanic Engineering*, 37(3):363–374, jul 2012. ISSN 0364-9059. doi: 10.1109/JOE.2012.2191656.

[154] J. Thomson, M. Moulton, A. de Klerk, J. Talbert, M. Guerra, S. Kastner, M. Smith, M. Schwendeman, S. Zippel, and S. Nylund. A new version of the swift platform for waves, currents, and turbulence in the ocean surface layer. In *IEEE/OES Workshop on Currents, Waves, and Turbulence Measurements*, March 2019.

[155] Jim Thomson. Wave breaking dissipation observed with SWIFT drifters. *Journal of Atmospheric and Oceanic Technology*, 29(12):1866–1882, 2013/01/03 2012.

[156] Kristen M. Thyng. *Numerical Simulation of Admiralty Inlet, WA, with Tidal Hydrokinetic Turbine Siting Application.* Doctor of philosophy, University of Washington, 2012.

[157] Kristen M. Thyng. Output data from 'numerical simulation of admiralty inlet, wa with tidal hydrokinetic turbine siting application'. `http://pong.tamu.edu/~kthyng/froude/ai65/OUT/`, 2012. last accessed August 8, 2019.

[158] Kristen M. Thyng, James J. Riley, and Jim Thomson. Inference of turbulence parameters from a ROMS simulation using the k-ϵ closure scheme. *Ocean Modelling*, 72: 104–118, 2013. ISSN 14635003. doi: 10.1016/j.ocemod.2013.08.008.

[159] Robert E. Todd, Daniel L. Rudnick, Jeffrey T. Sherman, W. Brechner Owens, and Lawrence George. Absolute velocity estimates from autonomous underwater gliders equipped with doppler current profilers. *Journal of Atmospheric and Oceanic Technology*, 34(2):309–333, 2017. ISSN 15200426. doi: 10.1175/JTECH-D-16-0156.1.

[160] M Toner, A C Poje, A D Kirwan, CKRT Jones, B L Lipphardt, and C E Grosch. Reconstructing Basin-Scale Eulerian Velocity Fields from Simulated Drifter Data. *Journal of Physical Oceanography*, 31:1361–1376, 2001. ISSN 1520-0485. doi: 10.1175/1520-0485(2001)031⟨1361:RBSEVF⟩2.0.CO;2.

[161] D. W. Velasco and Sven Nylund. Performance improvement for adcps on surface buoys. In *2019 IEEE/OES Twelfth Current, Waves and Turbulence Measurement (CWTM)*, pages 1–7, Feb 2019.

[162] Ross Vennell. Acoustic Doppler Current Profiler measurements of tidal phase and Amplitude in Cook Strait, New Zealand. *Continental Shelf Research*, 14(4):353–364, 1994.

[163] Taiping Wang and Zhaoqing Yang. A modeling study of tidal energy extraction and

the associated impact on tidal circulation in a multi-inlet bay system of puget sound. *Renewable Energy*, 114:204–214, 2017.

[164] John Wilkin, Leslie Rosenfeld, Arthur Allen, Rebecca Baltes, Antonio Baptista, Ruoying He, Patrick Hogan, Alexander Kurapov, Avichal Mehra, Josie Quintrell, et al. Advancing coastal ocean modelling, analysis, and prediction for the us integrated ocean observing system. *Journal of Operational Oceanography*, 10(2):115–126, 2017.

[165] J. Scott Willcox, James G. Bellingham, Yanwu Zhang, and Arthur B. Baggeroer. Performance metrics for oceanographic surveys with autonomous underwater vehicles. *IEEE Journal of Oceanic Engineering*, 26(4):711–725, 2001. ISSN 03649059. doi: 10.1109/48.972114.

[166] Ben Wilson, Steven Benjamins, and Jim Elliott. Using drifting passive echolocation loggers to study harbour porpoises in tidal-stream habitats. *Endangered Species Research*, 22(2):125–143, Dec 2013. ISSN 1863-5407. doi: 10.3354/esr00538. URL `http://www.int-res.com/abstracts/esr/v22/n2/p125-143/`.

[167] J Wolf and D Prandle. Some observations of wave–current interaction. *Coastal Engineering*, 37(3):471 – 485, 1999. ISSN 0378-3839. doi: https://doi.org/10.1016/S0378-3839(99)00039-3.

[168] Annie PS Wong, Susan E Wijffels, Stephen C Riser, Sylvie Pouliquen, Shigeki Hosoda, Dean Roemmich, John Gilson, Gregory C Johnson, Kim Martini, David J Murphy, et al. Argo data 1999–2019: Two million temperature-salinity profiles and subsurface velocity observations from a global array of profiling floats. *Frontiers in Marine Science*, 2020.

[169] I. R. Young, W. Rosenthal, and F. Ziemer. A three-dimensional analysis of marine radar images for the determination of ocean wave directionality and surface currents.

Journal of Geophysical Research, 90:1049–1059, 1985. ISSN 0148-0227. doi: 10.1029/JC090iC01p01049.

Appendix A

DERIVATION OF BUOYANCY-CONTROLLED FLOAT DYNAMICS

In the following derivations, f subscript indicates float properties, while w subscript indicates water properties. Consider the momentum balance on a volume of fluid V_{CV} moving through a domain,

$$\frac{\mathrm{d}}{\mathrm{d}t}\int_{V_{CV}} \boldsymbol{U}\rho \,\mathrm{d}V + \int_{S_{CV}} \boldsymbol{U}\rho(\boldsymbol{U}\cdot\hat{n})\,\mathrm{d}S = \sum F_{external,CV}. \tag{A.1}$$

That is, the time rate of change ($\frac{\mathrm{d}}{\mathrm{d}t}$) of momentum (velocity $\mathbf{U}$ times density ρ) of the fluid inside the control volume V_{CV} plus the momentum flux $\mathbf{U}\rho(\mathbf{U}\cdot\hat{n})$ through the surface bounding the control volume S_{CV} is equal to the sum of the external forces.

The external forces acting on the fluid volume are a sum of gravity, pressure, and viscous shear stresses

$$\sum F_{external,CV} = -\hat{\boldsymbol{g}}\int_{V_{CV}} \rho \,\mathrm{d}V + \int_{S_{CV}} (p\cdot\hat{\boldsymbol{n}})\mathrm{d}S + \int_{S_{CV}} \boldsymbol{\tau}\hat{n}\,\mathrm{d}S \tag{A.2}$$

where $\hat{\boldsymbol{g}}$ is acceleration due to gravity, acting in the downward direction, p is pressure, and $\boldsymbol{\tau}$ is the viscous stress tensor.

An underwater float will experience a similar momentum balance. First, we define the control volume V_{CV} in the previous expressions as the float volume. Given the hard boundaries of the float, there can be no momentum flux through the exterior surface of the float and the entire object must be moving at the same velocity $\boldsymbol{U_f}$. Additionally, the integrated mass of the float, $m_f = \int_{V_{CV}} \rho_f \mathrm{d}V$, does not change. Rewriting Eqs. A.1 and A.2 for the float under these assumptions gives

$$m_f \frac{\mathrm{d}U_f}{\mathrm{d}t} = -\hat{\boldsymbol{g}} m_f + \int_{S_{CV}} (p \cdot \hat{\boldsymbol{n}}\,)\mathrm{d}S + \int_{S_{CV}} \boldsymbol{\tau} \hat{n}\,\mathrm{d}S \tag{A.3}$$

Let us now examine the forces contributing to the right hand side. Through the following steps, we will decompose the normal and shear stresses (p and $\boldsymbol{\tau}$) into their constituent parts. For simplicity of notation, we will retain p and $\boldsymbol{\tau}$ to notate remaining unidentified forces as we progress through the derivation.

First, consider the case when both float and water are at rest. The pressure field experienced by the float is due entirely to hydrostatic pressure $p(z) = \hat{\boldsymbol{g}}\rho_w z$, where z is depth underwater. When fully submerged mid-water column, evaluating the hydrostatic pressure field over the float produces the familiar buoyancy term [85],

$$\int_{S_{CV}} (\hat{\boldsymbol{g}}\rho_w z \cdot \hat{\boldsymbol{n}})\mathrm{d}S = \hat{\boldsymbol{g}}\rho_w V_f \tag{A.4}$$

Thus, Eq. A.3 becomes

$$m_f \frac{\mathrm{d}U_f}{\mathrm{d}t} = -\hat{\boldsymbol{g}} m_f + \hat{\boldsymbol{g}}\rho_w V_f + \int_{S_{CV}} (p \cdot \hat{\boldsymbol{n}}\,)\mathrm{d}S + \int_{S_{CV}} \boldsymbol{\tau} \hat{n}\,\mathrm{d}S \tag{A.5}$$

Also, note that the hydrostatic pressure produces no shear forces.

Next, we will temporarily ignore the water viscosity and assume also the float is pinned in place, such that its velocity is zero. Let us first consider the case of perfectly steady, irrotational fluid flow (i.e., potential flow), uniform across the region surrounding the float. In the absence of friction, such a condition produces zero force on the float (a paradox posited by D'Alembert). However, acceleration of the float or the water does generate a force. Consider the case of still water through which the float accelerates (by some hypothetical external force). Given the water cannot move through the float, the float must accelerate the surrounding water. As this force is akin to the float having additional inertia, it is commonly termed 'added mass'. This added mass m_a can be solved analytically for simple geometries, such as spheres, ellipses, and cylinders [107], but here we take the general form

$$\boldsymbol{F_{m_a}} = -\frac{\mathrm{d}\boldsymbol{U_f}}{\mathrm{d}t}\boldsymbol{m_a} \tag{A.6}$$

where the added mass m_a is particular to the float geometry. Added mass for more complicated geometries may be found in [107].

Considering the inverse situation, in which the float is stationary and water accelerates, the previously described added mass term must again exist, as the flow is accelerated around the float. However, the float will experience an additional 'buoyancy-like' term. To conceptualize this, consider the example of a horizontally accelerating flow. In such conditions (regardless of the presence of the float), a pressure gradient opposite the direction of flow must exist. As such, similar to buoyancy produced by the hydrostatic pressure gradient, this flow-generating horizontal pressure field generates a force on the float equal to volume of displaced water times the pressure gradient $V_f \nabla p$. Given that for an inviscid fluid with constant density $\frac{\mathrm{D}\boldsymbol{U}}{\mathrm{D}t} = \frac{1}{\rho_w}\nabla p$ (Euler's equation), the combined force on the float in this case is

$$\boldsymbol{F_{m_a}} = \frac{\mathrm{D}\boldsymbol{U}}{\mathrm{D}t}(\rho_w V_f + \boldsymbol{m_a}) \tag{A.7}$$

as is discussed in [70].

In the case of an accelerating body and an accelerating flow, the two forces can be combined, giving

$$\boldsymbol{F_{m_a}} = \frac{\mathrm{D}\boldsymbol{U}}{\mathrm{D}t}(\rho_w V_f + \boldsymbol{m_a}) - \frac{\mathrm{d}\boldsymbol{U_f}}{\mathrm{d}t}\boldsymbol{m_a} \tag{A.8}$$

Note that superposition should be applicable here, as both terms are derived in the framework of potential flow. A subtle complication arises when we consider that the float is generally moving with the surrounding water. In this case, the 'buoyancy-like' term in

Eq. A.7 is modified according to the relative velocity between the float and water [107]. However, from the perspective of understanding the dynamics of the float in the context of design, this subtlety of the potential flow description is less critical than the overall impact of added mass on float behavior. The key elements to consider are:

1. An accelerating float must accelerate the fluid around it. This ‘added mass’ will depend on the geometry of the float and the direction of acceleration.

2. If flow accelerations (pressure gradients) have length scales such that they can considered uniform over the region containing the float, they may be considered ‘far-field’ and will always act to accelerate the float and added mass along with the surrounding flow. The size of the float thus determines the degree to which the float is correspondingly ‘Lagrangian.’ For this reason, a perfectly flow-following float would need to be of the same scale as the Taylor microstructure (smallest turbulent length scale).

3. Flow variations on length scales proportional to the float size (e.g., from turbulence, shear flow) may induce additional behaviors that are not considered here, such as rotation.

Including A.8 in A.5 gives

$$(m_f + \boldsymbol{m_a})\frac{\mathrm{d}\boldsymbol{U_f}}{\mathrm{d}t} = -\hat{\boldsymbol{g}}m_f + \hat{\boldsymbol{g}}\rho_w V_f + (\rho_w V_f + \boldsymbol{m_a})\frac{\mathrm{D}\boldsymbol{U}}{\mathrm{D}t} + \int_{S_{CV}} (p \cdot \hat{\boldsymbol{n}})\,\mathrm{d}S + \int_{S_{CV}} \boldsymbol{\tau}\hat{n}\,\mathrm{d}S \quad \text{(A.9)}$$

Lastly, we will consider the impact of viscosity. When there is a relative velocity between the float and surrounding water, a boundary layer develops between the float and surrounding flow. This produces viscous stresses along the surface of the float and a non-uniform pressure field over the float body. The resulting hydrodynamic force is typically decomposed into drag and lift components which are parallel and perpendicular (respectively) to the direction of the incoming flow. Given that relative velocities remain low and float geometries are typically symmetrical, we ignore lift. The dynamics governing drag are complex, but by dimensional analysis [107], the quadratic drag equation can be parameterized as

$$\boldsymbol{F_d} = -\frac{1}{2}\rho_w \boldsymbol{C_d} \boldsymbol{A} \boldsymbol{U_{rel}^2} \tag{A.10}$$

where $\boldsymbol{A}$ is the cross-sectional area of the float, $\boldsymbol{U_{rel}} = \boldsymbol{U_w} - \boldsymbol{U_f}$ is the relative velocity, and ρ_w is the density of the water. Note the negative sign is included as drag always acts opposite the direction of relative motion. Lastly, the coefficient $\boldsymbol{C_d}$ is a function of float geometry and Reynolds number, determined empirically. The effect of drag is to reduce relative motion between the float and surrounding water, which is desired for a flow-following float. This can be achieved through increasing surface roughness or adding sails or fins, with the caveat that this may also increase the inertia due to added mass. A porous surface can provide a more favorable ratio of drag to inertia than a solid one [148].

Adding drag to Eq. A.9, we reach the dynamic expression presented in Chapter 3 (Eq. 3.2).

$$(m_f + \boldsymbol{m_a})\frac{\mathrm{d}\boldsymbol{U_f}}{\mathrm{d}t} = -\hat{\boldsymbol{g}} m_f + \hat{\boldsymbol{g}} \rho_w V_f - \frac{1}{2}\rho_w \boldsymbol{C_d} \boldsymbol{A} \boldsymbol{U_{rel}^2} + (\rho_w V_f + \boldsymbol{m_a})\frac{\mathrm{D}\boldsymbol{U}}{\mathrm{D}t} \tag{A.11}$$

Note that in this derivation, we ignored rotational motion of the float. Floats, including the μFloat, are typically designed with the center of mass well below the center of buoyancy, such that the vertical orientation is passively maintained. This ensures that recovery antennas are facing skyward when surfacing. Design of a float that could directly measure flow shear and vorticity along horizontal (x,y) axes would require co-locating the center of mass and pressure. Rotations around the vertical (z) axis are possible and are observed on the μFloat when the buoyancy engine motor accelerates due to conservation of angular momentum. While this could theoretically induce lift (per Kutta-Joukowki theorem [75]), the observed rotational velocities are relatively slow due to viscous skin drag and because the direction of motor actuation changes frequently during depth-holding control. As such, we may reasonably neglect contributions from this phenomena. If found to be problematic, vertical drag surfaces (fins) could be added to increase viscous drag and counter the rotational motion. Additionally, we have assumed contribution from viscous boundary layer acceleration (Basset force [75]) is negligible.

Appendix B

HYDROPHONE PROCESSING

Figure 4.9 presents data from an OceanSonics icListen hydrophone externally mounted on a μFloat during Lake Washington testing. The hydrophone was set to record continuous waveform data, with 102.4 kHz bandwidth (256k Hz sample rate) and raw voltage levels from +3 to -3 V. In post-processing, we first converted recorded voltage to pressure. This conversion was performed in frequency space and based on frequency-dependent transducer sensitivity. To time-align the hydrophone time series to the corresponding μFloat data records – most critically, the nanomodem – we manually reviewed the time series to align motor movement with sharp increases in acoustic noise in the 0-3 kHz frequency band. The shift time, a consequence of hydrophone clock drift, was found to be 7.8 s.

From the time series of acoustic pressure, three metrics were extracted: (1) a broadband spectrogram; (2) the ambient sound pressure level (SPL) in the acoustic nanomodem communication frequency band; and (3) the SPL of acoustic nanomodem pings received by the hydrophone. The specifics for calculating each are described in the following sections.

B.0.1 Broadband Spectrogram

The spectrogram included in Figure 4.9 is composed of a time-series of median power spectral density (PSD) periodograms. Hydrophone data was recorded in one-minute files. For each file, we computed a high-resolution spectrogram by application of a Short Time Fast Fourier Transform (FFT) with Hamming window with a width of 2^{15} samples (0.128 s) and 50% overlap. The resulting spectrogram is 2^{15} frequency bands (3.125 Hz resolution) by 938 time steps (0.128 s resolution). For each 20-second segment (156 time-steps), we compute the median PSD at each frequency band, thus producing the ambient PSD periodogram for that

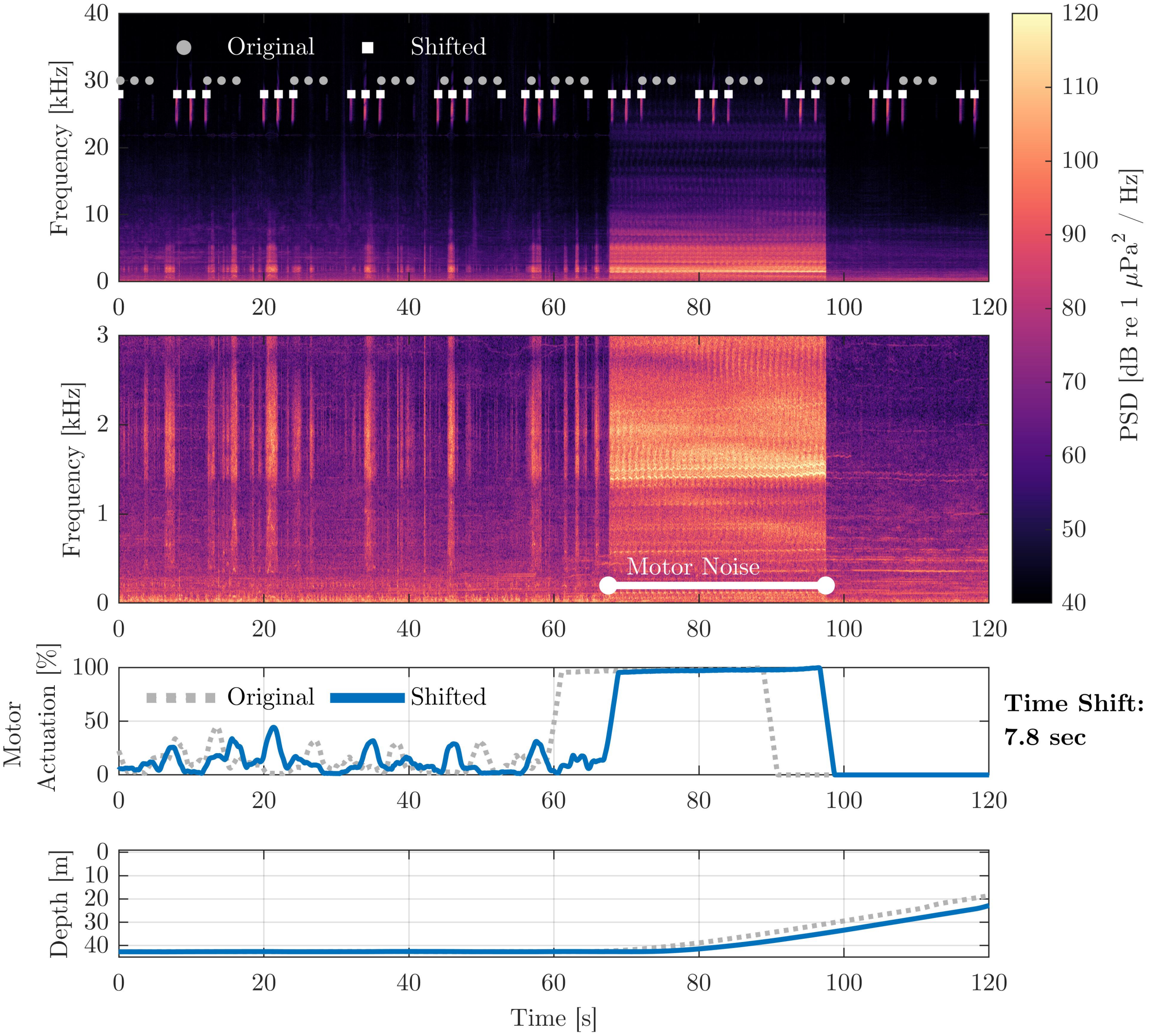

Figure B.1: Temporally aligning hydrophone data μFloat data (for μFloat 27). Upper two panels are spectrograms from hydrophone data. The upper-middle panel highlights 0-3 kHz frequency band, where motor noise is most pronounced, allowing alignment with motor actuation (lower-middle). Float depth (bottom) is shown for reference. The recorded nanomodem ping time stamps are overlaid on the hydrophone spectrogram (top panel). Note the ping indicators (circles and squares) are plotted near the 24-28 kHz nanomodem transmission band, but the y-values are arbitrary and offset vertically for clarity between original and shifted data.

20-second time step.

B.0.2 Ambient Sound Pressure Level (SPL) in Transmission Band

Nanomodem transmissions occur in the 24-28 kHz frequency band. To compute the ambient SPL in the transmission band, we apply an 8th-order bandpass Butterworth filter with 24-28 kHz pass band and 23-29 kHz stop band with 20 dB attenuation. As the time-resolution provided by the hydrophone is significantly higher than that required to resolve the transmission band, we subsequently downsample the band-passed time-series of pressure to decrease processing time. The downsample factor was determined by comparing the subsequently calculated metrics as produced by the full-resolution data against metric calculated from data downsampled by factors of 2,4,8,16, and 32. The comparison was performed over a trial set of data that included both periods of low and high ambient noise. The factor chosen (8) showed no appreciable change in the resulting metrics while decreasing processing time by a factor of 40.

Once the time-series was band-passed and down-sampled, the time-varying ambient noise level in the transmission band was computed as the median absolute pressure level at each 12-second interval (no overlap). Root-mean-square values were considered for this metric, however, the result was strongly biased by the nanomodem pings, and thus not suitable for representing ambient noise. Ambient SPL was then calculated as $20\log_{10}(P_{med}/1\mu\text{Pa})$.

B.0.3 Ping Receive SPL

To extract the ping receive levels from band-passed, down-sampled pressure series, we applied the same match filter that the nanomodem uses to identify incoming pings. To do so, we generated a template of the nanomodem chirp waveform (a 0.05-second preamble present on all nanomodem messages), then cross-correlate the template and pressure-time series. Times when the correlation surpassed a threshold of 0.25 were considered valid ping events. Note this is the same threshold used in the nanomodems to initiate decoding of the incoming pressure series.

Having located the pings, we computed the root-mean-square pressure level over the ping duration (0.275 seconds). The received SPL was calculated as $20\log_{10}(P_{rms}/1\mu\text{Pa})$. Finally, we labeled the hydrophone-recorded pings according to their source nanomodem by appeal to the known ping schedule, following the same process used to correct corrupted nanomodem records.

Appendix C

LOCALIZATION PROCESSING

The following section elaborates on the nanomodem post-processing steps outlined in Section 3.6.

C.1 Correcting for Mislabeled Nanomodem Messages

Nanomodem pings were broadcast from SLBs and recorded on all nanomodems within range (i.e., both nanomodems on SLBs and μFloats). The nanomodem ping encoded the message type and a unique numeric code associated with the source. For example, **#P242** indicates a ping (**#P**) from SLB 2 (**242**). Numeric codes were limited to 241-245, corresponding to SLBs 1-5. While the nanomodems are able to send and receive message types other than pings that offer additional functionality (e.g., broadcast, unicast), these were not utilized.

Nanomodem pings were subject to corruption during transmission. This corruption sometimes resulted in lost messages, as the receiving nanomodem did not recognize the distorted incoming waveform. Among the pings that were recorded, many messages exhibited incorrect numeric codes, typically one or two flipped bits relative to the correct value. Comparing data from four hydrophones deployed on μFloats during Lake Washington testing, we observed that increased rates of corruption occurred at lower SNR (Fig. D.1). Thus, we hypothesise that multipathing and low acoustic SNR are the likely causes of corrupt receptions. The low SNR can result from high ambient noise levels, or attenuation of the source due to absorption and spreading, as well as losses associated with reflection and scattering at boundaries.

Two types of corrupted messages were considered for correction: (1) messages received from invalid addresses (e.g., a ping from any numeric code other than 241-245); (2) messages received from a valid address (241-245), but at an implausible time-delay relative to the known ping schedule. Additionally, the ‘ping’ functionality is built in a send-receive fashion, such that if a nanomodem receives a ping with a label corresponding to its own ID, it issues a response ping. Thus, it is possible, but extremely unlikely, that a sent ping could be corrupted such that the received message matches the receiver ID, resulting in a valid ping broadcast from that receiver. Given the low probability of this event, it was not considered in the cleaning process and may have resulted in some small percentage of erroneous messages.

To correct corrupted messages, we perform the following steps:

1. Compile all received messages on a given receiver and sort chronologically.
2. Compute the approximate distance between all possible sources and the given receiver. For float positions, interpolated GPS data from times at the surface were used to estimate distance. Depending on flow conditions, this estimate may be off by a few hundred meters.
3. Compute estimated message travel time, given the approximate distances and average sound velocity (measured). Given sound speeds of 1450-1500 m/s and an assumed maximum distance error of 300 m, the corresponding error in estimated time of flight is 0.2 s at maximum. This is much smaller than the ping separation time in both Lake Washington (2 s) and Agate Pass (1 s).
4. Compute the estimated send time by subtracting the estimated travel times from the recorded receive time. This results in an approximate send time for each SLB for a single given ping.
5. Based on the known ping schedule for each SLB, assign the numeric code associated with the SLB that is the most likely source for the given recorded ping.

This process is performed over all pings in the record. For those pings which were received correctly, the process returns the original address. Those pings which were received from invalid addresses, as well as those with valid but incorrect addresses, are corrected by this procedure. Pings could theoretically align with more than one valid source due to variable source-receiver distances. However, this would require acoustic transmission times greater than the ping separation time, which correspond to transmission distances greater than 3000 m in Lake Washington and 1500 m in Agate Pass, neither of which occurred. As such, all pings recorded during Lake Washington and Agate Pass were uniquely labeled by this process.

C.2 Geometric Correction of Reflected Acoustic Paths

During testing on Lake Washington, we observed clear evidence of bottom-reflections, likely resulting from downward refraction of the propagating sound wave due to the strong thermocline and corresponding sound speed gradient. Examining the acoustically derived distances between SLBs, we observed step changes in these distances, as if alternating between two discrete distances (Fig. C.1, raw data). Comparing the acoustic distance estimates against distances calculated from GPS data for the SLBs revealed a clear bi-modal trend. During Test 1, the longer acoustic distances matched path lengths for sounds reflecting off a nominal bottom depth of 60 m (Fig. C.2).

To correct for reflections on both SLB and μFloat data, we used a simplified geometric model for ray propagation to calculate the estimated horizontal distance L_h from the measured acoustic path length L_a. As pictured in Figure C.3, the downward-refracted sound would follow a curved path (red) that prevents reception of direct transmission to distant floats and SLBs. To simplify, we assumed the acoustic path L_a followed straight trajectories with a single reflection off the bottom (dashed grey). Combining this with an estimated nominal depth Z, along with the known source depth z_s and receiver depth z_r, we can compute horizontal distance L_h as

$$L_h = \sqrt{{L_a}^2 - (2Z - z_s - z_r)^2} \tag{C.1}$$

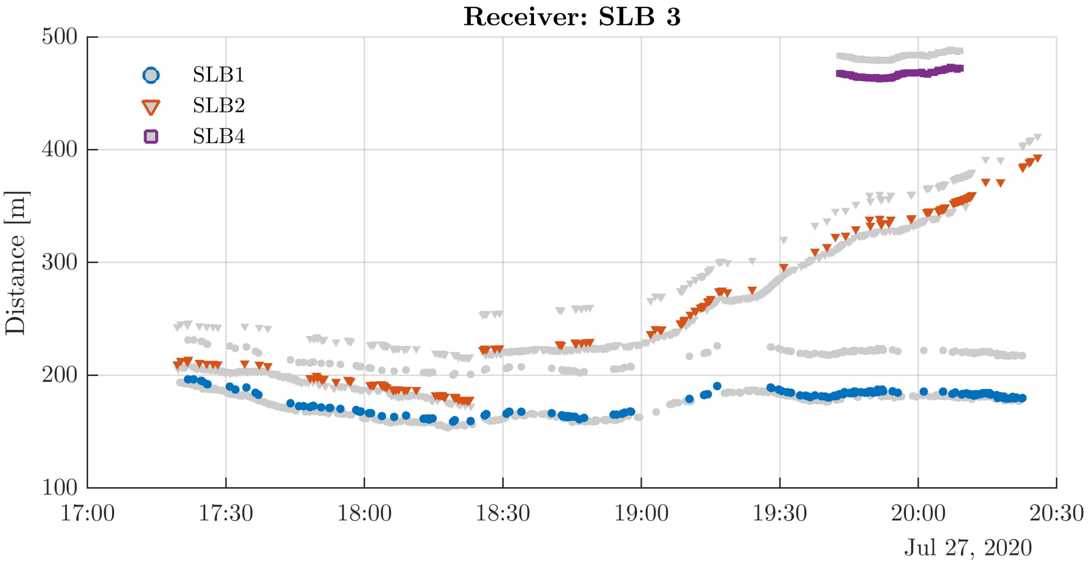

Figure C.1: Time series of distance between source SLBs 1, 2, and 4 and receiver SLB 3 during Lake Washington - Test 1, estimated from ping travel times. Raw data, in grey, includes discrete jumps between distances. Colored data has been corrected assuming a single bottom reflection. Note that SLB 2 was manually moved at 19:25, and SLB 4 was manually moved within 500 m at 19:45.

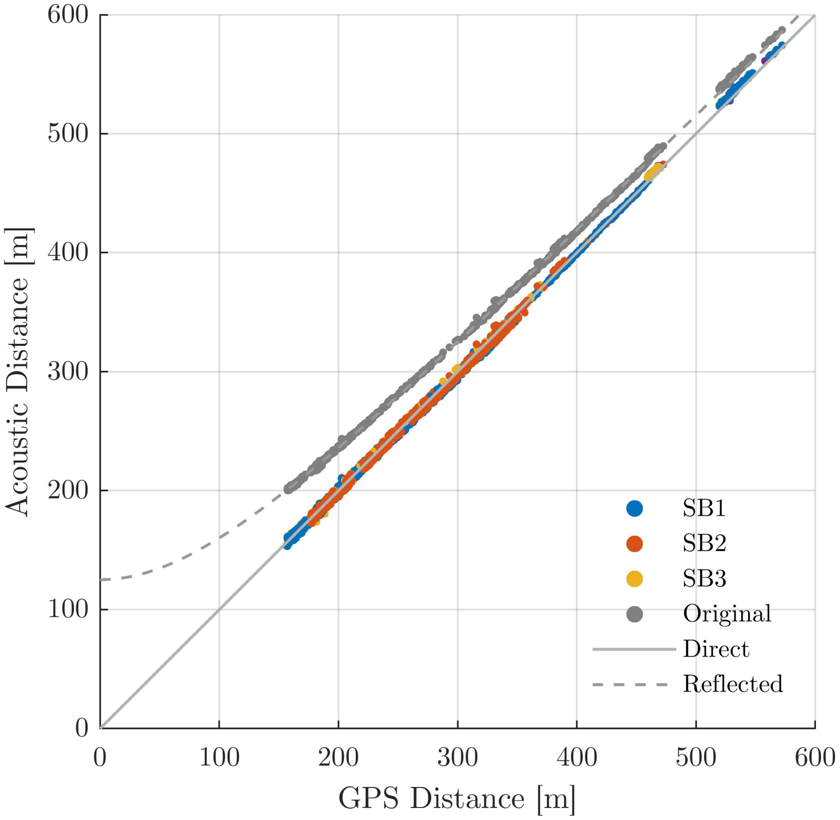

Figure C.2: Acoustic vs. GPS estimated separation distance for all SLBs during Lake Washington - Test 1. Solid line indicates equality between acoustic and GPS estimates, expected for direct paths. Dashed line indicates expected acoustic path length that includes a single bottom reflection assuming a 60 m nominal depth. Grey points are the original data and colored are the corrected values.

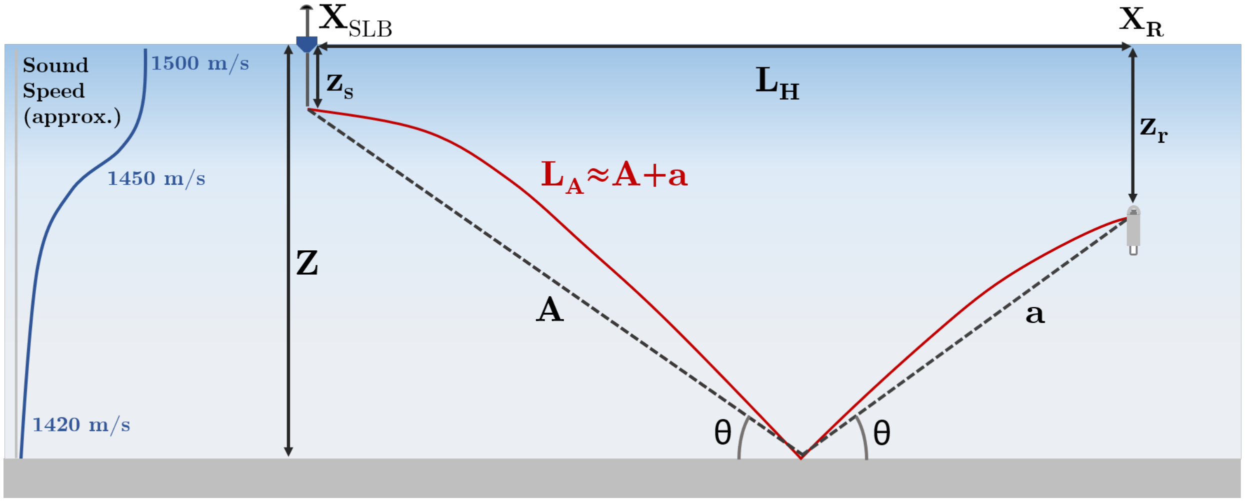

Figure C.3: Geometric treatment of reflected acoustic path length L_a to extract horizontal distance L_h based on known source depth z_s, receiver depth z_r, and an a nominal site depth Z. The sound speed gradient caused downward refraction of the nanomodem messages, resulting in reflected paths.

Note that for corrections during Tests 1 and 2 on Lake Washington were processed independently, as the nominal depths were different. For Agate Pass, no reflections were observed, though because the channel is shallow (10 m), the direct and reflected paths are equal to within 5 m beyond 40 m horizontal distance.

Localization accuracy assessments performed in 4.3.3 compared results based on the raw acoustic distance measurements and those were corrected for suspected bottom reflections. To identify and subsequently correct those pings with suspected bottom reflections, we computed the horizontal distance for all pings, assuming all pings followed the reflected path for all pings. We then compared both raw acoustic path and reflected path estimate to the GPS-estimated separation distance. The pings for which the reflected path was closer were labeled as 'reflected' and assigned the corrected horizontal distance. Because this procedure relies on knowledge of the actual path lengths, it is not a practical solution for robustly improving accuracy of μFloat localizations. However, performing this analysis on the SLBs was valuable as it provided insight on the degree to which unfavorable environmental conditions may degrade localization accuracy.

Reflections were strongly evident in the Lake Washington data, suspected on about 60% of SLB receptions during both tests (Table D.1). For the μFloats, the overall percentage is significantly lower than on the SLBs. The proportional time floats spent near the surface during LW-2 was higher than during LW-1, which likely caused the increase in suspected reflections during Test 2. In Agate Pass, reflected paths were either absent, which is possible given the lack of strong sound speed gradient, or path lengths were negligibly different due the shallow nature of the channel (10 m) relative to transmission distances (generally $>$ 100 m).

C.2.1 Cleaning and Smoothing Float Trajectories

Despite the previous steps taken to clean nanomodem transmissions and improve distance estimates, the resulting trilatered float and SLB positions were still noisy, gappy, and implied physically unrealistic trajectories. Two steps were taken to improve the overall trajectories.

First, obviously incorrect localizations were removed. For Lake Washington, currents were assumed to be less than 0.1 m/s and underwater periods less than 30 minutes, so localizations greater than 200 m away from the approximate locations (determined by interpolating GPS data from surface periods) were excluded. For Agate Pass, where currents were stronger, only points that were on land were excluded. Once these obvious outliers were removed, we smoothed the remaining positions, producing the final estimates of float trajectories. To generate these trajectories, we combined acoustic estimates with GPS data gathered prior to diving and after surfacing. For the profiling Agate Pass deployments, in which the floats regularly surfaced, all the GPS and acoustic position estimates for a given survey were combined into a single time series prior to smoothing. When building tracks to evaluate localization accuracy based on SLB data, we only include one minute of SLB GPS data on either end of the evaluation period, where the evaluation periods were defined by discrete in-water deployment periods for the SLBs (10 minutes at minimum in Lake Washington, 20 minute deployments in Agate Pass). While many smoothing methods were tested, we determined that a robust (outlier-rejecting) locally-weighted quadratic regression (MATLAB 'smooth' function with 'rloess' option) provided the optimal balance of maintaining high-frequency information, while overcoming the gappy nature of the position data. As the smoothing window size determines the smallest spatial and temporal features resolved in float data, we sought to minimize the smoothing window size. However, given the variably sized gaps in the data, the window needed to be large enough to include a representative sample of the data series. Additionally, the window for this smoothing technique operates over samples, rather than time. To ensure consistent window time span, the position data was mapped to a uniform time vector with 1 second resolution. Time steps without position data were filled with NaN values and thus did not contribute to the smoothing regression. Window size was initialized at 60 samples (1 minute) and increased by steps of 30 samples until either 60% of the windows included at least 10 data points or a window size of 240 samples (4 minutes) was reached. The smoothing operation was performed on x and y data separately using identical window size. In Lake Washington, the smoothing windows used 60-90 samples. In Agate Pass, windows ranged from 60-240 samples.

Appendix D

NANOMODEM CONNECTIVITY

Table D.1 displays the overall nanomodem connectivity statistics for the SLBs and μFloats during the two Lake Washington tests and Agate Pass test (F3) that are discussed in Chapter 4. For context, Figure D.1 shows how connectivity, corruption, and reflection rates change with SNR during the Lake Washington deployment, as computed from the four floats that were equipped with external hydrophones. Figure D.2 provides connectivity, corruption, reflection and SNR of nanomodem pings in Lake Washington as a function depth and distance, while Figure D.3 depicts receptions and corruptions during the Agate Pass tests. These latter two figures include both μFloat and SLB nanomodem records for the given test.

Receptions for the SLBs are lowest during LW-1 because SLBs 4 and 5 spent the majority of the test quite distant ($>$ 750 m) from the other three floats. This improves dramatically during LW-2, as all SLBs are placed within 200 m of each other and the floats. The μFloat connectivity matches this trend for the same reasons, however the overall percentages are significantly higher than on SLBs, due to the thermocline favoring targets at depth. For both platforms, overall connectivity in Agate Pass falls roughly between the two Lake Washington tests. This follows the trend of source-receiver distance dominating connectivity effects, as the average separation distance during Agate Pass ($\sim$ 350 m) split the two Lake Washington deployments (500 m and 150 m).

Overall, the number of corrupted, received messages are higher on the SLBs than the μFloats, likely due to their shallow depth. Due to the percentage of corruptions occurring at relatively high SNR ($\sim$ 10 dB) (Fig. D.1), we hypothesize that multipath interference is the likely cause. Interestingly, corruption rates observed in Agate Pass decrease on SLBs and increase on the μFloats relative to corruption rates in Lake Washington. The decrease in

Table D.1: Overall Nanomodem Connectivity. Percentage received is relative to total sent. Percentage corrupted and reflected are both relative to the number of received messages.

		Sent	Received	%	Corrupted	%	Reflected	%
LW - 1	SLB	15 190	4788	32 %	1485	31 %	2744	57 %
	μF	45 855	27 672	61 %	750	3 %	3538	9 %
LW - 2	SLB	3041	1950	64 %	615	32 %	1259	65 %
	μF	2982	2695	90 %	98	4 %	448	17 %
Agate Pass	SLB	4817	2160	45 %	343	16 %	0	0 %
	μF	13 812	7618	55 %	469	6 %	0	0 %

corruptions of the SLBs during the Agate Pass test is likely due to a higher overall SNR, as the SLBs remained closer together (within 500 m) during the deployment and messages did not suffer from acoustic refraction. For the μFloats, the increase in corruptions is possibly due to higher ambient noise relative to Lake Washington tests, increased multipathing interference, as well as increased self-noise from the μFloat motor. The motors ran more frequently and at greater speeds during the Agate Pass tests as the μFloats attempted to maintain depth in the presence of vertical turbulence, thus increasing their self-noise.

As noted in Section 4.4.1, it is important to stress that the ‘v2’ nanomodems have already become outdated. The v2 ping message is a crude packet with no error correction or detection and is not ideal for this application. The new ‘v3’ nanomodems have shorter ping messages (about 100 ms vs 275 ms) and are significantly more robust due to improved error correction. Thus, a short data message of a few bytes on the V3 would be about the same length as a v2 ping but protected by strong error correction and detection. Thus, corrupted packets should occur less than 1 in 10^6 messages.

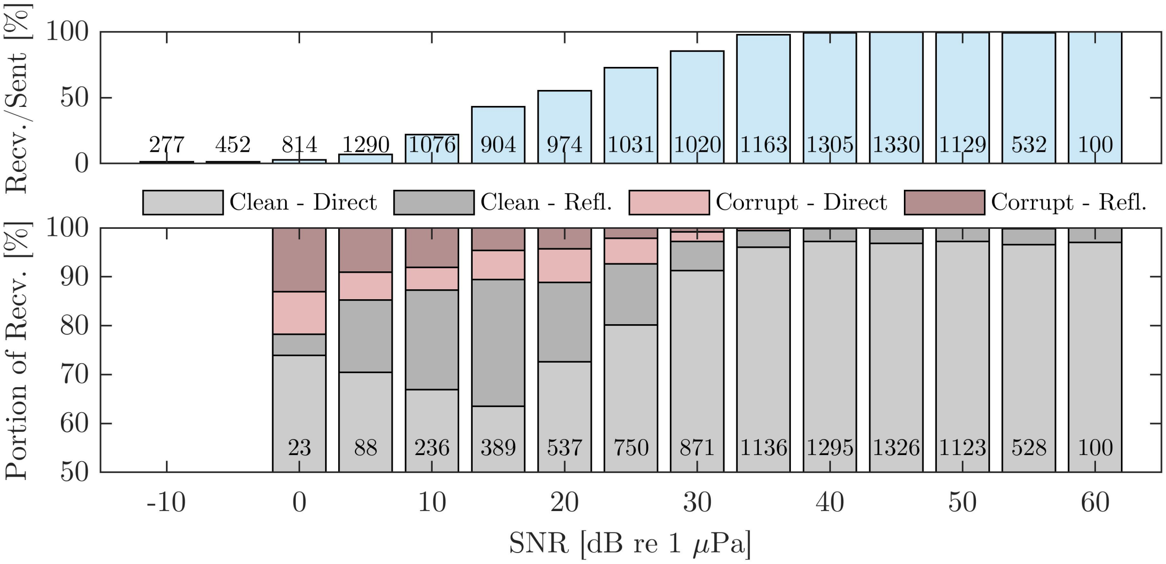

Figure D.1: Breakdown of received message by SNR. This includes only data from the four μFloats with externally mounted hydrophones. Numbers indicate total possible (upper) and total received (lower) pings in the SNR bin. Bins with fewer than 20 pings are omitted (i.e. receptions at -5 and -10).

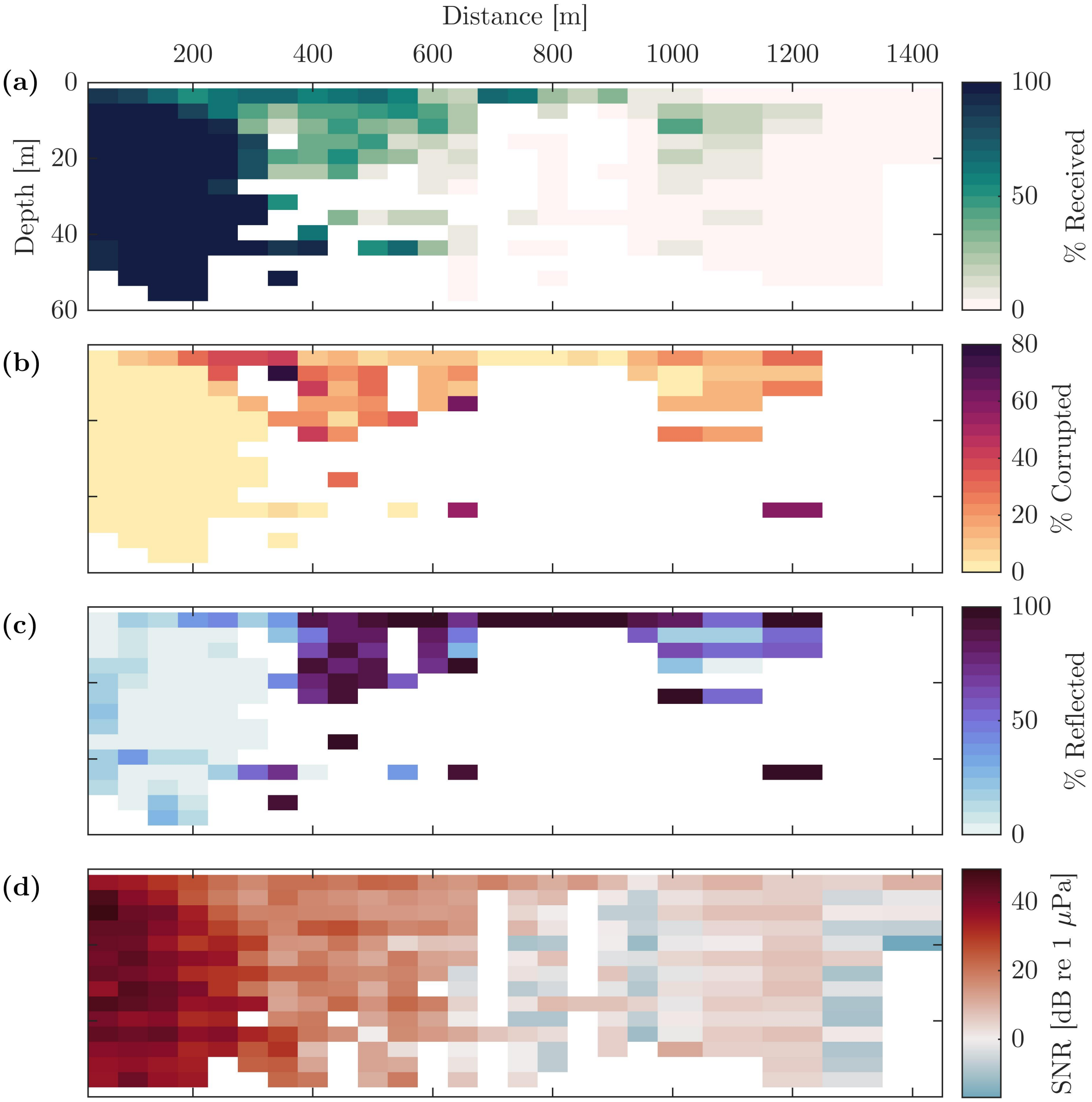

Figure D.2: Nanomodem connectivity during Lake Washington, as a function of depth and separation distance. (a) overall percent received relative to possibly received pings; (b) percentage of corrupt received messages; (c) percentage of received messages suspected of being following a reflected path; (d) SNR of received pings.

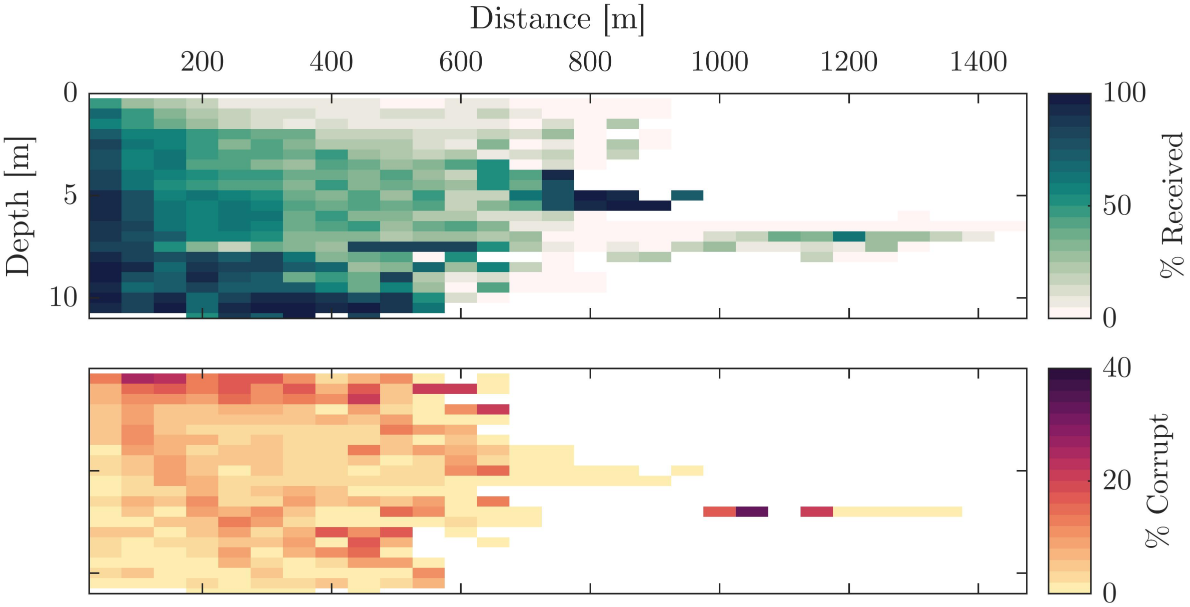

Figure D.3: Nanomodem connectivity in Agate Pass, as a function of depth and separation distance.

Appendix E

μFLOAT TECHNICAL DETAILS

E.1 Power Budget

As the μFloats were designed for the study of quickly evolving processes with time scales of interest from seconds to minutes, power efficiency was not a primary design objective. Nonetheless, an understanding of the power budget is useful for estimating how a given deployment schedule may reduce endurance, as well as guiding future design improvements.

To determine the average μFloat power budget, we analyzed electrical power data (5 Hz current and voltage measured at the battery bus) from all floats deployed during Agate Pass and Lake Washington tests. From a power-consumption perspective, the μFloat has two primary states: ‘active,’ in which the float is actively manipulating the buoyancy engine to dive to or hold a target depth, and ‘recovery,’ in which the float has fully extended its piston, returned to the surface, and is broadcasting its GPS location via radio and cellular modems. Recovery LEDs also blink while in this state. Background processes running on the single-board computer and logging of all data channels occur continuously during both of these states. Examining the power series from a typical float (Fig. E.1) shows the clear difference between the active and recovery time periods.

We can assess the relative consumption by the constant background processes, or ‘hotel’ load P_H, against the time-varying consumption by the buoyancy engine, $P_{BE}(t)$, by decomposing the power time series $P(t)$ accordingly,

$$P(t) = P_H + P_{BE}(t). \tag{E.1}$$

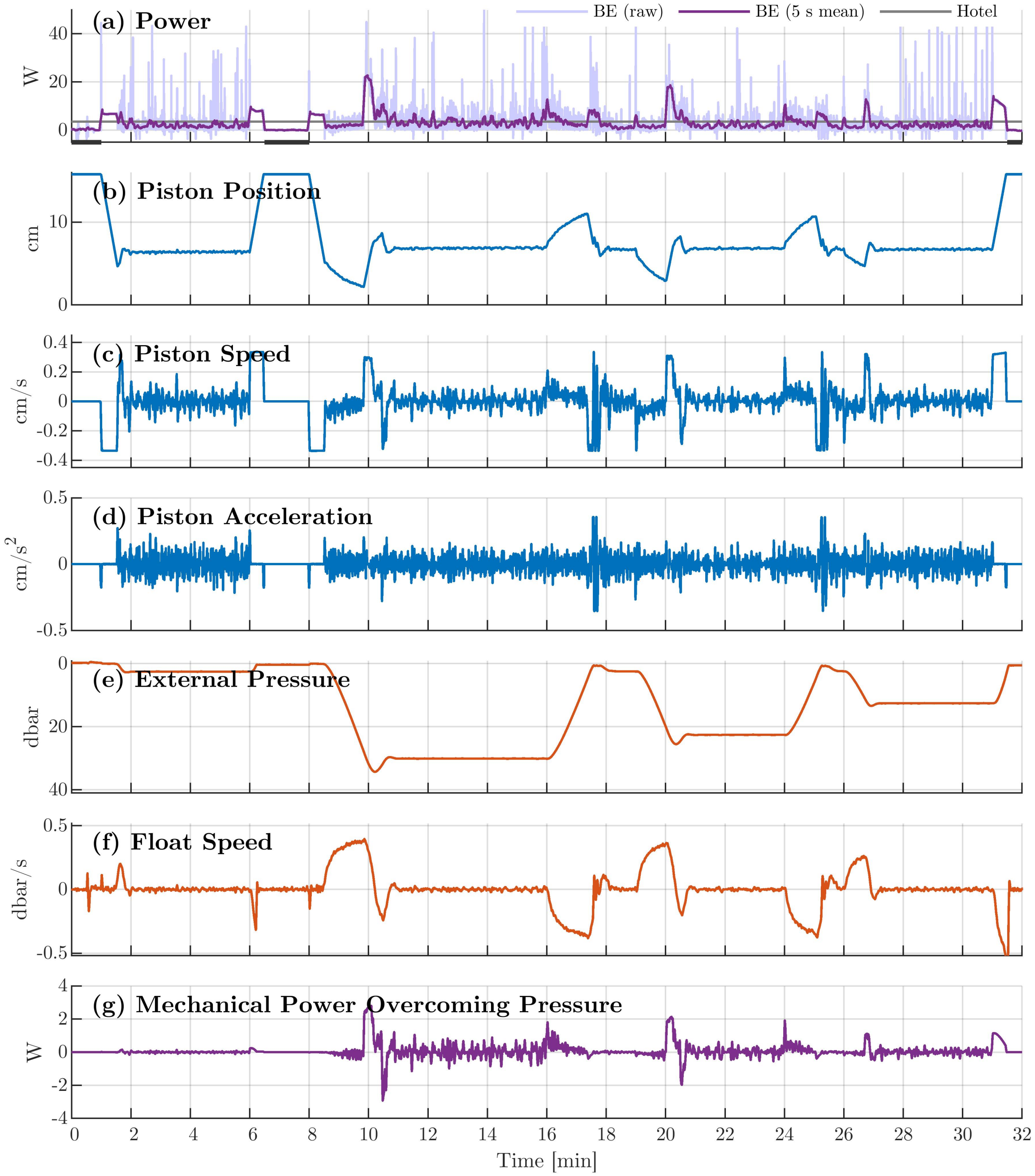

Figure E.1: μFloat electrical power consumption as function of time during segment of Lake Washington test (a). Note the hotel load P_H has been subtracted from the total power to produce the buoyancy engine load P_BE. Periods when the float was in recovery mode are indicated by black bars on (a). Associated time series are piston position (b), piston speed (c), piston acceleration (d), float pressure (e), float velocity (f), and the mechanical power acting against hydrostatic pressure (g).

Hotel Loads: Bench tests revealed that the power draw from radio and cellular broadcasting in recovery mode is negligible relative to the hotel load. Thus, for Lake Washington and Agate Pass tests, P_H was computed as the mean power when the piston was motionless (velocity less than 0.001 cm/s and acceleration less than 0.1 cm/s^2) and the float was on the surface (depth less than 1 m). Hotel loads were relatively consistent across the floats. During Lake Washington, the median hotel load was 3.7 W (min. 3.5 W, max. 4.7 W) and the median standard deviation of the hotel loads was 0.6 W, though four floats had significantly lower deviations (< 0.2 W) due float-to-float component variations. In Agate Pass, the median hotel load was 3.8 W (min. 3.7 W, max. 5.0 W) and the median standard deviation of the hotel loads was 0.4 W. The relatively large standard deviations ($\sim 10\%$ of the hotel loads) result from periods of repeated power spikes when the piston was not running. Further system tests are required to determine the source of these spikes and confirm they are reflective of actual power consumption.

Buoyancy Engine Loads: All power consumption beyond the mean hotel load was attributed to the buoyancy engine. Buoyancy engine power consumption was expected to depend on piston speed, piston acceleration, and float depth. General trends agreed, with power consumption increasing with piston speed and float depth (Fig. E.2), but inefficiencies in the drive train and inter-float variability preclude a deterministic power consumption model suitable for mission planning.

Examining the cumulative consumption for each float over the Lake Washington and Agate Pass tests indicated that power consumption was linearly correlated with the distance traveled by the piston (Fig. E.3a), though the constant of proportionality varied between floats. While piston travel is not known *a priori* as this depends on the response to disturbances, during tests we found that the motor ran nearly continuously while subsurface. Thus, total scheduled ‘active time’ can serve as a reasonable proxy (Fig. E.3b). Computing the median and 95^{th} percentile power consumption for the swarm provides a nominal and conservative estimate useful for planning purposes (Table E.1). Using this proxy, we found that the consumption rate in Lake Washington was higher than in Agate Pass, likely due to

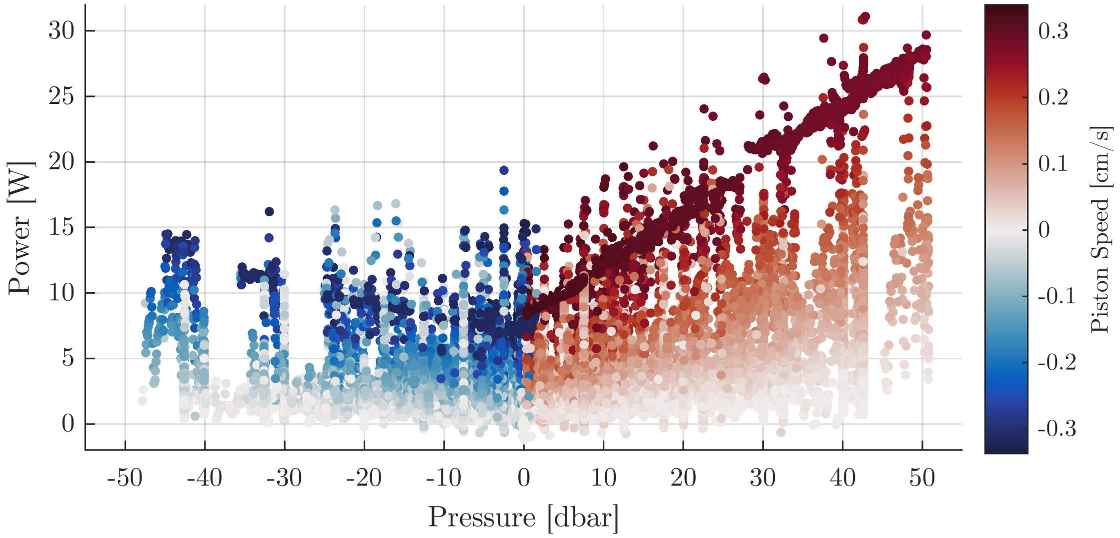

Figure E.2: Instantaneous power consumption, expressed as a function of hydrostatic pressure (float depth) and piston speed, for a float during Lake Washington tests. For clarity, pressure is assigned negative sign when the piston is retracting, as the pressure aids piston movement.

the deeper target depths. We attempted to embed depth into the heuristic relationship, but it increased ambiguity without increasing utility.

	$P_{BE,50^{\text{th}}}$	$P_{BE,95^{\text{th}}}$	Mean Depth
Lake Washington	4.2 W	4.7 W	14.0 m
Agate Pass	3.1 W	4.2 W	2.5 m

Table E.1: Buoyancy engine power consumption (50th and 95th percentiles) during Lake Washington and Agate Pass. The mean float depth over the duration of the test is provided for reference.

Improvements: Results demonstrate that total power consumption is a function of the hotel load, active time when the piston is operating, and powertrain efficiency. This indicates three clear paths for increasing endurance: (1) improve the efficiency of core electronics; (2) employ control schemes that reduce actuation time of the piston; and (3), refine or redesign

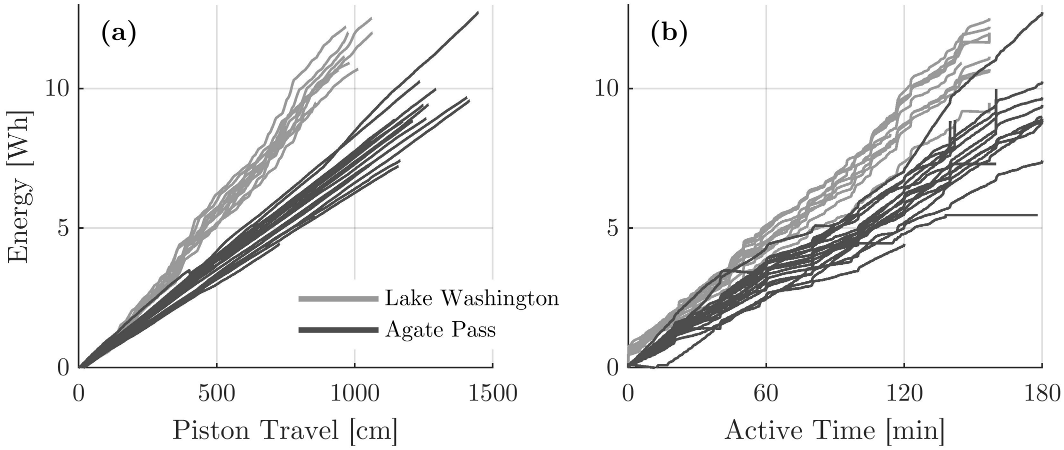

Figure E.3: Cumulative buoyancy engine power consumption as function of cumulative piston travel (a) and scheduled active time (b) during Lake Washington and Agate Pass deployments. Each line is one float.

the electro-mechanical drivetrain to increase efficiency. With the current system, only about 3 to 5% of the electrical power consumed by the buoyancy engine is accountable to overcoming external hydrostatic pressure (i.e., there is significant room for improvement).

E.2 Cost Breakdown

Considerable attention was given to reducing the unit cost of the μFloat to enable economic swarm deployments, resulting in a unit cost of \$2.4k, which is low in comparison to other coastal floats. A breakdown of the costs by subsystem is provided in Table E.2. The primary expense is the buoyancy engine, accounting for about 40% of the total cost, followed by the core electronics (18%) and communications (13%). However, the total costs for each subsystem are largely due to the cumulative contributions of moderately priced individual components. Thus, there are no quick steps to achieving further large reductions in system cost. Potential savings will likely be found in reducing the costs of custom parts and integrating more of the electronics into a custom board, thus reducing assembly time.

Table E.2: μFloat cost breakdown, organized by key subsystems

Buoyancy Engine	$ 969	Pressure Sensor	$ 210
		Custom Endcap and Seal	$ 290
		Piston, Traveling Nut, Alignment Plate	$ 193
		Lead Screw, Coupler, Bearing, Nuts	$ 96
		Internal Support Structure	$ 94
		Motor	$ 44
		Motor Driver	$ 37
		Limit Switches	$ 5
Core Electronics	$ 428	Custom battery pack	$ 165
		Single-board computer - Beaglebone Black	$ 61
		Power management electronics	$ 80
		Charging port	$ 60
		Inertial measurement unit	$ 42
		Relative humidity, pressure, and temperature sensor	$ 20
		Custom PCBs with misc. electronics and connectors	$ 100
Communications	$ 314	Acoustic nanomodem	$ 110
		GSM Modem - Particle Electron	$ 76
		GPS receiver	$ 44
		RF modem	$ 43
		WiFi modem	$ 11
		Custom PCB with misc. electronics and connectors	$ 30
Antenna	$ 174	Nanomodem transducer	$ 30
		GPS antenna	$ 24
		RF antenna	$ 15
		GSM antenna	$ 9
		LEDs	$ 3
		Bulkhead	$ 6
		Custom support structure	$ 5
		Urethane	$ 15
		Wiring and connectors	$ 22
		Assembly	$ 45
Structure	$ 242	Housing	$ 72
		Top and bottom flange seals (2x)	$ 67
		External hardware	$ 41
		Internal electronics chassis	$ 40
		Custom top endcap	$ 10
		Misc. ports	$ 12
External Sensors	$ 61	Temperature	$ 61
Assembly	$ 150		
Total	**$ 2338**		